

CONTENTS

OSCILLATORY SPATIOTEMPORAL SIGNAL DETECTION IN CLIMATE STUDIES: A MULTIPLE-TAPER SPECTRAL DOMAIN APPROACH

MICHAEL E. MANN AND JEFFREY PARK

1	Introduction	1
1.1	Motivation and Overview	1
1.2	Signal and Noise in Climate Data: Dynamical Mechanisms	3
2	Traditional Methods of Oscillatory Climate Signal Detection	6
2.1	A Synthetic Dataset	7
2.2	Conventional Approaches to Signal Detection	21
3	MTM-SVD Multivariate Frequency-Domain Climate Signal De- tection and Reconstruction	32
3.1	Signal Detection	33
3.2	Signal Reconstruction	36
3.3	Testing the Null hypothesis: Significance Estimation	38
3.4	Application to Synthetic Dataset	43
3.5	Effects of Sampling Inhomogeneities	46
4	Applications of MTM-SVD Approach to Observational and Model Climate Data	51
4.1	Global Temperature Data	54
4.2	Northern hemisphere surface temperature and sea level pressure joint modes	79
4.3	Long-term Multiproxy Temperature Data	110
4.4	Seasonal Cycle: Observations vs CO ₂ -forced model simulations	121
5	Conclusion	131
	References	133

OSCILLATORY SPATIOTEMPORAL SIGNAL DETECTION IN CLIMATE STUDIES: A MULTIPLE-TAPER SPECTRAL DOMAIN APPROACH

Michael E. Mann,
Department of Geosciences,
University of Massachusetts,
Amherst, MA 01003-8520,
(413) 545-9573

Jeffrey Park,
Department of Geology & Geophysics,
Yale University,
New Haven, CT 06520-8109,
(203) 432-3172

to appear in *Advances in Geophysics*

1. Introduction

1.1 Motivation and Overview

In order to properly assess the potential impact of forcings external to the climate system (e.g., possible anthropogenic enhanced greenhouse forcing), it is essential that we understand the background of natural climate variability on which external influences may be superimposed. Atmosphere-ocean-cryosphere interactions include many feedbacks that have time scales of years and longer. These feedbacks can, in principle, lead to irregular, but roughly cyclic, low-frequency climate variations (perhaps the most well-known example of which is the El Niño/Southern Oscillation or "ENSO"). If we can separate, in historical and proxy climate data, large-scale oscillatory, interannual and longer-period climate "signals" from the "background" climate variability, (1) it becomes easier to distinguish natural climate fluctuations from presumed anthropogenic or other external (e.g., solar) effects, (2) dynamical mechanisms potentially inferred from these signals provide a means of validating

numerical climate models; and (3) these signals can themselves potentially be used for long-range climatic forecasting.

The complex behavior of the climate system challenges any single exploratory data analysis method. Nonlinear dynamical mechanisms, for example, could connect variations on widely differing time scales. Some truly episodic phenomena, such as climatic responses to large volcanic eruptions, seem best suited for study in the time domain. Others, such as the periodic changes associated with the seasonal temperature in surface temperatures, are better suited for study in the frequency domain. For certain phenomena it is not clear whether an oscillatory or episodic picture is most appropriate. For example, both the statistical model of a step-wise discontinuity in the climate during the latter 1970s [e.g. *Trenberth*, 1980] and that of oscillatory behavior with a particularly abrupt variation in climate regimes occurring at about that time [*Latif and Barnett*, 1994; *Mann and Park*, 1994;1996] but with similar analogues at other times (e.g., 1900, 1915, 1940, 1955—see *Mann and Park*, 1994;1996] have been used to describe large interdecadal fluctuations in the North Pacific and northern hemisphere climate in recent decades. Depending on the null hypothesis and statistical criterion employed, both statistical models can be argued for at reasonably high levels of confidence. Still other phenomena, such as ENSO, exhibit a mix of time-domain, or “event”, characteristics and frequency-domain, or “oscillatory”, characteristics. Later in this introduction, we present a skeletal overview of the potential dynamical mechanisms behind low-frequency climate variability. In later sections, we present attempts to isolate and reconstruct “quasi-oscillatory” components of the climate system, with characteristic interannual to century timescales, using a powerful multivariate statistical technique called MTM-SVD. This technique combines the multiple-taper spectrum estimation methods (MTM), developed by Thomson [1982], with a principal-components analysis using the singular-value decomposition (SVD). Section 2 presents more traditional methods for oscillatory climate signal detection.

MTM-SVD detects an oscillatory signal in a spatially distributed data set (e.g., gridded historical climate fields) by identifying an unusual concentration of narrowband data variance in a particular large-scale pattern, relative to the random fluctuations of the background climate variability. Although formulated and applied as a signal detector in the frequency domain, MTM-SVD can be used to reconstruct the time history of any potential oscillatory climate signal, as well as its spatial

pattern. Secular trends in the data can also be detected and reconstructed in the MTM-SVD approach through a treatment of the near-zero frequency data variance. The evolution of an oscillatory signal over time, either in amplitude, frequency, or spatial pattern, can also suggest secular changes in the climate system, caused either by long-term natural variability or possible external forcings.

A proper estimate of the statistical significance of putative oscillatory signals is crucial in the application of MTM-SVD. As with most multivariate techniques, statistical inference is most straightforward if the null hypothesis for background variability is simply specifiable (e.g. spatially-uncorrelated white noise). Climate data falls far short of this ideal, as its random fluctuations exhibit significant correlations in both space and time. Much of Section 3 describes numerical experiments that demonstrate how to adjust the confidence levels for signal detection in MTM-SVD to account for such correlations. Section 3 describes the MTM-SVD method both formally, building upon the conceptual framework of other time series methods, and by demonstration on a variety of synthetic data sets.

The MTM-SVD methodology has been used for signal detection and reconstruction in global temperature data over the past century [*Mann and Park, 1994*], joint fields of surface temperature and sea level pressure in the Northern Hemisphere [*Mann and Park, 1996b*] and their relationship to continental hydroclimatic variations in North America [*Mann et al, 1995a*], low-frequency signals in the Atlantic and Pacific oceans [*Tourre et al, 1997*] signal detection in global [*Mann et al, 1995b*] and regional [*Bradley et al, 1994; Rajagopalan et al, 1996*] long-term climate proxy networks, the analysis of radionuclide tracers of the atmospheric general circulation [*Koch and Mann, 1996*], long-range climatic forecasting [*Rajagopalan et al, 1997*], and model vs. observational “fingerprint detection” of anthropogenic forcing [*Mann and Park, 1996a*]. We demonstrate in section 4 how MTM-SVD can be applied to some of these issues.

1.2 Signal and Noise in Climate Data: Dynamical Mechanisms

In a crude approximation, background climate variability can be described by a simple “red noise” model, in which the thermal inertia of the slow-response components of the climate system (e.g., the oceans as well as the cryosphere) tends to integrate the approximately white noise forcing provided by weather systems.

This process leads to enhanced noiselike variations at progressively longer periods [Hasselmann, 1976]. More detailed noise models have been developed which take into account the additional effects of convective and diffusive exchanges between the mixed layer and deeper ocean [Wigley and Raper, 1990]. More generally, climatic noise can be characterized as exhibiting a “coloured noise” spectrum, associated with some underlying spatial correlation structure. Such “noise” however is insufficient in describing the natural variability of the climate that arises from internal oscillatory modes of the climate system which are either self-sustained through non-linear dynamics or stochastically excited by the noise itself. These low-frequency modes or “signals” may further compound the detection of anthropogenic climate forcing [see e.g., IPCC, 1996; Barnett *et al.*, 1996]. The identification of such signals may have a profound importance in its own right, providing the possibility of skillful climate forecasting at decadal and longer lead times [see Latif and Barnett, 1994; Griffies and Bryan, 1997, Rajagopalan *et al.*, 1997]. For both reasons, the detection and description of low-frequency oscillatory climatic signals represents a problem of paramount importance both scientifically and societally.

Besides the seasonal and diurnal cycles, there is scant evidence for truly periodic climate signals [see Burroughs, 1992]. Many climatic processes nonetheless appear to exhibit some oscillatory character, describing spatially-coherent climatic variations which tend to oscillate between different states owing to a variety of possible linear or non-linear feedback mechanisms. Such “quasi-oscillatory” signals, as we term them, are marked by a dominant timescale of variation, and often by finite, somewhat episodic, spells of large-amplitude oscillation. Perhaps the best-known example is the El Nino/Southern oscillation which exhibits oscillatory variability within a 3-7 year timescale range, apparently further organized into distinct low-frequency (4-6 year) and high-frequency (2-3 year) narrow frequency bands [e.g., Barnett, 1991; Keppenne and Ghil, 1992; Dickey *et al.*, 1992; Ropelewski *et al.*, 1992; Mann and Park, 1994;1996b]. Such behavior can be associated with underlying coupled ocean-atmosphere dynamics which are presently understood at a reasonably fundamental level [Cane *et al.*, 1986; Philander, 1990]. There is mounting evidence both from observational analyses and a variety of theoretical climate model investigations that similar types of oscillatory signals may exist in the climate on decadal-to-century timescales. Several workers have isolated decadal-to-interdecadal [e.g., Folland *et al.*, 1984; Ghil and Vautard, 1991; Allen *et al.*, 1992; Mann and Park, 1993; 1994; Royer,

1993; *Mann et al*, 1995a;1995b; *Dettinger et al*, 1995; *Mann and Park*, 1996] and more speculative century-scale [*Schlesinger and Ramankutty*, 1994; *Mann and Park*, 1994; *Mann and Park*, 1996] oscillatory behavior in instrumental climate records spanning a little more than the last century. The investigation of longer-term proxy data supports the existence of interdecadal [*Plaut et al*, 1995; *Mann et al*, 1995b] and century-scale [*Stocker et al*, 1992; *Mann et al*, 1995b] climate signals prior to the 20th century.

While many studies have attributed observed decadal-to-century scale variability to external forcing due to the 18.6-year soli-lunar tide [e.g., *Mitra et al*, 1991; *Currie and O'Brien*, 1992; *Royer*, 1993], the ~ 11 -year solar cycle [e.g., *Labitzke and van Loon*, 1988; *Tinsley*, 1988; *Mitra et al.*, 1991; *Currie and O'Brien*, 1992] and its 22-year subharmonic or “Hale” cycle [*Vines*, 1986], and low-frequency changes in solar irradiance forcing [e.g., *Friis-Christensen and Lassen*, 1991, *Lean et al*, 1995], the most plausible oscillatory mechanisms – both in terms of physical mechanisms and their similarity in character to observed patterns of variability – involve natural oscillatory processes of the ocean or coupled ocean-atmosphere system. A convenient categorization of possible mechanisms is provided by *Stocker* [1996], including (a) the interaction between the meridional overturning “thermohaline” circulation and the wind-driven circulation [*Weaver and Sarachik* 1991; *Weaver et al*, 1991; *Huang*, 1993; *Cai and Godfrey*, 1995] (b) the interaction of thermally-generated baroclinic gyre anomalies and the thermohaline circulation [*Delworth et al*, 1993; *Greatbatch and Zhang*, 1995], and (c) the basin-scale advection of surface salinity [*Maier-Reimer and Mikolajewicz*, 1989; *Mysak et al*, 1993; *Griffies and Tziperman*, 1995; *Schmidt and Mysak*, 1996] or temperature [*Saravanan and McWilliams*, 1995] anomalies influencing deep water production and meridional overturning. A fourth category not highlighted by *Stocker* [1996] but which has nonetheless gained recent prominence involves the gyre-scale advection of thermal anomalies in the Pacific basin, associated changes in the thermal structure of the upper ocean, and its feedback on the atmospheric windstress profile [*Latif and Barnett*, 1994; *Von Storch*, 1994]. In addition, other studies have suggested that the interaction between high-latitude brine release and ocean circulation [*Yang and Neelin*, 1993], sub-harmonic generation arising from the nonlinear interaction of sea ice and high-latitude heat/freshwater fluxes [*Yang and Huang*, 1996] see also *Saltzman and Moritz*, 1980; *Saltzman*, 1982 for a more general discussion of the underlying non-linear dynamics] when driven by an annual

cycle, and the interaction between of ice-cover and thermal insolation [Zhang *et al*, 1995], coupled arctic sea-ice/atmospheric circulation processes [Mysak and Power 1992; Darby and Mysak, 1993] may lead to organized variability on decadal-to-century timescales. A final possibility is that such variability is simply the product of the fundamentally chaotic interaction of the atmosphere and ocean-atmosphere system at decadal and longer timescales [see Lorenz, 1990; Roebber, 1995; Liu and Opsteegh, 1995; Kurgansky *et al*, 1996].

It is useful to further distinguish the possible climatic mechanisms discussed above in terms of the fundamental nature of the underlying dynamics. This is not always a straightforward task, as the distinction between self-sustained unstable oscillations and stochastically forced stable oscillations based on classical diagnostics may not be obvious [Saltzman *et al*, 1981]. Self-sustained non-linear oscillations result from a phase-space bifurcation of the system’s dynamics [e.g., Hopf bifurcation – see Quon and Ghil, 1995; Chen and Ghil, 1995;1996]. Furthermore, such self-sustained non-linear oscillatory behavior may exhibit a dependence on the external control parameters of the non-linear system, and frequency-modulation is also possible [e.g., Tziperman *et al*, 1994; Jin *et al*, 1994] if the phase-space character of the system undergoes lower frequency changes. Such oscillatory behavior tends to exhibit chaotic intermittent oscillations [see Lorenz, 1990] and furthermore, is assumed to be obscured by the noise present in the climate system. In contrast, stochastically excited, damped stable oscillations can arise in both linear and non-linear systems. Such oscillations arise from the excitation of the natural eigenmodes of a stable system by stochastic coloured noise forcing [e.g., Hasselmann, 1988; Mysak *et al*, 1993; Weaver and Sarachik, 1991; Schmidt and Mysak, 1996; Delworth *et al*, 1993; Latif and Barnett, 1994]. Any means of exploratory signal detection in climate studies should be sufficiently general to identify, though perhaps not distinguish, stochastically excited or self-sustained oscillatory behavior, since neither can *a priori* be eliminated based on theoretical or dynamical considerations.

2. Traditional Methods of Oscillatory Climate Signal Detection

A variety of techniques have been applied to the problem of signal detection in observational and dynamical model-generated climate data. Such techniques have typi-

cally employed univariate methods for isolating narrowband peaks in the power spectrum of climate time series based on spectral estimation methods such as Blackman-Tukey or Maximum Entropy Spectrum Analysis [e.g., *Brillinger*, 1981; *Marple*, 1987]. Traditional attempts to exploit the mutual information available in spatially distributed climate records have involved Principal Component Analysis (PCA) or related orthogonal multivariate spatiotemporal decompositions [*Preisendorfer*, 1988; *Bretherton et al*, 1992] followed by spectral analysis of the time series of the resultant spatial modes [e.g., *Trenberth and Shin*, 1984; *Deser and Blackmon*, 1993; *Tanimoto et al*, 1993]. Only recently have methods been developed [e.g., Principal Oscillation Patterns (“POPs”) – *Hasselmann*, 1988, Multichannel Singular Spectrum analysis (“M-SSA”) – *Keppenne and Ghil*, 1993, and Multitaper frequency-domain Singular Value decomposition (“MTM-SVD”) – *Mann and Park*, 1994] which simultaneously exploit both the coherent spatial structure and narrowband frequency-domain structure of climatic signals for more efficient spatiotemporal signal detection. Furthermore, the properties of climatic noise and proper null hypothesis testing in the context of multivariate signal detection approaches have only recently begun to receive proper attention [e.g., *Mann and Park*, 1996b; *Allen and Robertson*, 1996].

In this section, we motivate a particular model – that of spatiotemporal coloured noise – as the null hypothesis for climate variability. A spatiotemporal model is invoked because of the intrinsic large-scale spatial structure of climatic variations. A “coloured noise” model is invoked because the complicated dynamics of the climate system lead to stochastic variations with a frequency-domain structure more complicated than simple (e.g., Gaussian white noise) models. This model must be sufficiently well rejected if we are to infer the existence of (ie “detect”) a signal in a climatic data field. We argue that such climate signals should be associated with patterns that exhibit wider spatial coherence than the underlying noise, with narrowband frequency-domain signatures. Under such assumptions for climatic data, we show how traditional methods for signal detection suffer from a number of weaknesses. We motivate instead the MTM-SVD methodology which overcomes many such weaknesses, and provides certain optimal features in multivariate signal detection and reconstruction. We demonstrate that the MTM-SVD method produces correct inferences when applied to known (i.e., specified synthetic) spatiotemporal coloured noise processes, focusing on spatially-correlated “red” noise (including that which is considerably “redder” than estimates for actual climate data). When ap-

plied to synthetic data examples, MTM-SVD provides excellent fidelity in signal detection and reconstruction. Finally, we demonstrate that the approach does not suffer significantly when substantial temporal and spatial inhomogeneities, typical in real climate data, are introduced into the synthetic example.

2.1 Signal and Noise Assumptions: A Synthetic Dataset

We introduce here a synthetic example with the basic signal and noise attributes inferred for observed climate data. The synthetic data are constructed on a grid resembling a cartesian projection of the spherical globe such as is typically used for gridding actual spatial climate data (Figure 1). The gridded network has uniform monthly sampling and a duration $N = 1200$ months (100 years).

The dataset is constructed so as to contain two irregular oscillatory signals and a trend, each widely correlated over the synthetic global domain, linearly added to noise which exhibits near-neighbor spatial correlation and an underlying red noise temporal autocorrelation structure. Thus constructed, the noise, while spatially-correlated, does not exhibit the large-scale coherent structure associated with the low-frequency climate “signals.” This latter distinction, motivated for both theoretical observational-based considerations described below, underlies the reason that multivariate analysis can greatly enhance the effective signal-to-noise ratio and efficiency of signal detection and reconstruction.

Noise component

We adopt a model of spatially correlated coloured noise that is motivated by theoretical models for stochastic climate variability. In the absence of any complex dynamics, the inertia of the ocean and other slow-response components of the climate system alone tend to integrate any high-frequency (often approximated as “white”) noise forcing provided synoptic-scale “weather” forcing [see *Hasselmann*, 1976], altering the temporal characteristics of the noise, but preserving the limited, near-term spatial correlation structure of the noise.

The simplest mathematical description of such an integrating noise process in the context of discretely measured variables such as monthly mean climate data, is the first-order autoregressive (“AR(1)”) red noise process [see *Gilman et al.*, 1963],

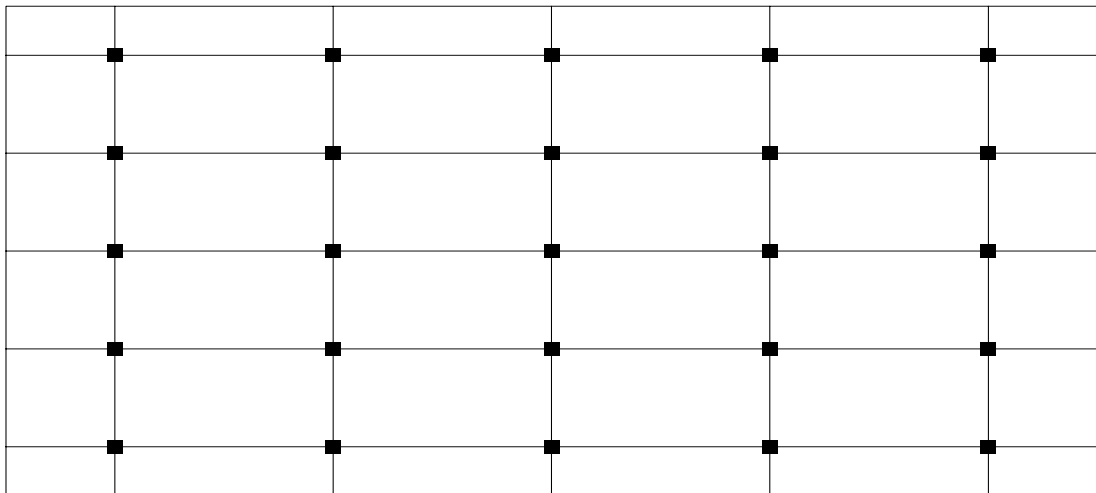


Figure 1: Global Cartesian grid showing spatial sampling of synthetic data network. Sampling of 25 gridpoints is equally distributed in both longitude (72° separation between gridpoints) and latitude (36° separation between gridpoints), with data centered at the “equator” and in “subtropical” and “subpolar” zonal bands in the two “hemispheres” of the synthetic domain. [From Mann (1998).]

specified by the statistical model,

$$y_t = \rho y_{t-1} + w_t \quad (1)$$

(where w_t is a white noise “innovation” sequence, with variance σ^2) and characterized by the power spectrum,

$$S(f) = S_0 \frac{1 - \rho^2}{1 - 2\rho \cos(f/f_N) + \rho^2} \quad (2)$$

where the average power S_0 is related to the white-noise variance,

$$S_0 = \sigma^2 / (1 - \rho^2) \quad (3)$$

Figure 2 shows the power spectrum for ideal monthly sampled AR(1) red noise processes of increasing levels of autocorrelation. In the AR(1) red noise model, autocorrelation decays exponentially so that the decorrelation timescale of the noise τ is related to the lag-one autocorrelation coefficient ρ by $\tau = -\Delta t / \log \rho$ where Δt is the temporal sampling interval. ρ (and less directly τ) is a parameter that measures the relative “smoothness” of the noise spectrum – i.e., how rapidly the amplitude of the noise spectrum varies with frequency. This smoothness can be quantified in terms of the relative gain over the bandwidth of the spectrum estimator, which we will define by the factor,

$$F(f) = \Delta f_{BW} \frac{d \log S(f)}{df} \quad (4)$$

where a spectrum bandwidth $\Delta f_{BW} \approx 0.04$ cycle/year is typically applicable in studies of multidecadal-to-centuries duration climate datasets (see section 2.1). Thus defined, F measures the relative “inverse” of smoothness. A smoothly-varying noise spectrum can be characterized by the local or global (in the frequency domain) fulfillment of the condition that F be small compared to unity (i.e., $1/F$ large). For $F \gtrsim 1$ we might expect the “smoothness” assumption to begin to break down, and for $F \gg 1$ we certainly do.

Given the typical bandwidth indicated above, we can consider the estimated smoothness for the different cases described in Figure 2. For $\rho = 0$ we observe a uniform “perfect” inverse smoothness factor $F = 0$ for all frequencies. For the “moderate” case $\rho = 0.9$, we have a maximum value of the parameter $F_{MAX} \approx 0.11$ near $f = 0.2$ cycle/year, and an average value over the interannual frequency range of interest $f < 0.5$ cycle/year, of $F_{AVE} \approx 0.09$. For the more strongly red case

$\rho = 0.99$ the corresponding values are $F_{MAX} = 0.8$ (near $f = 0.02$ cycle/year) and $F_{AVE} = 0.2$. Finally, for the nearly singular case we have $F_{MAX} = 8$ (near $f = 0$) and $F_{AVE} = 0.6$. Roughly speaking, then, we might consider the noise spectrum as smoothly varying throughout the interannual frequency range for the case $\rho < 0.9$. For the case $0.9 \lesssim \rho < 0.99$ we can consider the noise spectrum as varying smoothly over most of the interannual frequency interval, though perhaps less so near zero frequency. As $\rho \rightarrow 1$, the AR(1) red noise process approaches a pure random walk $y_t = y_{t-1} + w_t$, characterized by first-order non-stationarity, an infinite decorrelation timescale τ and a spectrum that is singular at $f = 0$. As the random-walk condition is approached, the noise spectrum may violate our smoothness assumption. As shown in section 2.1, the best-fit red noise spectrum for instrumental climate data fall in the white ($\rho = 0$) to moderately red ($\rho = 0.9$ for monthly data – i.e., $\tau \approx 0.8$ years) range, and should satisfy the requirements of a smoothly varying noise background.

AR(1) red noise accurately describes the physical model of natural variability for a simple stochastically-forced energy balance of the climate which contains a mixed-layer ocean. It can also be shown to be the limiting case of more complex stochastic models of climate which allow for exchange of heat with the deep ocean [Wigley and Raper, 1990]. The latter noise model in general requires the specification of a number of poorly constrained physical parameters, and is statistically described by higher order AR models. A combination of dynamical considerations and parsimony thus might tend to favor the AR(1) red noise model. Indeed, empirical studies of a wide variety of proxy and instrumental climate data [Gilman *et al.*, 1963; Kutzbach and Bryson, 1974; Allen and Smith, 1994; Mann and Lees, 1996] suggest that the AR(1) red noise model provides an excellent description of the background climate noise spectrum. Nonetheless, the ideal null hypothesis accommodates both simple AR(1) red noise and more general coloured noise processes. In section 3.3 we introduce a means for employing such a more general coloured noise null hypothesis in signal detection. Nonetheless, for demonstrative purposes, we here consider the null hypothesis of climatic noise modeled as having the temporal correlation structure described by the AR(1) red noise model, and short-range spatial correlation structure. Typical estimates of the temporal decorrelation timescales for monthly gridded surface temperature data, for example, are $\tau \lesssim 1$ year [Allen and Smith 1994; Mann and Lees, 1996]. Estimates of temporal decorrelation scales in actual observational data

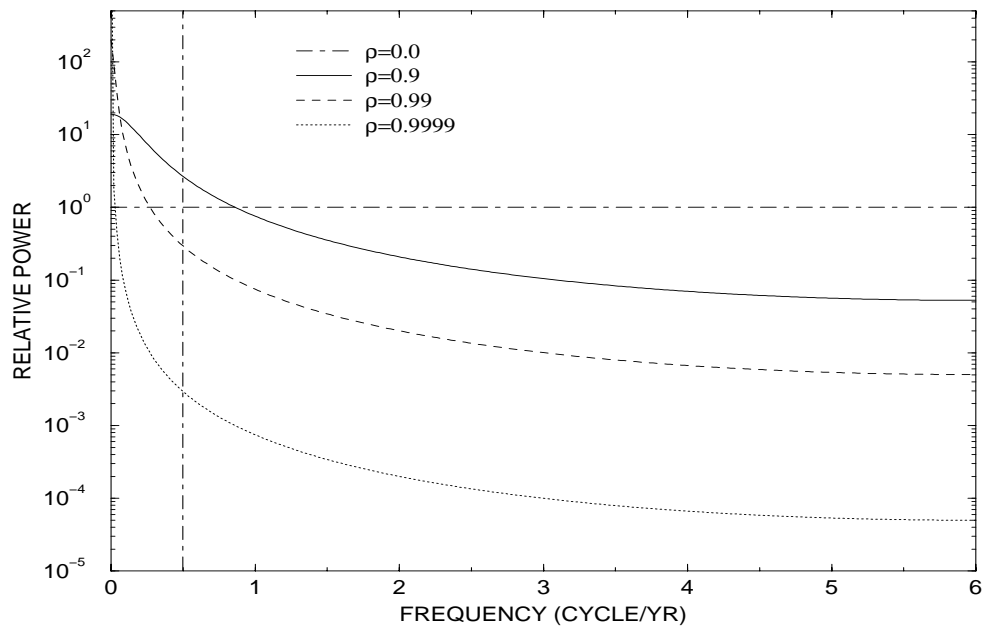


Figure 2: Power spectra of ideal monthly sampled AR(1) red noise processes with varying levels of month-to-month autocorrelation ρ . The vertical line separates off the “interannual” ($f < 0.5$ cycle/year; periods greater than $T = 2$ year) regime of the spectrum. [From Mann (1998).]

are discussed in more detail in section 2.1. While the spatial decorrelation length scale d tends to vary somewhat with season [Livezey and Chen, 1983; Briffa and Jones, 1992], estimates from both model-based [Madden et al., 1993] and observational [Kim and North, 1991; Mann and Park, 1993] data indicate an approximate value of $d = 1500 - 2000$ km for monthly surface temperature data. In keeping with the above qualitative description of climatic noise, we prescribe a spatiotemporal AR(1) red noise background with a roughly $d = 1.5$ grid spacing decorrelation length scale, and a temporal decorrelation timescale of $\tau \approx 0.9$ year ($\rho = 0.9$) in the synthetic monthly dataset.

Signal Component

Typical climate signals (e.g., the El Niño/Southern Oscillation or “ENSO”) tend to be associated with large-scale (i.e., global or hemispheric-wide) perturbations of the coupled ocean-atmosphere system. Such signals are detectable not only in climatic measurements in the regions where the intrinsic climate dynamics are important [e.g., the tropical Pacific in the case of ENSO – see Cane et al, 1986], but through their altering effect on planetary wave propagation, and global atmospheric circulation patterns, lead to substantial perturbations in remote regions [e.g., Horel and Wallace, 1981]. Such signals are thus detectable in part because of their hemispheric or global-scale spatial organization. The patterns of expression of ENSO in surface temperature [Ropelewski and Halpert, 1987] and precipitation [Halpert and Ropelewski, 1992] are clearly global in extent, and have been theoretically shown to be consistent with the influence of tropical heating anomalies on the planetary wave structure of the extratropical atmosphere [see e.g. Horel and Wallace, 1991] There is recent evidence both in observational studies [e.g., Dettinger et al, 1995; Ghil and Vautard, 1991; Mann and Park, 1993;1994;1996b; Schlesinger and Ramankutty, 1994; Mann et al, 1995b] and coupled ocean-atmosphere model simulation studies [e.g., Latif and Barnett, 1994; Delworth et al, 1993] for oscillatory climate mechanisms with similar global-scale influence at decadal and longer timescales.

Most theoretical models describe such signals as having a quasi-oscillatory character. Positive and negative feedbacks, and delayed oscillator coupled mechanisms can allow for oscillatory behavior in either a linear or non-linear dynamical context. Either intrinsic non-linearities or stochastic forcing can modulate both amplitude and phase, leading to finite spells, or episodes, of coherent oscillatory behavior.

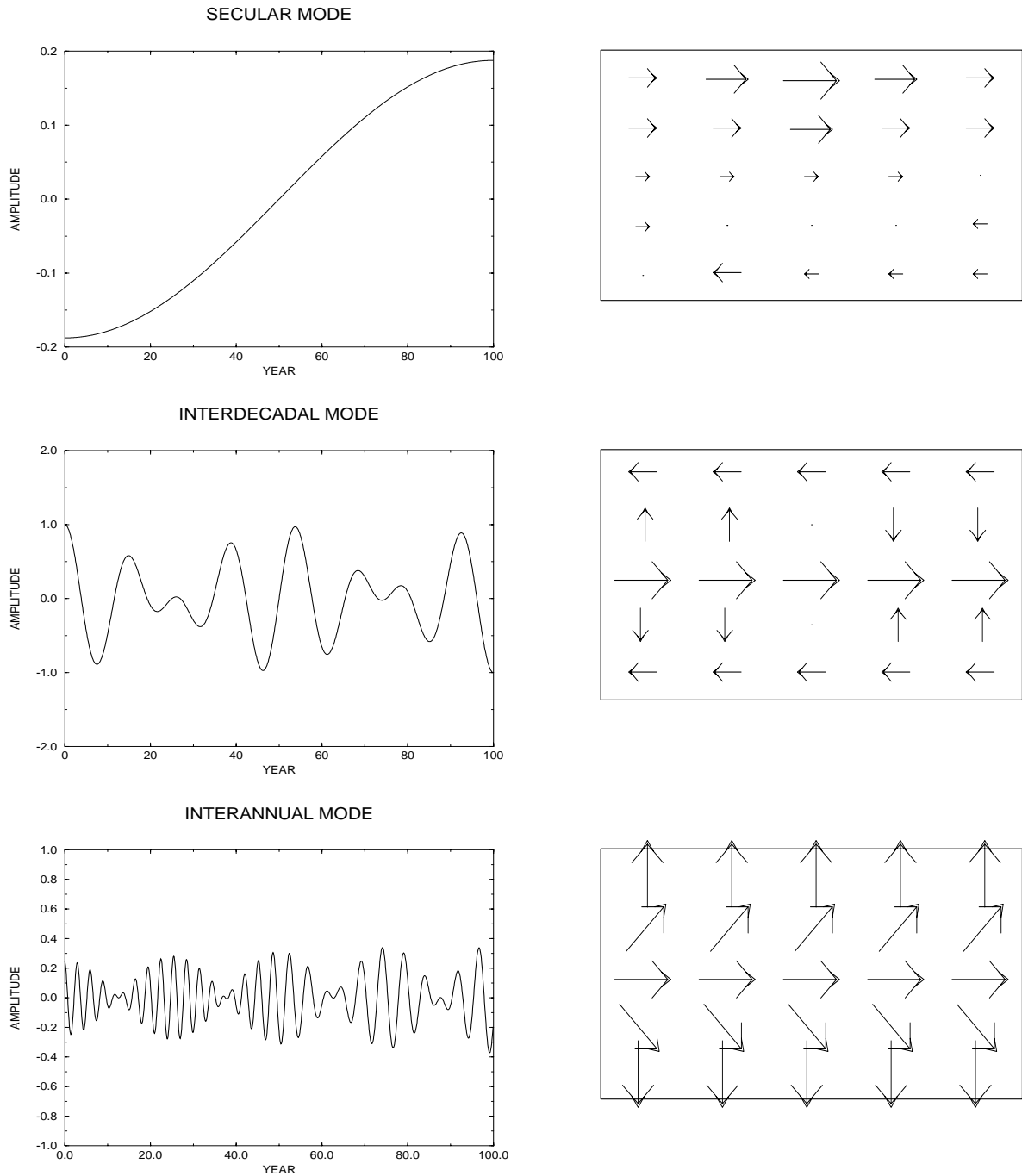


Figure 3: Temporal (left) and Spatial (right) patterns of synthetic signals showing (a) secular mode, (b) interdecadal mode and (c) interannual mode. Conventions are described in the text. [From Mann (1998).]

TIME SERIES FOR REFERENCE GRIDPOINT

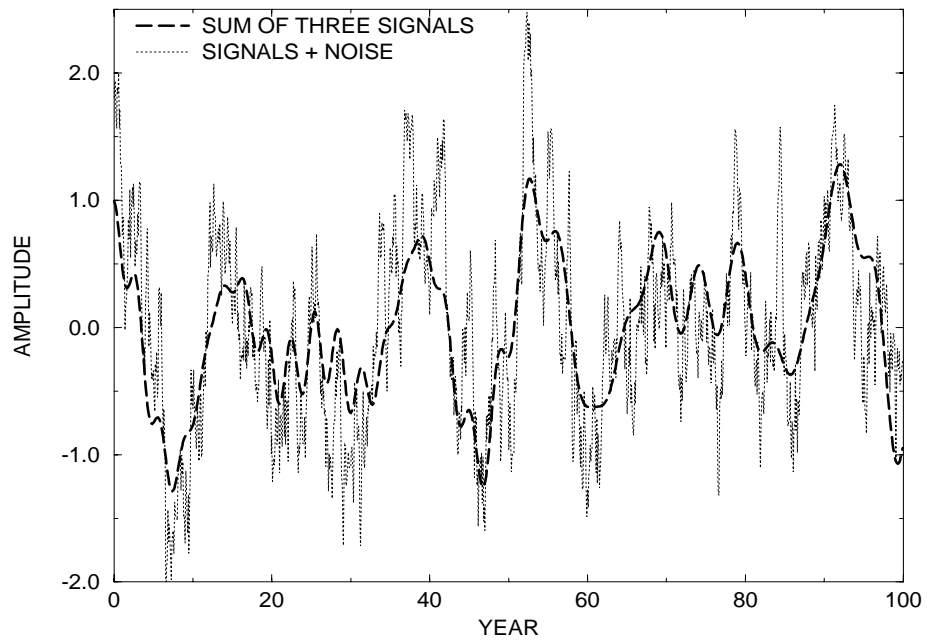


Figure 4: Time signal and signal+noise for reference (central) gridpoint time series. [From Mann (1998).]

SIGNAL	SPATIAL CHAR	TEMPORAL CHAR	T (years)	f (cyc/yr)	MAX AMP.
TREND	Variable amp/sign	half-cosine trend	200	0.005	1.0
INTERDEC. OSCIL	Variable amp/phase	amp mod	15	0.065	1.0
INTERANN. OSCIL	Uniform amp/variable phase	amp/freq mod	3-5	0.33-0.2	1.0
RED NOISE	near-neighbor spat. correlation	AR(1) red noise			1.0

Table 1: Description of the 3 synthetic examples and noise in the synthetic example, Indicating the Spatial and Temporal characteristics of Each Signal (Spatial Phase and Amplitude Pattern, and Pattern of Temporal Modulation), Signal Period (or Period Range) in Years, Frequency (or Frequency Range) in Cycles/Year, and Maximum Regional Peak Amplitude. [From Mann (1998).]

Furthermore, frequency modulation [e.g., in the case of ENSO-see *Tziperman et al*, 1994; *Jin et al*, 1994] can result from changes in external governing parameters. A proper statistical model for oscillatory climate signals must thus describe a narrow-band but not strictly periodic mode of variability with spatial scale structure that is coherent (though perhaps quite variable in sign or phase) at large spatial scales. Climatic trends that are inconsistent with the noise null hypothesis can be treated as oscillatory signals with zero frequency (i.e., infinite period). Other types of climate signals (e.g., volcanic climate perturbations) may have truly event-like character that is best described by alternative statistical models. [e.g., wavelet based generalizations of the frequency domain methods discussed below – see *Lilly and Park*, 1995; *Park and Mann*, 1997].

The synthetic dataset exhibits the key features of our conceptual model of the climate system. Slowly modulated quasi-oscillatory low-frequency components and a secular trend are superposed on a spatially and temporally autocorrelated noise component, with the relative importance of each varying by location. We construct three synthetic signals that exhibit the kinds of complexity (e.g., amplitude, phase, and frequency modulation) that we might expect to encounter in true climate signals. The first signal is a secular trend with a half-period cosine shape describing a variable amplitude “warming” trend in most locations. Some locations exhibit the opposite sign or a vanishing amplitude. This signal represents an analog for a spatially-variable global warming signal. The second signal represents an inter-decadal oscillation with phase/amplitude modulation that vanishes in a global average due to phase cancellation over the domain. The third signal exhibits the most complex characteristics, with uniform amplitude, but partial phase cancellation, an amplitude trend with periodic modulation and linear ramp, and frequency modulation with a rapid transition between 3 and 5 year periodicity during the middle 40

years. This signal exhibits a poleward propagating phase pattern.

The amplitudes of the signals are prescribed so that the total signal variance is equal to the total noise variance (i.e., the aggregate signal-to-noise variance ratio is unity). The secular trend describes 56% of the raw data variance, the interdecadal signal 25%, and the interannual signal 8%. The residual 43% variance is explained by the spatially-correlated red noise. Note the similarity between this imposed breakdown of variance, and the empirical signal/noise decompositions of *Mann and Park* [1994;1996b], recounted in Section 4.1 and 4.2. In these data sets the identified signals consume a somewhat smaller proportion of the data variance, roughly 40%. The residual 60% variance was attributed to the coloured noise background. The characteristics of the signals and noise are summarized in Table 1. In Figure 3 we show the spatial and temporal patterns of the three signals described above, while in Figure 4 we show the time reconstruction for a reference site (center gridpoint). The relative spatial pattern is depicted by a vector map in which the angle represents the relative phase and the length indicates the relative amplitude of the signal at each gridpoint.

Comparison with Actual Climate Data

In this section, we estimate the signal and noise properties of actual instrumental climate data to help motivate our assumptions regarding signal and noise in the preceding sections. We make use of the historical gridded temperature data used by *Mann and Park* [1994] in their multivariate analysis of global temperature variations. In Figure 5, we show the spectra (as estimated by the multitaper method – see section 2.2) along with the best-fit red noise background for a few instrumental gridpoint temperature series in the subset of 449 nearly continuous 100 year gridpoint temperature records over the globe (see Figure 16).

In almost every of the 449 gridpoint series, the null hypothesis of white noise (i.e., AR(1) noise with $\rho = 0$) is rejected at a very high level of likelihood, with the best fit values of ρ ranging from 0.09 to 0.80 and averaging $\rho \approx 0.35$. The null hypothesis of red noise is only *weakly* rejected, however. For example, due to chance coincidence alone, we would expect 30 peaks to randomly exceed the 90% confidence level over the positive Nyquist interval ($f = 0$ to $f = 6.0$ cycle/year) for a realization of a true AR(1) red noise process with the bandwidth $NW = 2$ employed in the spectrum estimation (see section 2.2). In contrast, the typical temperature

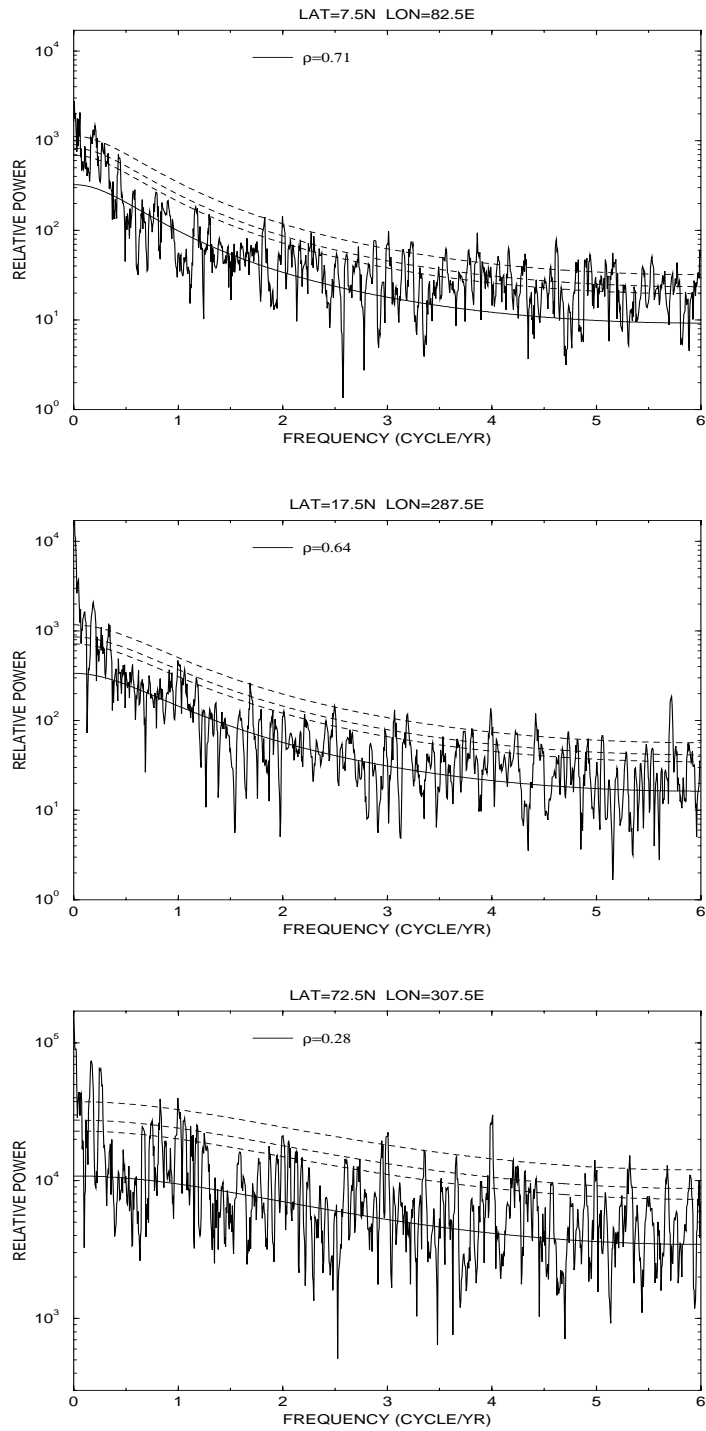


Figure 5: Multitaper spectra of 3 different 100 year long monthly land air and sea surface temperature gridpoint records over the globe based on time-frequency bandwidth factor $NW = 2$ and $K = 3$ tapers, along with robustly estimated median red noise level and 90,95,and 99% confidence limits for significance relative to red noise – see section 2.2. [From Mann (1998).]

gridpoint yields 35-45 peaks that exceed that level. This small discrepancy between expected rates of false detection, and observed rates of signal detection implies the existence of additional structure in the climate spectrum which is not consistent with red noise. We hypothesize that such additional structure implies the existence of a small number of distinct band-limited processes superposed on a stochastic red-noise background. We thus argue that (a) moderate ($\rho < 0.9$) red noise provides an excellent null hypothesis for the noise background and (b) there is evidence for a small number of signals in addition to the noise background. The forgoing analysis cannot establish whether the latter “signals” do indeed represent spatiotemporally consistent signals in the multivariate data, and is limited by its assumptions of a strict AR(1) noise model. We introduce in section 3.1 a methodology for signal detection that does not suffer either of these limitations. First, however, we review the traditional approaches to oscillatory climate signal detection.

2.2 Conventional Approaches to Signal Detection

Univariate Signal Detection

While a variety of traditional spectral analysis methods (e.g., Blackman-Tukey) have been widely employed in the analysis of geophysical processes [see e.g. the review by *Brillinger*, 1981 and references therein], specialized methods have more recently been developed that are more faithful in their underlying assumptions to the irregular oscillatory behavior expected of climatic signals. Among such methods are multitaper spectral analysis [*Thomson*, 1982; *Park et al*, 1987; *Percival and Walden*, 1993] which employs multiple orthogonal data tapers to describe phase and amplitude modulated structures, and Singular Spectrum Analysis [*Vautard and Ghil*, 1989; *Ghil and Vautard*, 1991; *Ghil and Yiou*, 1996] which makes use of anharmonic basis functions derived from the lagged covariances of the data series.

These univariate spectral analysis approaches have been used to detect and reconstruct the complicated signals present in climate data [MTM – see *Thomson*, 1990; *Kuo et al*, 1990; *Park and Maasch*, 1993; *Mann and Park*, 1993; *Thomson*, 1995, SSA – see *Ghil and Vautard*, 1991; *Yiou et al*, 1991, 1993; *Allen and Smith*, 1994; *Schlesinger and Ramankutty*, 1994; *Lall and Mann*, 1995]. Furthermore, considerable attention has been paid to assure proper null hypothesis testing in climate studies for both SSA [e.g., *Allen and Smith*, 1994] and MTM [*Mann and Lees*, 1996].

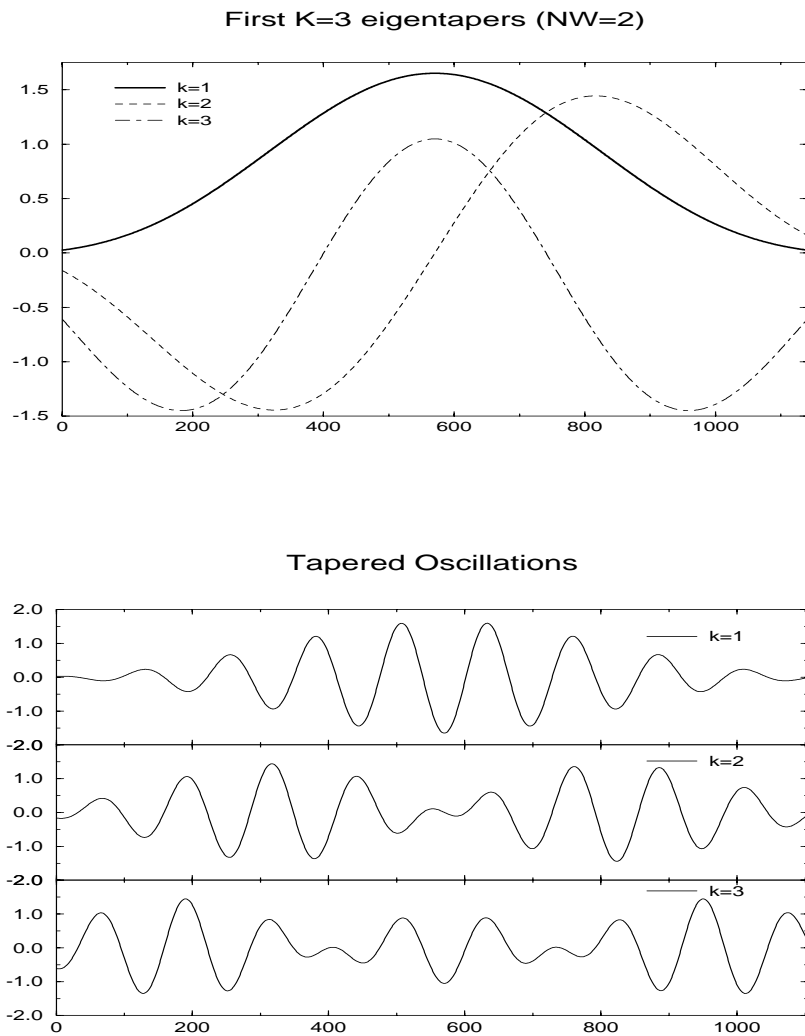


Figure 6: (a) The first three orthogonal Slepian data tapers for the case $K = 3$, $NW = 2$ and (b) the components of a fixed amplitude phase-coherent sinusoidal oscillation described by the modulating envelope associated with each of the $K = 3$ data tapers. [From Mann (1998)].

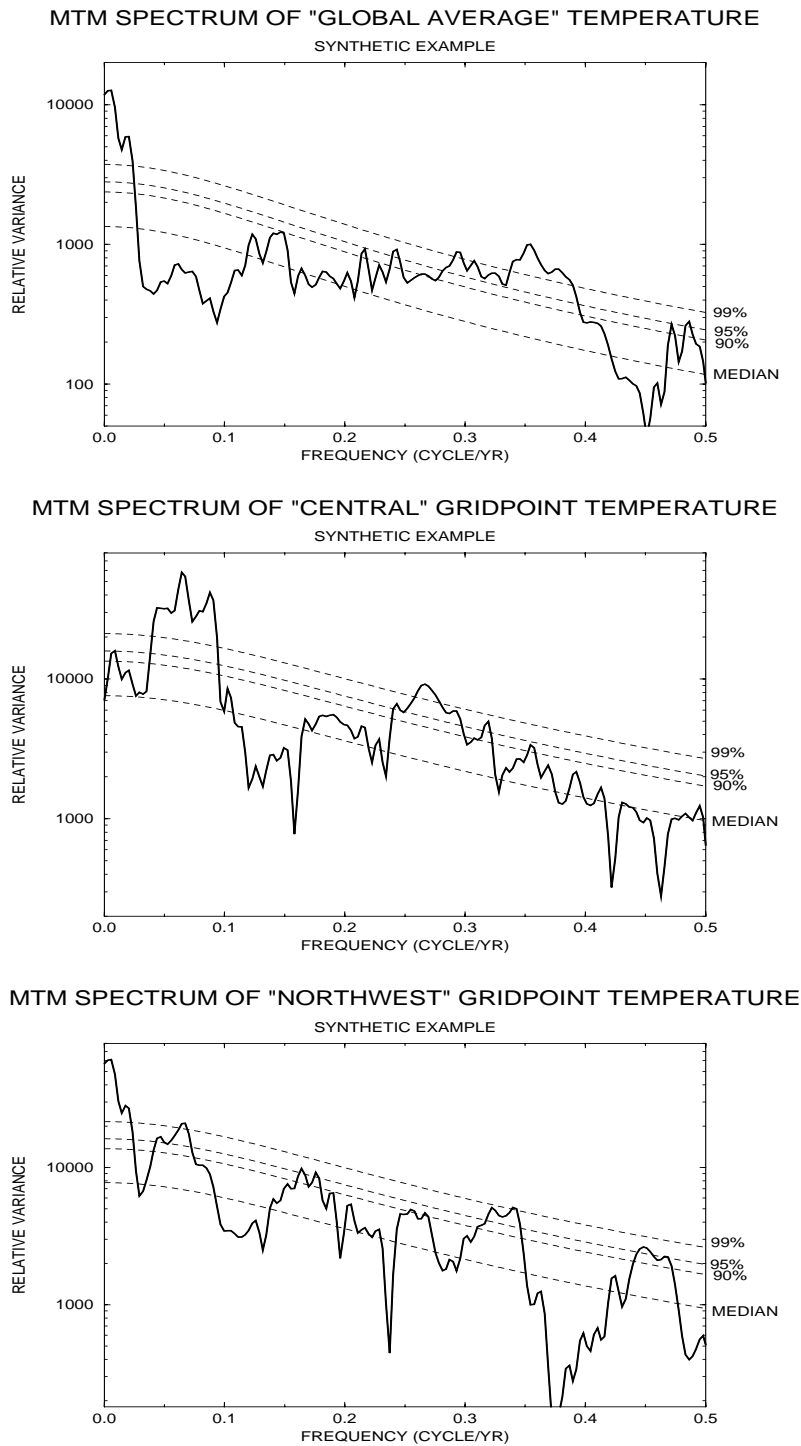


Figure 7: Multitaper spectra of time series from (top) global average over domain (middle) central gridpoint and (bottom) extreme northwest gridpoint, along with robustly estimated median red noise level and 90,95,and 99% confidence limits for significance relative to red noise. [From Mann (1998).]

Rather than focusing on a comparison of these methods [see e.g., *Thomson* 1982; *Ghil and Yiou*, 1996], we here focus on the application of the MTM method to univariate signal detection alone, postponing any inter-method comparison to the discussion of multivariate signal detection techniques and the multivariate generalization of MTM described in section 3.

In the multitaper method, one determines for a given time series $\{x\}_{n=1}^N$, a set of K orthogonal data tapers and K associated tapered Fourier transforms or “eigenspectra”

$$Y_k(f) = \sum_{n=1}^N w_n^{(k)} x_n e^{i2\pi f n \Delta t} \quad (5)$$

where $\Delta t = 1$ month is the sampling interval and $\{w_n^{(k)}\}_{n=1}^N$ is the k th member in an orthogonal sequence of Slepian tapers, $k = 1, \dots, K$. The “time-frequency bandwidth parameter” defined by $NW = p$ defines a particular family of eigentapers. Only the first $K = 2p - 1$ tapers are usefully resistant to spectral leakage, so that the choice of K and p represent a tradeoff between spectral resolution and the degrees of freedom (which can be used to constrain the variance of the spectral estimators). In the context of climate studies of roughly century duration, $NW \equiv p = 2$ and $K = 3$ provide a good compromise [*Mann and Park*, 1994; *Mann and Lees*, 1996] between the resolution appropriate to resolve the natural bandwidths of climatic signals, and the stability of spectral estimates. The set of K tapered eigenspectra have energy concentrated within a bandwidth of $\pm p f_R$ centered on a given frequency f where $f_R = (N\Delta t)^{-1}$ is the Rayleigh frequency. Thus, the choice $p = 2$ provide a full-bandwidth of spectral estimation $\Delta f_{BW} = 2p f_R \approx 0.04$ cycle/year for a 100-year data series. Each of the K eigenspectra represent statistically independent local averages of the spectral information near f , under the assumption of a smoothly varying coloured (“locally white”) spectral backgrounds. As explained in section 2.1, this assumption holds up very well for actual climate data which exhibit a weak-to-moderate red noise background. Figure 6 shows the three orthogonal data tapers for the case $K = 3$, along with a sinusoid modulated by each of the K eigentapers. From the latter plot, it is evident that the multitaper analysis can provide a description of an irregular narrowband oscillatory signal centered at a particular frequency f through the variety of amplitude and phase modulations that can be described by a suitable linear combinations of K independently tapered carrier oscillations. Each of the K spectral degrees of freedom available for each time series at a given frequency f

will provide statistical information in the multivariate extension described in section 3. In univariate applications these independent estimates are combined through a weighted average of the eigenspectral estimates to provide a spectral estimate with optimal spectral resolution/variance tradeoff properties [Thomson, 1982],

$$s(f) = \frac{\sum_{k=1}^K \lambda_k |Y_k(f)|^2}{\sum_{k=1}^K \lambda_k} \quad (6)$$

An “adaptively weighted” estimate of the spectrum can be calculated as

$$s(f) = \frac{\sum_{k=1}^K b_k^2(f) \lambda_k |Y_k(f)|^2}{\sum_{k=1}^K b_k^2(f) \lambda_k} \quad (7)$$

where b_k is a data-adaptively determined weighting function of the eigenspectra that seeks to minimize broad-band leakage in the spectrum [Thomson, 1982].

We here show the results of univariate MTM spectral analysis applied to the problem of detecting signals in the synthetic data set (Figure 7). We use the procedure of *Mann and Lees* [1996] to provide robust estimates of the estimated red noise background and significances of narrowband peaks. Since the phase of each oscillation varies over the spatial grid, there is some cancellation of the oscillatory components in the average across series. Note that the MTM spectra of the “global average” does not detect the interdecadal signal, constructed to vanish in a global average, as significant. Partial phase-cancellation of other signals also diminishes the usefulness of large-scale spatial averaging. Although interdecadal and interannual peaks are detected for the “reference” gridpoint, the secular trend, small at that gridpoint, is not recognized as significant at the 95% level. The secular trend and interdecadal peak are clearly detected in the spectrum for the “northwest” grid point, but it is difficult to identify any consistent interannual peaks in this spectrum or that of the “reference” gridpoint, and there are several spurious peaks (sampling fluctuations from the noise background) that rival the true signals in their prominence. Thus, on one hand, large-scale spatial averaging is often an ineffective means of signal/noise ratio enhancement. On the other hand, signal-to-noise ratios in the univariate “regional” signal detection approach are too low for consistent detection of large-scale signals. It is thus clear that the mutual information available in the spatially distributed data must be used in a more sophisticated way for effective spatiotemporal signal detection. This is particularly true in exploratory analysis where the spatial structures at different frequencies are not known *a priori*.

PCA+Spectral Analysis

A common approach to spatiotemporal signal detection in geophysical applications is based on some variant of Principal component analysis (PCA), in which a Singular Value Decomposition (SVD) is performed on the data matrix followed by spectral analysis (“PCA+SA”) of the time series of the independent spatial modes [Trenberth and Shin, 1984; Deser and Blackmon, 1993; Tanimoto et al, 1993; Venegas et al, 1996].

Consider a set of individual data series $x^{(m)}$ ($m = 1, 2, \dots, M$) of length N time units (e.g., months or years) centered to represent departures from the respective long-term means. Typically, each series is normalized by its standard deviation. The resulting demeaned and normalized series are termed “standardized” series.

The standardized spatiotemporal data can then be written as a data matrix

$$\underline{\mathbf{X}} = \begin{bmatrix} w_1 x_{t_1}^{(1)} & w_2 x_{t_1}^{(2)} & \dots & w_M x_{t_1}^{(M)} \\ w_1 x_{t_2}^{(1)} & w_2 x_{t_2}^{(2)} & \dots & w_M x_{t_2}^{(M)} \\ \vdots & & & \\ w_1 x_{t_N}^{(1)} & w_2 x_{t_N}^{(2)} & \dots & w_M x_{t_N}^{(M)} \end{bmatrix} \quad (8)$$

where t_1, t_2, \dots, t_N spans over the N time samples, and $m = 1, 2, \dots, M$ spans the M (e.g., individual gridpoint) different series. w_m might, for example, indicate weightings by gridpoint area.

The data matrix is decomposed by Singular Value Decomposition,

$$\underline{\mathbf{X}} = \sum_{k=1}^M \lambda_k \mathbf{u}_k \mathbf{u}_k^\dagger \mathbf{v}_k \quad (9)$$

into its dominant spatiotemporal eigenvectors, where the M -vector or empirical orthogonal function (EOF) \mathbf{v}_m describes the relative spatial pattern of the m th eigenvector, the N -vector \mathbf{u}_m or principal component (PC) describes its variation over time, and the eigenvalue (the square of the singular value) λ_m is the associated fraction of described data variance. The dagger on the vector \mathbf{u}_m indicates the conjugate transpose.

We demonstrate the application of PCA to the synthetic dataset described in section 2.1. Four eigenvalues (each indicating the fractional data variance explained by an associated empirical eigenvector which describes the temporal variation of a particular fixed anomaly pattern) are established as significant relative to spatially-correlated noise in the multivariate dataset (Figure 8). The significance criterion is

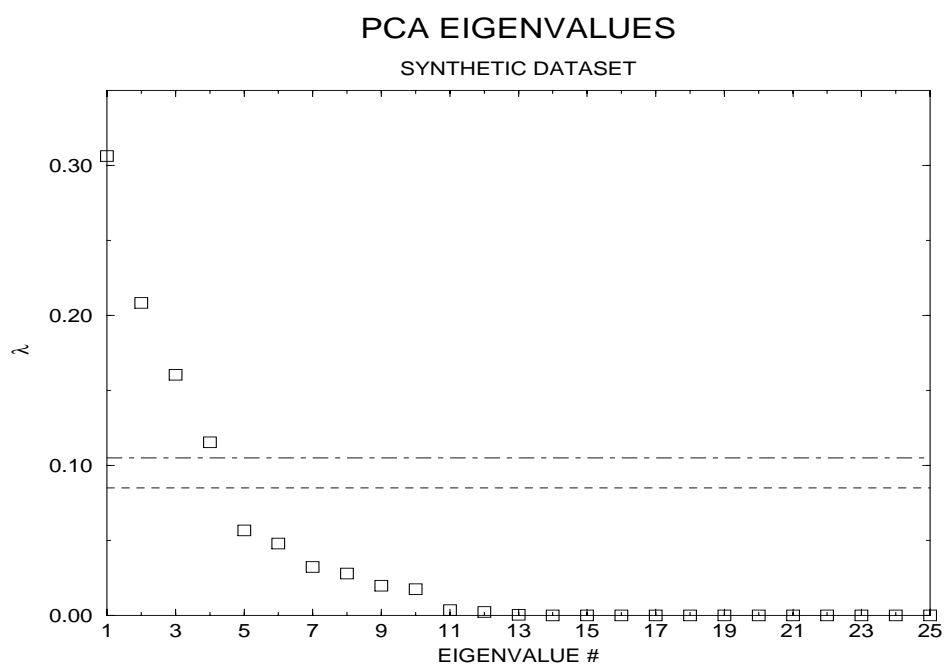


Figure 8: Eigenvalue spectrum of the PCA decomposition of the synthetic dataset. 4 eigenvectors are indicated as being statistically significant taking into account spatial autocorrelation of the gridpoint data. Thresholds for significance are shown based on the two different calculations described in the text. [From Mann (1998)].

based on the PCA selection “rule N”, modified to take into account the reduction in spatial degrees of freedom owing to spatial autocorrelation [Preisendorfer, 1989]. Estimating a spatial decorrelation scale of $d = 1.5$ gridpoints, leads to $N' \approx N/d = 11.7$ so that only eigenvectors with $\lambda > 1/N' = 0.085$ are to be retained. Furthermore, there is a clear break in the eigenvalue spectrum from its red noise floor between eigenvalues 4 and 5, so the selection of 4 eigenvectors seems quite natural in this case.

The decomposition provided by PCA exhibits several clear shortcomings. An immediate problem is that the PCA procedure detects 4 significant statistically independent modes of variation in the data when we know *a priori* that only 3 modes of variation are distinct from the red noise background.

Furthermore, the power spectra of the statistically significant PCs (Figure 9) present a muddled picture of signal and noise in the dataset. PC #1 describes a pattern of variability which exhibits dual dominant timescales including a significant trend and significant narrowband variance in the 3-5 year interannual range. The reader will note a striking similarity to the spectrum of the globally-averaged data shown earlier in Figure 7 (top). The PC #1, to a very good degree of approximation, describes the globally in-phase mode of variation in the dataset. This component is slightly different from the global mean because variations that are 180 degrees out of phase project oppositely onto the global mean. Thus, the principal mode of the PCA has no simple “physical” interpretation, representing a combination of incomplete projections of two of the signals – secular trend and interannual signal – which project onto the global mean. PCs #2,3, and 4 describe various combinations of the residual, spatially-heterogeneous component of the multivariate data. The modulated interdecadal oscillation appears as a peak of varying prominence in each of these 3 PCs. The interannual signal is scattered in varying degree among each of the PCs. The noise background, furthermore, is not consistently decomposed among the 4 PCs, with PC #3 exhibiting a considerably whiter noise background than the others. The mis-identification of signal and noise arises here results from fundamental weaknesses in the PCA+SA signal-detection approach. The primary weakness results from the performance of two consecutive statistical operations which have conflicting optimality properties. PCA performs a time-optimal variance decomposition through a Karhunen-Loeve expansion of the dataset in the time domain, appropriate for a random or broadband multivariate process. However, as discussed

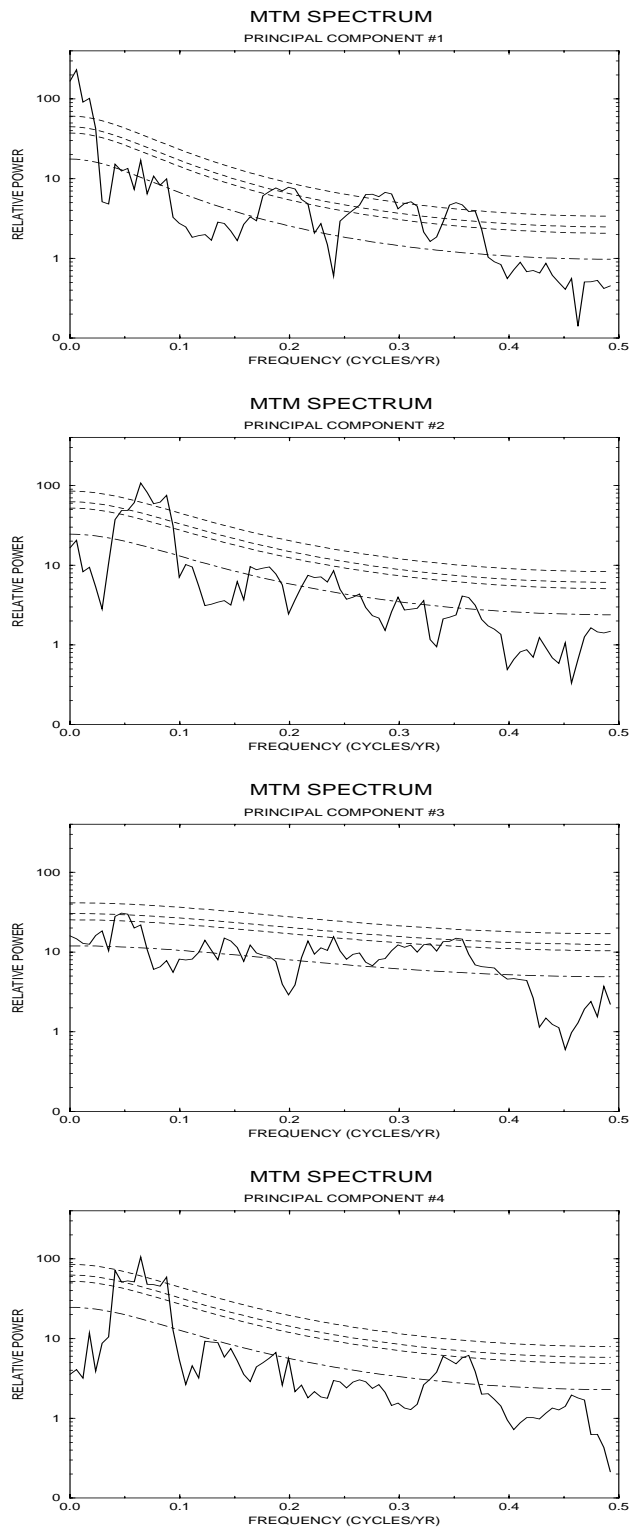


Figure 9: Multitaper spectra of the significant principal components (1-4) along with significance levels relative to red noise. [From Mann (1998).]

earlier, there is considerable evidence for narrowband processes in observed climate data with characteristics similar to those we have imposed in our synthetic example. When such narrowband frequency-domain structure is present, the thoroughly unoptimal frequency-domain properties of the time-domain decomposition become apparent [see the discussion by *Brillinger*, chapter 9, 1981]. In contrast, a frequency-domain Karhunen-Loeve expansion provides an optimal decomposition of the data variance for this latter case [*Thomson*, 1982]. The combination of a red noise background and narrowband multivariate processes in the synthetic dataset thus cannot be efficiently separated in the PCA+SA approach. Furthermore, because there is no phase information (see however, the “complex” PCA method described below) in the PCA decomposition, the propagating phase structure in the signals cannot be correctly described by the empirical eigenvectors. Rather, the eigendecomposition must artificially describe such phase information in terms of multiple standing waves.

Nonetheless, a variety of generalizations of PCA have been developed which attempt to ameliorate several of the problems noted above, through various modifications or alternative spatiotemporal variance decompositions. Below we discuss such methods, pointing out the relative strengths and weaknesses of each approach, and emphasizing those particular weaknesses or limitations which are overcome by the MTM-SVD approach described in section 3.

Multivariate AR

While typically applied to the problem of spatiotemporal interpolation of data fields in climate studies [e.g., *Wikle and Cressie*, 1996; *Kaplan et al*, 1997], Markovian (ie, AR(1) or higher order AR) spatiotemporal models do also provide a means of multivariate spectrum estimation and signal detection [see *Marple*, 1987]. Such multivariate AR methods of spectral analysis offer the drawback however that (a) they assume strict stationarity of the data and (b) provide less than optimal resolution/variance tradeoff properties in spectral estimation.

Principal Oscillation Patterns

Principal Oscillation Patterns or “POP”s [*Hasselmann*, 1988; *Penland*, 1989; *Xu*, 1993; *Von Storch et al*, 1995] exploit Markovian structure in the data in a dynamical context distinct from that of the conventional multivariate AR approach.

“POPs” offer a philosophical appeal under certain assumptions for the governing dynamics; they invoke a specific dynamical model – stochastically forced damped linear oscillatory behavior – in multivariate spectral estimation. Furthermore, POPs are readily generalized to incorporate spatially-variable phase information (complex POPs or “CPOP”s-see *Bursor* [1993]). As long as the underlying model of stable linear dynamics is appropriate, and the climatic data series to be analyzed are long, POPs or CPOPs provide a useful means of signal detection. On the other hand, the specificity of the subsumed inverse model limits the usefulness of POPs as an exploratory data analysis tool, when the correct dynamical model describing signals cannot be specified *a priori* or when the exact underlying noise spectrum is not known. The POP approach, furthermore, is not optimized to guard against the biases (i.e., spectral leakage) known to exist in the spectrum estimation of finite time series [*Thomson*, 1982], and will provide unoptimal signal vs. noise decompositions for relatively short and noisy time series.

Extended EOFs

Extended EOFs [*Weare and Nasstrom*, 1982; *Graham et al*, 1987; *Preisendorfer*, 1988] identify the dominant spatiotemporal structure of lagged sequences of covariance estimates. Such a decomposition can thus capture time-evolving patterns in the data, since phase information is retained in the decomposition. The approach is useful to recover oscillatory patterns that are known to exist in the data, but cannot be used to detect spatiotemporal signals themselves without further generalization (see “Multichannel SSA” below).

Rotated EOFs + Spectral Analysis

Through selecting alternative rotated combinations of the eigenvectors obtained through PCA (e.g., “varimax rotation” [e.g., *Richman*, 1986; *Houghton and Tourre*, 1992] one can often obtain spatial patterns which may bear a closer relationship to particular, physically-based modes of variability (e.g, the dynamical pattern of ENSO). To the extent that such rotation may allow for a more natural separation of the data into physically meaningful patterns, the PCA+SA procedure used above can be combined with a rotation procedure to provide a more faithful separation of the true signals in the data, and a more faithful signal detection procedure. Such a rotation is however subjective, requiring some *a priori* assumptions regarding the

spatial patterns that are of physical significance (e.g., in the case of varimax rotation, that spatial structures of signals should be regionally localized). Objective selection rules for significance in PCA are also lost upon rotation. In some sense, rotation of EOFs prior to spectral analysis is an imperfect solution to the more fundamental problem that PCA provides only a time-domain optimal decomposition of the data variance, unable to appropriately recognize frequency-domain organization.

Complex Harmonic PCA

A complex generalization of PCA known as “complex harmonic PCA” or “CH-PCA” [see e.g., *Wallace and Dickinson, 1972; Barnett 1983; Trenberth and Shin 1984; Barnett 1991, Preisendorfer, 1988* – see also “principal components in the frequency domain” (chapter 9) in *Brillinger, 1981*] provides a better description of oscillatory features in a multivariate dataset than does conventional PCA. The CH-PCA procedure makes use of PCA on a matrix analogous to that defined by (2.7) but containing instead appropriately estimated complex spectral estimates $y^{(m)}$ of the data series $x^{(m)}$ at all resolvable frequencies,

$$\underline{\mathbf{Y}} = \begin{bmatrix} y_{f_0}^{(1)} & y_{f_0}^{(2)} & \cdots & y_{f_0}^{(M)} \\ y_{f_1}^{(1)} & y_{f_1}^{(2)} & \cdots & y_{f_1}^{(M)} \\ \vdots & \vdots & \vdots & \vdots \\ y_{f_{N-1}}^{(1)} & y_{f_{N-1}}^{(2)} & \cdots & y_{f_{N-1}}^{(M)} \end{bmatrix} \quad (10)$$

A PCA is then performed in the transformed, frequency domain,

$$\underline{\mathbf{Y}} = \sum_{n=1}^N \lambda_n \mathbf{u}_n \dagger \mathbf{v}_n \quad (11)$$

where n in this context runs over the N distinct frequencies of the Discrete Fourier Transform of a dataset of length N samples. The empirical orthogonal function (EOF) \mathbf{v}_m describes the complex spatial pattern in amplitude and phase of the n th eigenvector, and the N -vector \mathbf{u}_m now describes the combinations of pure harmonic components of variability that describe the relatively smooth time-evolution of the n th eigenvector. The eigenvalue (the square of the singular value) λ_m as before describes the associated fraction of data variance. Because phase information is maintained in this procedure, standing and traveling oscillatory signals in the dataset are described more faithfully [see *Preisendorfer, 1988, chapter 12*]. The

primary limitation of “CH-PCA” is that spectral estimates for the neighboring frequency estimates treated as independent random variables are in fact correlated, introducing a statistical dependence that is difficult to assess in interpreting the results of the eigendecomposition. Furthermore, modulated or irregular oscillations are not appropriately modeled.

Bandpass-filtered PCA

In what can be viewed as an alternative to CH-PCA, a technique for identifying narrowband but anharmonic oscillatory features in the data is to pre-filter with a bandpass over the frequency interval of interest [e.g., *Trenberth and Shin, 1984*], seeking to determine if there is a single dominant mode of variability within that restricted frequency band. While this approach does allow the detection of irregular narrowband oscillations, some of the more fundamental problems noted earlier for PCA+SA are not circumvented. In particular, because phase information is lost in the PCA, only standing oscillations can be described by any particular eigenmode. Furthermore, though bandpassing alleviates the most serious problems in PCA of successive operations of frequency domain-optimized filtering (bandpassing) followed by time-optimal filtering (time-domain PCA of the data), the conventional filtering procedures invoked [e.g., the Hilbert Transform – see *Preisendorfer, 1988*] provide less than optimal spectral resolution/variance tradeoff properties [e.g., *Thomson, 1982*].

Multichannel SSA

The approach of Multichannel SSA or “M-SSA” [*Keppenne and Ghil, 1993; Allen and Robertson, 1996; Moron et al, 1997*], as in the method of extended EOFs described earlier, employs a multivariate correlation-space eigenvector decomposition to describe evolving spatially-correlated structures in a multivariate dataset. Indeed, the terminology of “extended EOFs” and “M-SSA” is sometimes used interchangeably [*Allen and Robertson, 1996*] We will draw a distinction, however, using “M-SSA” to describe the more general procedure of estimating the statistical significance (relative to a specified noise null hypothesis) of spatiotemporal oscillations detected in the lagged estimates of the data covariance matrix. Beyond detecting significant irregular spatiotemporal oscillations in a multivariate dataset, M-SSA provides a direct link to the theoretical framework of non-linear dynamical systems

[see *Vautard and Ghil, 1989; Ghil and Yiou, 1996*]. The approach provides an optimal decomposition in the correlation domain, and not in the frequency domain [note the explicit comparisons of *Thomson, 1982*, of correlation-domain and frequency-domain estimators]. SSA (and its multivariate counterpart “M-SSA”) can usefully analyze only those quasi-oscillatory structures with periods in the range $[L/5, L]$ where $L = N/3$. [see *Vautard et al, 1992*] where L is the embedding dimension for the lagged-covariance estimation (equivalently, the width, in time units, of an equivalent moving window through the time series). Consequently, there are rather severe restrictions on the range of frequency bands over which temporal structure can be reconstructed simultaneously. For instance, to recover interdecadal patterns (approximate period 20 years), one may want to choose $L = 30$ years with a 100 year record. This window width will not allow the reliable decomposition of oscillatory signals (e.g., ENSO) with dominant timescales less than 6 years in this case. More importantly, in the multivariate context, M-SSA approach runs up against severe dimensional limitations for large datasets. The introduction of multiple channels in the covariance estimation requires the statistical decomposition of a matrix in the time, spatial index, and lag domains. For a fixed duration data series of length N and M channels (e.g., gridpoints), this requires the SVD of an $N \otimes ML$ matrix, which quickly becomes ill-posed (i.e., a unique eigendecomposition of the variance is not possible) as the number of spatial channels M becomes large. To avoid this problem, the spatial dataset must first be further decomposed into a lower-dimensional representation (e.g., by conventional PCA) before the M-SSA algorithm is applied [*Vautard et al, 1992; Moron et al, 1997*]. This latter step then tends to reintroduce some of the limitations of classical PCA noted above which we seek to avoid. In this sense, the usefulness of M-SSA becomes limited for spatially-extensive datasets.

3. MTM-SVD Multivariate Frequency-Domain Climate Signal Detection and Reconstruction

The multitaper frequency-domain singular value decomposition or “MTM-SVD” approach [*Mann and Park, 1994; Mann et al, 1995ab; Mann and Park, 1996ab*] exploits the optimality of multitaper spectral analysis for analyzing narrow band signals superposed on a smoothly-varying spectral noise background [see section 2.1]. The MTM-SVD approach seeks to isolate statistically significant narrowband

oscillations (which may be modulated or “irregular” in nature) that are correlated among a sufficiently large number of normalized independent series or “channels” (e.g., multiple gridpoints) as to comprise a significant fraction of the total data variance. The approach invokes a null hypothesis of a smoothly-varying coloured noise background, rejecting the null hypothesis when a large share of the multivariate data variance within a specified narrow frequency band can be attributed to a particular mode (i.e., modulated spatiotemporal oscillation) of variability. The approach can be appropriately modified with an “evolutive” generalization to describe broader-band and frequency-modulated processes [see *Mann et al*, 1995b; *Mann and Park*, 1996b]. Wavelet-based generalizations of the procedure more appropriate for the description of episodic variability have also been developed [*Lilly and Park*, 1995; *Park and Mann*, 1997].

As the MTM-SVD approach is complex-valued in nature, it naturally describes spatially-correlated oscillatory signals with arbitrary spatial relationships in both amplitude and phase. In this manner, the approach can distinguish standing and traveling oscillatory patterns in a spatiotemporal dataset. The multitaper decomposition also allows for a relaxation of the typically strict stationarity assumptions invoked in most spatiotemporal decompositions. The optimal frequency-domain properties of multitaper spectral analysis enables the procedure to provide superior signal detection and signal/noise separation under the assumption of narrowband signals and the null hypothesis of a spatially correlated coloured noise background with a smoothly varying spectrum. Moreover, because the methodology allows for the detection of either periodic or aperiodic irregular oscillatory patterns, it does not invoke restrictive assumptions regarding the governing dynamics. The characteristics of amplitude-, phase- and frequency-modulated spatiotemporal oscillations assumed in the associated statistical model of “signal”, for example, accommodates the description of stochastically excited linear climate oscillations and self-sustained non-linear oscillations equally well. Thus, the MTM-SVD technique provides a philosophical appeal over conventional multivariate techniques in an exploratory data analysis setting.

In this section, we describe details of MTM-SVD method, including the techniques for signal detection, signal reconstruction, and confidence level and significance estimation. We demonstrate that the method provides the correct null inferences when applied to a class of spatially-correlated coloured (red) noise processes.

Finally, we demonstrate highly successful spatiotemporal signal detection and reconstruction when the method is applied to the synthetic signal+noise example described in section 2.1.

3.1 Signal Detection

The MTM-SVD signal detection method makes use of the mutual information available from each of the K spectral estimates available at each frequency f in a multivariate dataset of “spatial dimension” M . Rather than averaging the estimates of the distinct K eigentapers as in equations (2.5) and (2.6), the MTM-SVD approach retains the independent statistical information provided by each of the K eigenspectra, and seeks to find the optimal linear combinations of eigentapers that maximize the multivariate variance explained by a particular amplitude/phase modulation of a given carrier frequency component. The availability of multiple independent spectral estimates for each time series at a given frequency f is the fundamental requirement for the orthogonal decomposition employed in the MTM-SVD approach, and in almost all cases, the minimum value of the time-frequency bandwidth parameter $NW = 2$ is used which admits ($K = 3$) such multiple degrees of freedom. This choice insures minimal loss of frequency resolution. The reader is referred back to the discussion of section 2.2 and Figure 6. The decomposition describes a carrier oscillation modulated by a complex envelope function with K degrees of freedom, allowing for the description of modulated, irregular oscillations while providing the optimal spectral resolution/variance tradeoff of multitaper spectral analysis.

We “standardize” each of the series to be analyzed by removing the mean over the N samples to yield an “anomaly” series $\{x'_n\}^{(m)}$ and normalize the resulting series by its standard deviation $\sigma^{(m)}$, where $n = 1, \dots, N$ and N is number of samples (e.g., $N = 1200$ for 100 years of monthly data). This normalization favors the detection of spatially-coherent processes. To represent the data in the frequency domain, we calculate the multitapered Fourier transforms for each normalized time series $x_n^{(m)} = x'_n{}^{(m)}/\sigma^{(m)}$

$$Y_l^{(m)}(f) = \sum_{n=1}^N w_n^{(l)} x_n^{(m)} e^{i2\pi f n \Delta t} \quad (12)$$

for a given choice of K and the time-frequency bandwidth product $NW = p$, as in the univariate multitaper procedure (see equation 2.4). Because secular variations

are separated from higher-frequency variability with minimum spectral leakage, non-stationarity of the first order (e.g., a linear trend in the data) can be described with little bias on the rest of the spectrum, without any detrending or “pre-whitening” of the data series. Thus, the decomposition avoids the strict stationarity requirements of most statistical time series decompositions.

The $M \times K$ matrix,

$$\mathbf{A}(f) = \begin{bmatrix} w_1 Y_1^{(1)} & w_1 Y_2^{(1)} & \dots & w_1 Y_K^{(1)} \\ w_2 Y_1^{(2)} & w_2 Y_2^{(2)} & \dots & w_2 Y_K^{(2)} \\ \vdots & & & \\ w_M Y_1^{(M)} & w_M Y_2^{(M)} & \dots & w_M Y_K^{(M)} \end{bmatrix} \quad (13)$$

is formed with each row calculated from a different grid point time series, and each column using a different Slepian taper. The w_m represent spatially-variable weights to adjust for relative areas of gridpoints, etc.

To isolate spatially-coherent narrowband processes, a complex singular value decomposition [e.g., *Marple*, 1987] is performed of the above matrix,

$$\underline{\mathbf{A}}(\mathbf{f}) = \sum_{k=1}^K \lambda_k(f) \mathbf{u}_k(\mathbf{f})^\dagger \mathbf{v}_k \quad (14)$$

into K orthonormal M -vectors \mathbf{u}_k , representing complex spatial empirical orthogonal functions (“spatial EOFs”), and K orthonormal K -vectors \mathbf{v}_k [termed “spectral EOFs” by *Mann and Park* 1994] which we will term here “principal modulations” in analogy with “principal components” of a time-domain eigendecomposition. Because the SVD is a multi-linear decomposition, this approach posits a linear spatial relationship among all time series (e.g., spatial gridpoints) in any given signal. Any regional responses which are non-linearly related to the large-scale signal may be imperfectly described by the estimated signal spatial pattern. The “principal modulations” describe the linear combination of projections of the K eigentapers which impose the amplitude and phase modulation of the oscillatory behavior associated with the k th mode. The key distinction between CH-PCA and MTM-SVD is that the MTM-SVD technique performs a *local* frequency-domain decomposition of K statistically independent spectral estimates as defined by equation 13, whereas CH-PCA performs a *global* frequency-domain decomposition over all spectral estimates (compare equation 10). This distinction is the primary reason that the MTM-SVD technique can be used to isolate irregular oscillations superposed on an *arbitrary* smoothly varying coloured noise background.

The singular value $\lambda_k(f)$ scales the amplitude of the k th mode in this local eigendecomposition, where the K singular values are ordered $\lambda_1(f) \geq \lambda_2(f) \geq \dots \lambda_K(f) \geq 0$. The associated “eigenvalues” are the $\lambda_k^2(f)$. The normalized principal eigenvalue, $\lambda_1^2(f)/\sum_{j=2}^K \lambda_j^2(f)$ provides a signal detection parameter that is *local* in the frequency domain. Under the assumption that no more than one signal is present within the narrow bandwidth of spectral estimation, the normalized principal eigenvalue should stand out distinctly above what would be expected from an appropriate noise model. In the relatively unlikely event that there exist two similarly strong signals within a single bandwidth, the usefulness of this detection parameter will be diminished. We refer to the normalized principal eigenvalue as a function of frequency as the “local fractional variance spectrum” or “LFV” spectrum. The LFV spectrum varies between $1/K$ and unity in magnitude, and has a variable frequency bandwidth $\Delta f_{MTM-SVD}$ between $\pm f_R$ and $\pm p f_R$, as it can be no more narrow than the Rayleigh resolution f_R and no greater than the bandwidth corresponding to a uniform average of the K eigenspectra (i.e., Δf_{BF} defined in section 2.1). Correspondingly only variability with period shorter than $N\Delta t/p$ (e.g., 50 years for 100 years of data and $NW = 2$) can be confidently distinguished from a secular variation. This multivariate spectrum provides a powerful frequency-domain signal detection parameter, indicating the maximum fraction of narrowband spatiotemporal variance that can be explained by a particular modulated oscillation as a function of frequency. Typically, only this principal eigenvalue spectrum is used as a signal detection parameter. An iterative procedure may be advised if there is reason to believe that multiple signals may be present in a particular narrow frequency band. For example, *Mann and Park* [1994;1996b] use this latter procedure to identify two significant secular variations in instrumental climate data of the past century (see section 4.1 for more details regarding this iterative procedure). As discussed below, the frequency-independent nature of the distribution of LFV for a wide range of coloured noise processes provides for fairly unrestrictive null hypothesis testing, and the use of powerful non-parametric significance estimation procedures.

3.2 Signal Reconstruction

The spatial pattern of a signal associated with a significant peak in the LFV spectrum at frequency $f = f_0$ is described by the complex-valued M -vector, \mathbf{u}_1 which

indicates the relative amplitude and phase of the signal at particular locations (e.g., grid points) of the multivariate dataset. Using the envelope estimate $\tilde{A}_1(f_0, t)$ (see equation 17), the reconstructed spatiotemporal signal \tilde{y} is described by,

$$\tilde{x}_n^{(m)} = \gamma(f_0) \Re \left\{ \sigma^{(m)} u_1^{(m)} \tilde{A}_1(n\Delta t) e^{-i2\pi f_0 n\Delta t} \right\}, \quad (15)$$

where $u_1^{(m)}$ is the m th component of the spatial EOF $\mathbf{u}_1(f_0)$. The factor $\gamma(f_0) = 2$ for $f_0 \geq pf_R$, owing to contributions from spectral information near f_0 and $-f_0$. At $f_0 = 0$, $\gamma(f) = 1$. For $0 < f_0 \leq pf_R$, the value of γ is more problematic, as the sampling widths of the Slepian tapers in the frequency domain for f_0 and $-f_0$ overlap partially. In practice, it is simplest to treat such long-period variability as quasi-secular and use the $f_0 = 0$ passband for its reconstruction.

The canonical spatial pattern of the signal can be represented by the complex field,

$$\hat{x}^{(m)} = \gamma(f_0) \sigma^{(m)} u_1^{(m)} A_{rms}(f_0) \quad (16)$$

where the pattern is scaled by the root-mean-square amplitude $A_{rms}(f_0)$ of the modulating envelope $\tilde{A}_1(f_0, t)$ (because of amplitude modulation, the amplitude of the pattern is variable from cycle to cycle). This reconstructed pattern describes the evolving spatial pattern over a cycle, and can thus be represented by a complex-valued pattern [see e.g., *Mann and Park, 1994*], with the magnitude of the vector indicating relative amplitude and the angle indicating relative phase (i.e., relative timing of peak/minimum anomaly at a particular location for a particular variable). This information is often more physically portrayed in terms of a sequence of real-valued anomaly patterns (positive or negative values of the anomaly field) corresponding to the projection of the complex spatial vector onto various phases of a cycle [e.g., *Mann and Park, 1996b*].

The complex-valued K -vector \mathbf{v}_1 can be inverted to obtain the slowly varying envelope of the signal, similar to the complex demodulate. *Park* [1992] and *Park and Maasch* [1993] show how the slowly varying envelope $A(t)$ of an oscillatory signal $x(t) = \Re\{A(t)e^{-i2\pi f_0 t}\}$ centered at a “carrier” frequency f_0 can be estimated from a set of eigenspectra $Y_l(f_0)$, $l = 1, \dots, K$. The time domain signal $x(t)$ and envelope $\Re A(t)$ are formally identical for modes referenced to $f_0 = 0$, that is, the secular modes of variability. In the multivariate case, the time-domain signal is reconstructed from the components of its corresponding spectral EOF $\mathbf{v}_1^*(f_0)$. This

reconstruction is not unique and requires additional constraints. The simplest reconstruction is an MTM version of the complex demodulate, a linear combination of the Slepian tapers $\{w_n^{(l)}\}_{n=1}^N$

$$\tilde{A}_1(n\Delta t) = \sum_{l=1}^K \xi_l^{-1} \lambda_l(f_0) (v_1^{(l)})^* w_n^{(l)}, \quad (17)$$

where $v_1^{(l)}$ is the l th component of the vector $\mathbf{v}_1(f_0)$. The ξ_l are the bandwidth retention factors of the Slepian tapers [see *Park and Maasch, 1993*]. This reconstruction tends to minimize the size of the envelope and thus favors $\tilde{A}_k \rightarrow 0$ at the ends of the time series. Such an inverse clearly is not appropriate for signals associated with nonstationarity in the mean (i.e., a secular trend). A second possible inversion minimizes the numerical first derivative of $\tilde{A}_1(n\Delta t)$ [*Park, 1992*], which favors envelopes that approach zero slope at the ends of the time series. Such an inversion does not discriminate against a zero-frequency trend in the data, for example, but is suited poorly for other describing features which change rapidly near the beginning or end of the data series. A third possible constraint minimizes the roughness of the envelope using the second derivative of $\tilde{A}_1(n\Delta t)$, which constrains neither the mean nor the slope near the ends of the data. *Mann and Park [1996]* favor a more general data-adaptive means of time-domain signal reconstruction in which the mean-square multivariate misfit with the raw data is minimized over all possible linear combinations of these 3 constraints. This approach removes the subjective reliance on some particular *a priori* boundary condition assumption and has been shown to provide optimal skill in a forecasting context [*Rajagopalan et al, 1997*].

For the evolutive procedure, the temporal reconstructions are performed separately in a sequence of staggered windows or “moving window” of specified width through the entire data series. The width of the window is typically chosen so that it includes multiple periods of the oscillatory signal of interest, but is short enough to capture the evolution of frequency and amplitude features over the duration of the record. As an example, to study interannual (say, 3-5 year) oscillatory behavior associated with ENSO based on roughly century duration records, we typically invoke a 40 year window in the evolutive procedure. The temporal reconstruction is in this case determined by a multivariate projection filtering [*Thomson 1995; Mann and Park 1996a*] using the reconstructions from overlapping intervals of adjacent windows. The spatial reconstruction for an evolutively determined signal (representing the “average” relative spatial phase and amplitude pattern of the signal) is

determined by averaging the spatial patterns over multiple windows from the beginning to end of the full data interval. In this case, the relative spatial patterns (in both amplitude and phase) vary somewhat over time, consistent with the possible non-stationarity of certain climate process [see for example, the discussion of secular changes in the characteristic effect of ENSO on precipitation patterns in certain regions by *Ropelewski and Halpert* [1987]. For such cases, either the spatial pattern corresponding to a particular window of time when the signal is strongest, or the average pattern over all windows, may be of most interest.

3.3 Testing the Null Hypothesis: Significance Estimation

The statistical significance of potential signals in the LFV spectrum requires an accurate estimate of the expectations from chance coincidence, given an appropriate null hypothesis. Following the earlier discussion of section 2.1, the least restrictive null hypothesis that might be adopted is that the observed behavior arises from the statistical fluctuations of a spatiotemporal noise process with an arbitrarily coloured noise background and a spatial correlation structure estimated empirically from the data set itself. The significance of putative narrowband signals detected in the LFV spectrum is estimated by diagnosing the likelihood that a given value of the LFV would arise from random fluctuations of such a process. Spatial correlation in the climate noise background which is largely local, but, to a lesser extent, at the larger planetary wave scale also, strongly limits the true number of spatial degrees of freedom in the sampling of any climatic field. If such spatial correlation of the noise is not properly accounted for, incorrect significance level estimation and spurious signal detection (ie, peaks in the LFV spectrum) are likely. We guard against contaminations from long-range spatial correlations in the climate background noise by a bootstrap resampling of the multivariate data in time. This resampling destroys temporal, but not spatial, structure in the data set. Thus, MTM-SVD analysis of many independent time-resamplings of a multivariate data set can be used to calibrate the LFV confidence levels.

The LFV spectrum measures, within a narrow frequency band, the amplitude of the largest spatially-correlated oscillatory “signal” relative to oscillations with other spatial patterns and temporal modulations. To be used as a signal detection parameter, the statistical significance of local peaks in the LFV spectrum is established by estimating the corresponding null distribution of the LFV parameter

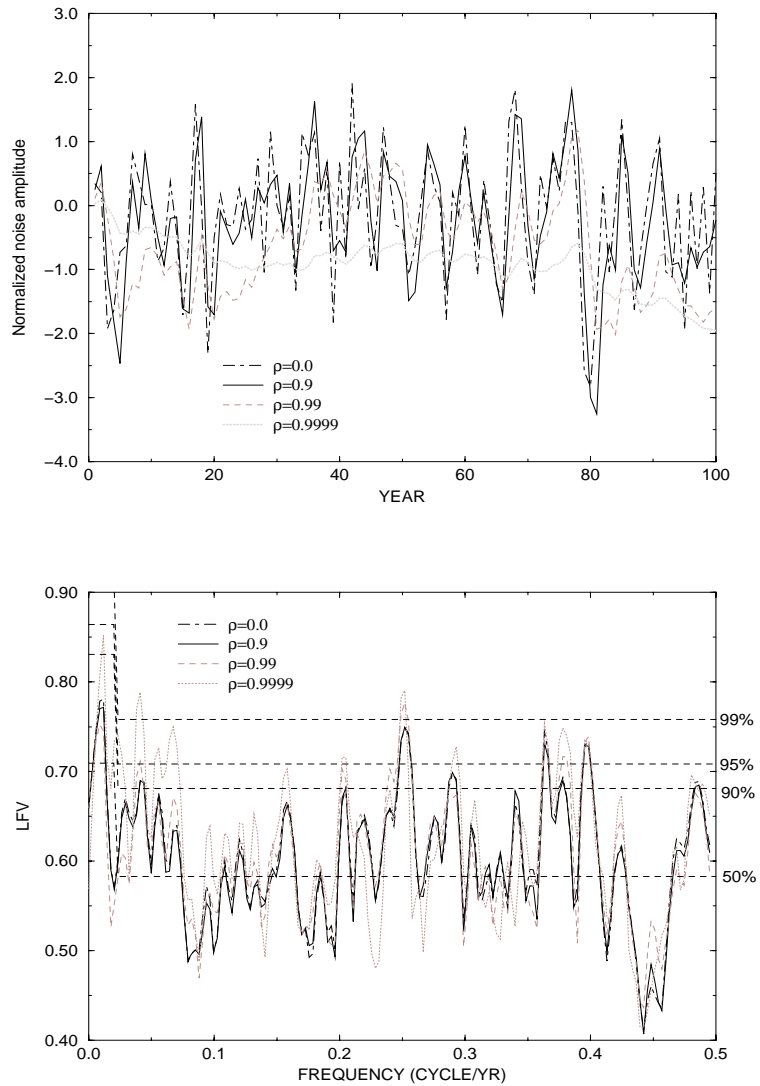


Figure 10: (top) Center gridpoint annual mean reference series for spatiotemporal noise realization with varying levels of autocorrelation ρ . (bottom) LFV spectrum of the MTM-SVD analysis based on multivariate spatiotemporal noise realization with varying levels of autocorrelation ρ . [From Mann (1998).]

for spatially correlated coloured noise in the absence of signal. The fundamental advantage of the LFV spectrum as a means of signal detection in this regard, is the universality of its underlying distribution for a very general class of noise processes. Under the assumption that the noise components of the time series that comprise the multivariate dataset exhibit a smoothly varying coloured noise spectrum (e.g., as defined in section 2.1) the null distribution is in fact independent of frequency and indistinguishable from that of white noise series with the same underlying spatial correlation structure. This frequency-independence of the distribution results from the fact that the K eigenspectra estimated from a noise process will exhibit a Gaussian distribution at any frequency f as long as the noise spectrum appears flat over the narrow bandwidth $f \pm pf_R$ within which the eigendecomposition is actually performed. This local variance decomposition is resistant to influence from neighboring frequency bands owing to the spectral leakage resistance properties of MTM discussed in section 2.2.

We demonstrate this frequency-independence of the null distribution of the LFV spectrum using the specific example of spatially-correlated red noise, showing the virtual independence of the LFV spectrum of the level of temporal autocorrelation in the dataset. There is nothing preferential about the AR(1) coloured noise model, however, and in fact the LFV exhibits a universal null distribution for any smoothly varying coloured noise process with a given number of spatial degrees of freedom. These features allow us to invoke a quite weak null hypothesis in signal detection that accommodates not only spatially-correlated red noise, but in fact a wide class of spatially-correlated coloured noise processes (e.g., the noise model of *Wigley and Raper* [1990] discussed earlier). We exploit the frequency-independence of the null distribution by making use of a resampling technique for estimating this distribution and associated confidence intervals for significance. We employ a bootstrap method [*Efron*, 1990] in which the spatially-distributed dataset is resampled in such a way that the spatial patterns of the actual data are unaltered, but their temporal sequence is randomly permuted in time. This permutation whitens the dataset, destroying any temporal structure, but keeping all spatial structure intact so that the spatial degrees of freedom in the actual (e.g., monthly) data field are always faithfully represented. Because the distribution of the signal detection parameter – the LFV spectrum – is independent of frequency under the assumptions described above, the distribution of the white bootstrap resamples is representative of that for

any frequency. Within one bandwidth of zero frequency (the “secular band”) however, fewer spectral degrees of freedom are available because the Fourier transform becomes real-valued at $f = 0$. Within this secular band, the confidence levels must be estimated separately.

The null hypothesis described above can also be tested by an alternative “parametric” approach. If the number of spatial degrees of freedom M in the noise background can be reasonably estimated, an alternative parametric procedure for estimating the null distribution is provided by Monte Carlo simulation with M realizations of a Gaussian distributed process [see *Mann and Park, 1994*]. Generally, the non-parametric bootstrap procedure is preferable, avoiding *a priori* assumptions of the spatial correlation structure of the noise. The frequency-independence of the distribution provides improved statistics on the quantile distribution, allowing the averaging of results over many independent frequencies of the discrete Fourier transform. Typically, 1000 independent bootstrap realizations are performed, providing good enough statistics for reliable estimation of the 99% threshold for significance. When dealing with monthly or seasonal data in which there may be seasonal inhomogeneity in the variance as well as the mean [for example, different seasons may have different levels of temporal autocorrelation – see e.g. *Briffa and Jones, 1992*], it is often advisable to perform the bootstrap procedure separately for each month of the year, averaging the results for all months or the appropriate season analyzed [see *Mann and Park, 1996b*].

To test the proper distribution estimation of the bootstrap procedure, we generated replicates of the synthetic spatiotemporal red noise process described in section 2.1 with varying levels of temporal autocorrelation. The same white noise innovation was used in each case, so that the stochastic element is identical for each case. The time series for the reference center gridpoint are shown for increasing values of ρ (Figure 10, top). The case $\rho = 0$ corresponds to a pure white noise sequence. The lower-frequency variability becomes relatively enhanced as ρ increases, with the case $\rho = 0.9999 \approx 1$ nearly a non-stationary random walk (the reader is referred back to Figure 2).

We applied the MTM-SVD methodology with $K = 3$ and $NW = 2$ to estimate the LFV spectrum for each spatiotemporal noise realization, estimating significance levels from the bootstrap procedure described above. The estimated null distribution, the reader might note, will be independent of the value of ρ owing to the

ρ	50%	90%	95%	99%
0.0	50%	10%	5%	1%
0.9	50%	10%	5%	1%
0.99	50%	12%	6%	2%
0.9999	50%	15%	10%	5%

Table 2: Rates of Exceedence of a Given Confidence Level for Significance as a Function of the Noise Autocorrelation Level ρ . [From Mann (1998).]

whitening nature of the bootstrap. Of interest, then, is whether this independence holds up, at least under reasonable degrees of redness, for the observed distributions of LFV spectra for the red noise processes themselves. The LFV spectra for the different cases are shown in Figure 10, bottom. Since the case $\rho = 0$ corresponds to white noise, the null hypothesis of a smoothly varying “locally white” noise background should trivially be satisfied. Indeed, the observed LFV spectrum breaches the 99% confidence level at a 0% rate, the 95% level at a 4.1% rate, and the 90% level at an 11.7% rate. This distribution is consistent with the expected rates of chance coincidence for rejecting the null hypothesis (1%, 5%, and 10% respectively). Moreover, the distribution for moderate red noise (i.e., $\rho = 0.9$, redder in fact than observational climate data as discussed in section 2.1) is virtually indistinguishable on the scale of the plotted LFV spectrum from that of the pure white noise case (compare cases $\rho = 0$ and $\rho = 0.9$ in Figure 10). Even for the quite strongly red case $\rho = 0.99$, the observed spectrum is quite close to that for the white noise case. Only as the red noise spectrum nears singularity (i.e., $\rho = 0.9999 \approx 1$) does the distribution of the LFV spectrum noticeably depart from that of the pure white noise case. The most obvious discrepancies are observed at low frequencies where the parameter F defined in section 2.1 far exceeds unity. A more thorough experiment employing ensembles of 1000 random trials (Table 2) demonstrates that the correct rates of chance exceedence of given confidence levels are indeed obtained for all but the largest value of ρ . Thus, the null distribution of the LFV spectrum has been shown to conform to the pure white-noise distribution under precisely those conditions for which our *a priori* definition of a smoothly varying coloured noise spectrum is satisfied. While we have demonstrated the frequency-independence of the null distribution for the LFV spectrum and the validity of the significance estimation procedure for the case of a smoothly varying red noise spectrum, we assert without demonstration that the requirement is much more generally just that of

smoothly varying coloured noise background, for which the spectrum does not vary abruptly with frequency (ie, a “locally-white” noise background). This generality of the null hypothesis invoked in the signal detection procedure is a significant strength of the MTM-SVD methodology.

3.4 Application to Synthetic Dataset

We now apply the MTM-SVD methodology to the full synthetic (spatiotemporal signal + noise) dataset described in section 2.1 using $K = 3$ and $NW = 2$. Figure 11 (top) shows the LFV spectrum of the full 100 years of synthetic monthly data. Each of the *a priori* signals (secular trend corresponding to the zero frequency peak, interdecadal peak centered near $f = 0.065$ cycle/yr, and multiple peaks within the $f = 0.5$ to $f = 0.33$ cycle/yr band of the frequency-modulated interannual signal) are significant well above the 99.5% level. There are no spurious peaks at the 99% level, consistent with chance expectations. With $NW = 2$ and $N = 1200$ months of data, there are between 25 and 50 independent values of the LFV spectrum within the range $f = 0$ to $f = 0.5$ cycle/yr, so that roughly speaking, no spurious peaks are expected at the 99% level, and only 1 or 2 at the 95% level.

The multiple, closely spaced set of highly significant peaks in the $f=0.2$ to $f=0.33$ cycle/yr (3-5 year period) range that were detected in the LFV spectrum are suggestive of a more broadband signal. Thus, it is useful to use an evolutive version of the analysis to see if a more parsimonious description of the signal is evident. Figure 11 (bottom) shows the evolutive LFV spectrum based on a 40 year moving window. Note that in this case, only oscillatory signals with period shorter than 20 year timescale can be resolved from a secular variation, so that the interdecadal signal and secular trend appear as a single merged low frequency streak in the evolutive spectrum. In the resolvable interannual band, however, a single dominant band of significant variance emerges, drifting from a dominant frequency $f = 0.35$ cycle/year (≈ 3 year period) early, to $f = 0.5$ cycle/year (≈ 2 year period) near the end of the series. Amplitude modulation is also somewhat evident in the evolutive LFV spectrum itself, although a reliable estimate of the amplitude modulation is only possible through signal reconstruction. It is thus clear that the description of a single frequency-modulated interannual signal provides a more parsimonious description of the group of peaks in the interannual band found in the spectrum of the full 100 year series.

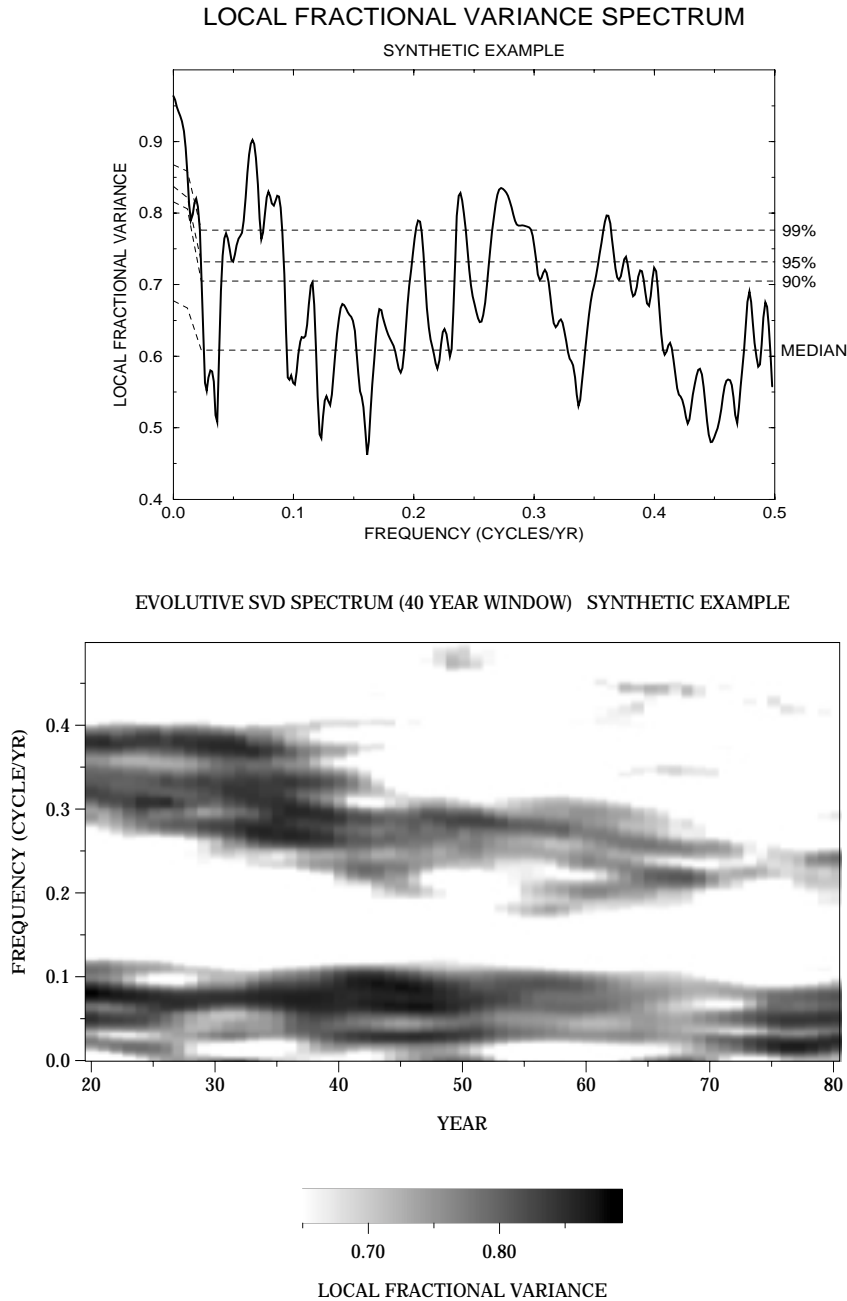


Figure 11: Local fractional variance spectrum of SVD based on (top) full 100 years of monthly data and (bottom) evolutive analysis with a 40 year moving window. In the former case, 90%, 95% and 99% confidence levels are shown with dashed line. For latter case, the LFV spectrum amplitude is indicated in grayscale, filtered at the 90% level for significance. Darker contrast indicates greater amplitude and significance [From Mann (1998).]

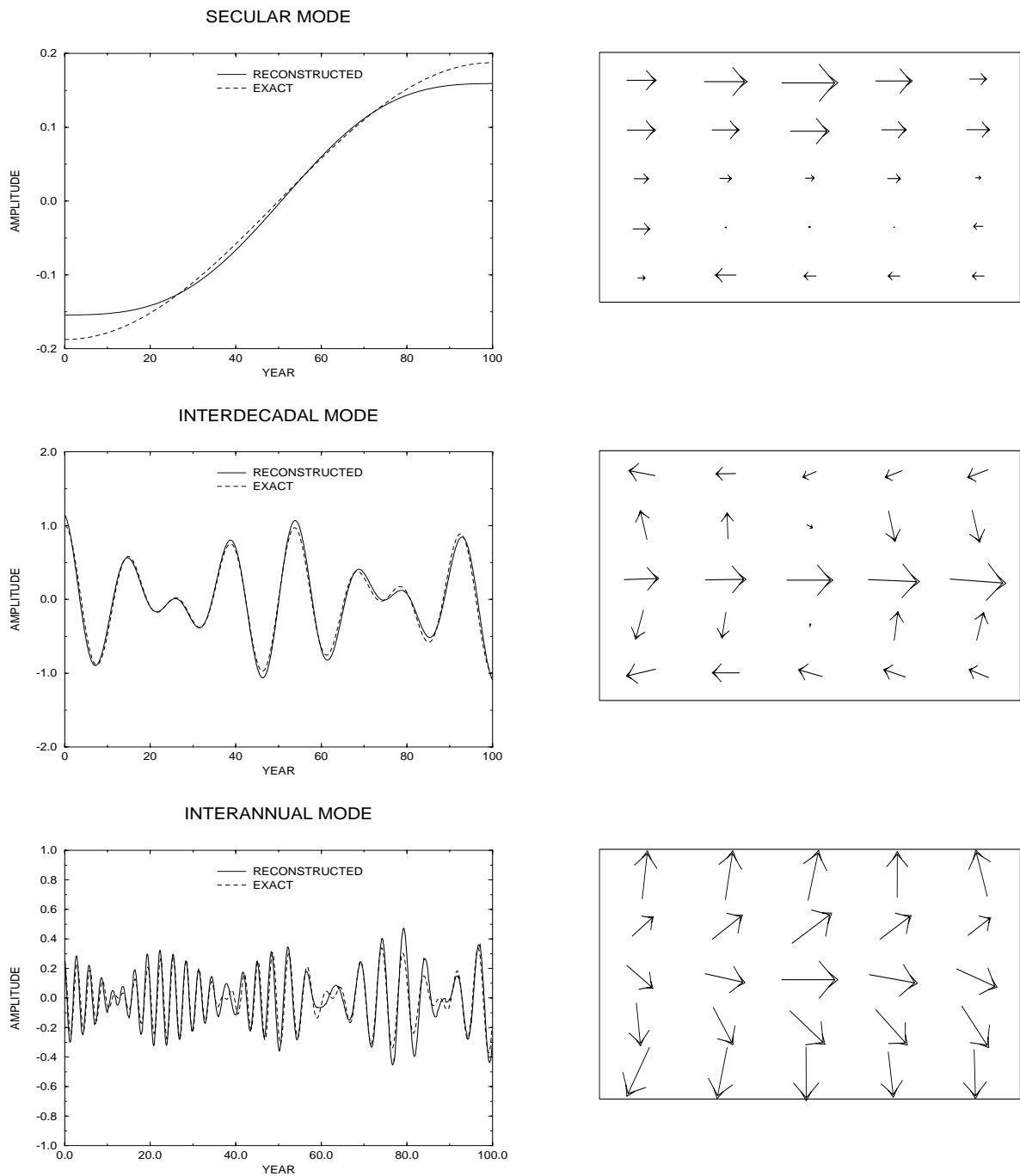


Figure 12: Temporal (left) and Spatial (right) patterns of reconstructed synthetic signals showing (a) secular mode, (b) interdecadal mode and (c) interannual mode. Actual reference time-domain signal as (see Figure 2) is shown by dashed curve for comparison to reconstructed reference time signal. [From Mann (1998).]

Each of the 3 signals are independently reconstructed (Figure 12). The secular and interdecadal oscillatory signals are reconstructed by the standard technique described in section 3.2, while the interannual signal is reconstructed based on the evolutive reconstruction method, employing a 40 year moving window. Both the spatial and temporal reconstructions are faithful to the exact counterparts (Figure 3), resolving much of the the complicated spatial variations in amplitude and phase of the true signals. Since the signals were immersed in spatially correlated red noise, some degree of noise contamination is unavoidable, and small spatially-correlated errors in both amplitude and phase are evident in the reconstructed spatial patterns. It is worthy of note that the spatial correlation structure of the noise itself can lead to spurious small-scale coherent departures from the true signal. Nonetheless, the phase and amplitude errors are modest, and it is clear that reconstructed signal amplitudes are very small in those regions where no original signal was present (compare e.g., the spatial patterns for the true and reconstructed interdecadal and secular signals at the nodes of the true signals). More simplistic means of signal projection (e.g., the common bandpassing of a multivariate dataset over a preferred range of frequencies) will lead to considerable spurious projection of the noise background. Such errors are largely avoided in the MTM-SVD signal reconstruction procedure, because only a particular modulated component of the narrowband variance is projected out in signal reconstruction. Consequently, regional errors in amplitude and phase are smaller.

These observations underscores a shortcoming of conventional PCA that is overcome in the MTM-SVD approach. As discussed previously in section 2.2, the spatial patterns of PCA eigenmodes are often arbitrary, and it is thus difficult to distinguish true global signals from combinations of regional signals artificially combined through the PCA procedure. Procedures such as varimax rotation [*Richman, 1986*] may yield more physically sensible patterns, but only under certain restrictive assumptions regarding the spatial structure of signals; in fact the true linear transformations of the eigenmodes required to yield physically distinct climate signals cannot *a priori* be known. In the case of MTM-SVD, a corresponding alternative linear transformation—the Fourier transform—is in fact specifiable *a priori*. The MTM-SVD procedure assumes that a signal has a very specific narrowband frequency-domain structure, and under that assumption assures quite high spatial signal-to-noise ratios in signal reconstruction. While there is considerable power in the synthetic data

(signal-plus-noise) at all gridpoints at all frequencies, the regional as well as large-scale spatial structure of the reconstructed signals were shown above to be quite faithful to their true counterparts. The ambiguities in distinguishing regional vs. global spatial structures, inherent in conventional PCA, is thus relatively alleviated in the MTM-SVD approach. Similarly, as discussed later, some of the deficiencies inherent in joint field decompositions are avoided when performed in the context of MTM-SVD. In the event where more than one signal is present *within* the narrow bandwidth of spectral estimation, however, similar problems and ambiguities to that encountered in traditional PCA can arise. Such an example is presented and discussed in section 4.1.

3.5 Effects of Sampling Inhomogeneities

Finally, we test the sensitivity of the MTM-SVD methodology to the sorts of potential sampling problems encountered in actual climate datasets. We examine the effects of temporal gaps in the sampling, as well as the effects of the sparse spatial subsampling of the global domain. We test the sensitivity to inhomogeneous time sampling by placing random gaps independently in each of the 25 gridpoints of the synthetic dataset, introducing a proportion of missing data that varies linearly from 50% at the beginning of the N=1200 months to 0% at the end. This trend in missing data simulates the gaps in instrumental climate data which are far more prevalent early in the instrumental climate record, and virtually absent in the most recent record. In the true climate record, this trend in sampling is somewhat more complex [for example, World War II induced a sudden decrease in spatial sampling of climate observations – see e.g., *Bottomley et al*, 1990]. The precise dates of the missing data are not correlated in space, again consistent with the typical missing data bias found in actual climate data. The gaps introduced as described above are somewhat more severe than those found in any of the gridded temperature dataset described earlier, ensuring a conservative test of the impact of missing data in actual climate records. The MTM-SVD analysis is repeated with this missing data, filling gaps with linear interpolation of neighboring values in time for each gridpoint (Figure 13). The missing data has little discernible effect on the analysis, owing largely to the fact that the serial correlation in time due to both signal and noise decreases the amount of independent information in any one sample. Given that the synthetic data has similar temporal correlation structure to the observational

climate data, we conclude that sizable rates of randomly missing data have little influence on the ability to discern significant frequency-domain information in the multivariate data. The impact of systematic biases in the collection of data, hidden in the processing stage of gridded monthly data typically used for climate studies, exhibits a greater potential to decrease the fidelity of these records, but considerable attempts have been made to document and ameliorate the impacts of such biases in gridded climate data [see the review by *Parker et al*, 1995]. *Jones and Briffa* [1992] favour the use of sea surface temperature (SST) rather than marine air temperature (MAT) measures of maritime temperature variations owing to historical changes in the diurnal timings of sampling in the latter case. SST measurements, on the other hand, suffers from systematic biases due to changes in bucket collection methods that can, if imperfectly, be estimated [*Bottomley et al*, 1990].

Finally, we examine the bias of inhomogeneities in the spatial sampling of climate data by employing sparse subsamples of the full spatial domain (see Figure 14) to the dataset described above. The application of the MTM-SVD methodology to these sparser spatial networks reveals a surprising insensitivity to the precise sub-sampling of the spatial domain, though the relative prominence and detectability of signals depends on whether or not regions where the signal is strongest are included in the spatial network (Figure 15). The “checkerboard” network grid of (I) containing 13 of the 25 gridpoints exhibits an LFV spectrum which is virtually indistinguishable from that of the full grid. So too does the more regionally restricted network of 10 gridpoints of (II), with no differences in peak detection at the 95% or greater levels of inference. The sparser regular network of 9 gridpoints of (III) begins to show signal detection degradation, with the interannual peaks detected at a lesser (95%–99%) degree of confidence than in the full dataset and cases I and II. Similar observations hold for the “northern hemisphere” only sparse network of 8 gridpoints in (IV). In this case, the sparseness of “tropical” sampling where the interdecadal signal is most prominent, leads to decreased detectability of the signal – it is just barely isolated at the 99% level for significance. Only with the very sparse network of 5 gridpoints (V) does the signal detection procedure suffer markedly. This network, for example, only samples the grid where the secular trend either vanishes or is relatively weak. Not surprisingly, the secular peak is not isolated as significant. Furthermore, the sampling network contains only a small number of spatial samples, and they are distributed over a small sub-region where the relatively larger coherence scale of the

signals relative to noise cannot be as readily exploited. Furthermore, with such few spatial degrees of freedom, the temporal gaps introduced in the individual synthetic series become more problematic, as there is little mutual information in space to help guide the spatiotemporal decomposition. In this case, distinctions between signal and noise at e.g., the 95% confidence level are less decisive. Notable spurious peaks (e.g., two between $f = 0.4$ and $f = 0.5$ cycles/year) breach the 95% level of significance. Comparing with LFV spectra of the denser grids (I-IV) allows us to visualize how increasing degrees of freedom in sampling allow for more clearcut signal/noise separation, damping out these noise fluctuations.

While a precise comparison of the spatial gaps in the synthetic data to those of the observational data is not possible because the relevant spatial scales and densities of sampling are not directly comparable, these results suggest that the samplings available in the instrumental record are probably adequate to analyze signals representative of global or hemispheric domains. The sparse networks of long-term proxy climate indicators available for analysis [Mann *et al.*, 1995b] are more likely to suffer some of the biases evident, for example, in the worst case scenario (V) discussed above.

4. Applications of MTM-SVD Approach to Observational and Model Climate Data

The search for oscillatory signals in the climate record exhibits a long and, sometimes *checkered*, history. Other than certain climate processes such as the 3-7 year El Nino/Southern oscillation (ENSO) for which the underlying dynamics are now relatively well understood [see e.g., Cane *et al.*, 1986; Philander, 1990] the detection of oscillatory signals in the climate record has remained controversial [see e.g., the review by Burroughs, 1992]. Increasingly widespread and higher-quality climate data and the development of more sophisticated statistical analysis techniques has led to more confident exploratory signal detection in climate studies. Several recent studies, for example, have provided evidence for decadal and longer timescale oscillatory climate signals in greater than century-long records of estimated global or hemisphere-mean surface temperature [e.g., Folland *et al.*, 1984; Kuo *et al.*, 1990; Ghil and Vautard, 1991; Allen and Smith, 1992; Mann and Park, 1993; Schlesinger and Ramankutty, 1994; Mann and Lees, 1996]. Without providing a spatial picture

of variability however, such studies shed little insight into the possible processes that may be responsible.

Simultaneous analysis of multiple indices of climatic variability, including vertically resolved oceanographic and atmospheric data [see e.g., *Wallace et al*, 1992; *Fraedrich et al*, 1993; *Xu*, 1993] have the potential to offer the most insight into underlying dynamical processes, but long duration (i.e., century-long) globally-distributed records are not available. Geopotential height data, for example, are available for only a few decades. Long records of sea level pressure are available but are largely confined to the northern hemisphere. Widespread records of precipitation exist, but they represent a more indirect proxy for underlying physical processes. Global temperature data provide widespread coverage for almost a century, and probably provide the greatest potential for the detection of interannual and decadal-scale spatiotemporal climate signals. Only proxy climate data, however, can provide a longer-term perspective on multidecadal and century-scale climate variability. Qualitative studies of longer-term proxy climate data [e.g., *Bradley and Jones*, 1993] have been undertaken, but systematic multivariate analyses of these data are at a preliminary stage [see *Bradley et al*, 1994; *Diaz and Pulwarty*, 1994; *Mann et al*, 1995].

It is thus worthwhile to analyze all of the complementary data available, both instrumental and proxy, to isolate persuasive evidence for signals in the climate record. Few early studies analyzed records of sufficient duration and global extent to characterize modes of climatic variability at decadal and longer timescales. Furthermore, most applications of conventional spatiotemporal signal detection approaches to climate data have suffered the limitations outlined in section 2.2. Seeking to obtain a clearer picture of possible low-frequency signals in the climate record, we review in this chapter the application of the MTM-SVD multivariate signal detection approach described in chapter 3 to various instrumental and proxy climate datasets.

We first describe an analysis of globally-distributed monthly land air and sea surface temperature data available during the past century [see *Mann and Park*, 1994]. The spatiotemporal nature of the analysis allows us to judge the relative importance of spatially uniform variations which may be associated with changes in the global surface heat budget, and more regionally heterogeneous patterns which may be indicative of the relocation of heat by anomalous patterns of atmospheric circulation. Aside from identifying well-established quasibiennial and interannual

ENSO signals in the data, this analysis provides evidence for less well-established decadal and multidecadal signals. These signals include a 15-18 year timescale oscillatory pattern exhibiting important tropical and extratropical features, and a secular “multidecadal” variation associated with a single cycle of warming and cooling global in extent, but most pronounced in the North Atlantic.

To obtain a more direct picture of the possible dynamical processes governing such signals, we analyze spatiotemporal variability jointly between surface temperature and sea level pressure (“SLP”) records that are available for nearly a century covering much of the northern hemisphere [see *Mann and Park*, 1996b]. This analysis yields independent evidence for the signals discussed above, and provides physical insight into possible underlying dynamical processes. The coupled oscillatory patterns of surface temperature and atmospheric circulation anomalies provide a more specific “fingerprint” of variability for comparison with signals found in climate model simulation studies. Seasonal and time-dependent features of the signals are more closely examined in this analysis. While sacrificing the global scope of the temperature-only analysis, the joint field analysis provides more dynamical insight, and nearly complete spatial sampling of the Northern Hemisphere region.

Next, to address the difficulty in isolating multidecadal and longer-term oscillations in the short instrumental record, we analyze a globally-distributed set of disparate proxy (“multiproxy”) temperature records of several centuries duration [*Mann et al*, 1995b]. This analysis provides evidence for persistent 15-30 year period interdecadal, and 50-100 year century-scale climatic oscillations. While the widespread sampling available in the instrumental record is not available in the proxy data sampling, the resolvable features of the spatial patterns appear to be consistent with their instrumental counterparts. Most importantly, information regarding the long-term amplitude and frequency modulation and the persistence of oscillations over time is available from this analysis.

Finally, we focus the MTM-SVD method on the frequency band centered on $f = 1\text{cyc}/\text{yr}$, i.e., the yearly cycle of temperature, to examine historical shifts in the timing of the seasonal cycle. To do this, we restore the yearly cycle of temperature at each gridpoint to the temperature anomaly data set described by *Briffa and Jones* [1992]. We verify that the seasonal shift reported by *Thomson* [1995] is present in this data set, and appears strongly concentrated in the continental interiors of the Northern-Hemisphere continents. We show that the observed spatial pattern of

seasonal shifts is in conflict with predictions of the effects of enhanced-greenhouse conditions in two well-known numerical climate models.

4.1 Global Temperature Data

Global surface temperature records provide a long and widespread sampling dating back to the 19th century. Such data sample most of the globe, albeit quite sparsely in certain regions. *Mann and Park* [1993] demonstrated that interannual and interdecadal temperature signals, while widely correlated, exhibit spatial variability that leads to considerable cancellation in a global average. Thus, analyses of hemisphere or global-mean surface temperature alone [e.g., *Folland et al.*, 1984; *Kuo et al.*, 1990; *Ghil and Vautard*, 1991; *Allen and Smith*, 1992; *Mann and Park*, 1993; *Schlesinger and Ramankutty*, 1994; *Mann and Lees*, 1996] can yield at best incomplete information regarding low-frequency climate signals. An analysis of the spatial patterns of signals is essential to capture more fully the complex regional variations in amplitude, sign, or phase of low-frequency global temperature signals. Here we seek to isolate the full spatiotemporal structure of oscillatory modes of variability in global temperature, including those whose effect is largely to redistribute heat over the Earth's surface. Such signals would scarcely be evident in large-scale temperature averages.

The temperature data used in this analysis (Figure 16) consist of land air and sea surface temperature anomalies distributed on a $5^\circ \times 5^\circ$ global grid [see *Jones and Briffa*, 1992]. To obtain nearly continuous monthly sampling from 1891 to 1990, we use a subset consisting of $M = 449$ grid points containing only small gaps (less than 6 months). We interpolated these gaps linearly, yielding time series of length $N = 1200$ months (i.e., 100 years). Such interpolation is defensible in light of the demonstrations regarding temporal inhomogeneity in section 3.5. While notable spatial gaps are evident over certain regions (e.g., the southern oceans, large portions of the North Atlantic and Pacific, Africa), the most seriously unsampled regions – the high latitudes – represent a small proportion of the global surface area. In light of the tests of spatial sampling sensitivity described in section 3.5, the available gridpoint data should be sufficient for establishing global-scale signals. Nonetheless, as described later, we provide an additional internal consistency check by comparing results from a relatively homogeneous, sparse spatial subsampling of the data with those of the full gridpoint dataset set (see also Figure 16).

An attempt has been made [Jones and Briffa, 1992] to remove the potential sources of systematic bias in this dataset arising from urban warming, historical changes in data collection, and the weighting of data within grid points. To the extent that some residual biases are inevitable, we refer the reader to discussions by those who have looked into these issues most carefully [Jones and Briffa, 1992; Parker et al, 1994; Bottomley et al, 1992]. Similar applications of the MTM-SVD methodology to spatially-interpolated instrumental climate datasets of greater than century duration [e.g., Kaplan et al, 1997] have recently been undertaken [Tourre et al, 1997].

Here we apply the standard MTM-SVD analysis procedure described in section 3 to the temperature dataset, with the conventional choices $K = 3$ spectral degrees of freedom and bandwidth parameter $p = 2$ that were advocated previously. The gridpoint anomaly series are standardized (ie, the long-term mean is removed and the residual is normalized by its standard deviation). The $M = 449$ gridpoints are uniformly weighted in the analysis. Temporal signal reconstruction is performed based on *a priori* specified boundary constraints of “minimum-slope” for secular variations and “minimum-norm” for oscillatory signals (see section 3.2). Justification of these choices is provided by Mann and Park [1994], although more objective boundary constraints (see section 3.2) are used in the subsequent analysis of joint SLP and temperature data (section 4.2).

LFV spectra

Figure 17 shows the LFV spectrum resulting from the MTM-SVD analysis of the 100 year dataset over the broad frequency range $f = 0$ to $f = 2.0$ cycle/year (i.e., periods from secular trend through half-year). Statistical significance levels shown were taken from the bootstrap resampling estimates of the null distribution. A separate parametric analysis [Mann and Park, 1994] suggests that this distribution is equivalent to that of Gaussian (locally) white noise with $\tilde{M} = 20$ spatial degrees of freedom. The most prominent peaks are the secular ($f \approx 0$) peak and those corresponding to the seasonal cycle and its first harmonic at $f = 1$ and $f = 2$ cycle/year. The latter peaks are somewhat unexpected in *deseasonalized* temperature anomaly data for which the seasonal cycle has nominally been removed [Jones and Briffa, 1992]. Due to the deseasonalization process, one statistical degree of freedom has been removed from any variability at the annual cycle or its harmonics. The de-

creased number of degrees of freedom raises the required levels of significance in the LFV spectrum from those shown, but does not alter the conclusion that the annual cycle and its first harmonic are significant in the anomaly data. This anomalous behavior in the annual cycle of global temperature anomaly data was first noted by *Kuo et al* [1990], and appears to be associated with low-frequency changes in the timing of the seasons [*Thomson, 1995; Mann and Park, 1996a*]. Otherwise, the LFV spectrum exhibits for the most part the frequency-independent spectrum expected for a coloured noise process (the reader is referred back to the discussion of section 3.3) but with a somewhat greater number of 99%-significant peaks (11 aside from the 3 discussed above) than would be expected (1-2 following the discussion in section 3.3) from chance coincidence alone. Of these, 8 are found in the interannual ($f < 0.5$ cycle/year) band, corresponding mostly to frequencies (e.g., the ≈ 2.1 quasibiennial period and the 3-7 year period ENSO band) associated with *a priori* established climate signals. Other apparent signals, however, are more disputable. Note that the background LFV spectrum (e.g., the depth of the noise floor) does not exhibit a corresponding increase in the interannual frequency range, underscoring the fact that the distribution of the LFV spectrum is similar at the low frequencies, as expected, but that there are simply a greater number of excursions at the highest percentiles. This observation is consistent with the detection of a small number of narrowband interannual signals superimposed on the noise background. We focus on these below.

Figure 18 shows the LFV spectrum in the interannual ($f > 0.5$ cycle/year – i.e., periods greater than 2 years) range. Results for the full 100 years of monthly data are shown along with those based on only the first and last 90 years of data. The latter calculations provide a test of the robustness of signals “found” in the LFV spectrum. Further truncation of the data series would decrease the spectral resolution of the LFV spectrum to the point where meaningful comparison is not possible. The irregular nature expected of the signals will lead to variations in the relative prominence of individual spectral peaks over different time intervals, but consistency among the three trials allows more confident signal detection inferences. The LFV spectrum indicates peaks centered at 2.2 years, several peaks within the 4-6 year band, a peak centered at 15-18 year period, and a secular peak where the significance breaches the 99% confidence level for nonrandomness in each of the three trials. Other significant peaks are not as robust. The peak near 3 year period

breaches the 99% confidence level in one of the three cases, and at least the 90% level in the other two. Peaks near 3.5 year period, 7-8 year period, and 10-12 year period pass or nearly reach the 95% confidence level in two of the three cases, and at least the 90% confidence level in the remaining case.

Trend detection can also be accommodated through analysis of the LFV spectrum, but some subtleties must be taken into account. As explained in section 3.1, multiple signals with period longer than N/p (where $p = 2$ is the bandwidth parameter used in all of our studies), corresponding to the secular band $f < pf_R = 0.02$ cycle/year in this study, cannot be distinguished in the LFV spectrum. However, at least $K-1=2$ distinct secular variations can still be separately identified by virtue of their orthogonal spatial patterns and temporal modulations if referenced to the secular band near $f = 0$. Both secular trends and ultra-low-frequency oscillatory signals in this case will be described as having a carrier frequency $f = 0$ and an envelope with $K - 1 = 2$ degrees of freedom (there is a loss of one-degree of freedom at $f = 0$ due to removal of the mean). The envelope can thus describe limited oscillatory, though strictly not periodic, behavior. An iterative procedure is used to identify possible significant *secondary* secular modes of variation, based on the fraction of residual secular variance explained once the principal mode is accounted for. This process leads to the detection of two distinct secular timescale signals at the 99% confidence level in the global temperature dataset. The primary mode accounts for 77% of the zero-frequency variance (i.e., an LFV of 0.77) while the secondary mode describes most of the remaining 23% zero-frequency variance. Because the resolution of the LFV is variable between f_R and pf_R and $K - 1$ distinct modes (i.e., trends or oscillatory variations) are resolvable at each distinct frequency value, these two modes need not combine to describe *all* of the variance in the nominal secular band ($f < 0.02$ cycle/year). Only for convenience are multiple secular variations referenced to the same frequency $f = 0$ for detection and reconstruction. A residual of secular band variance is left behind once these two secular variations are taken aside, describing the low-frequency noise background which is not discernible from coloured noise.

Distinct peaks in the LFV spectrum at 15-to-18 and 11-to-12 year and near 2.2 year period rise abruptly from the noise background, and are thus inferred as representing distinct “signals” in the data. In contrast, the group of peaks within the 3-7 year ENSO band are not well separated from the noise background or from

#	f (cycle/yr)	τ (years)	% LFV	T_{MAX}	T_{RMS}	T_{GLB}	P_{GLB}
SECULAR TREND	0–0.02	<i>trend</i>	0.77	1.7	0.55	0.51	0.94
MULTIDEC. VARIATION	0–0.02	>50	0.23	1.4	0.29	0.03	0.10
INTERDEC. OSC.	0.055–0.065	15–18	0.60	1.6	0.45	0.18	0.40
QUASIDEC. OSC	0.085–0.09	10–12	0.52	1.7	0.37	0.06	0.17
ENSO BAND	0.13–0.15	6.7–7.7	0.53	1.4	0.39	0.16	0.42
”	0.175–0.195	5.1–5.7	0.62	1.6	0.36	0.09	0.32
”	0.21–0.23	4.3–4.8	0.61	1.6	0.37	0.15	0.41
”	0.295–0.30	3.3–3.4	0.51	1.3	0.36	0.10	0.28
”	0.32–0.35	2.8–3.0	0.53	1.1	0.28	0.11	0.40
QUASIBI OSC	0.43–0.47	≈ 2.2	0.58	1.5	0.38	0.14	0.36

Table 3: Statistically Significant Spatio-Temporal Signals or Signal Components Isolated in the SVD Analysis, Enumerated in Order of Increasing Frequency, Along With Associated Range in Frequency and Period of the Signal/Component, Local Fractional Variance (LFV) Explained of the Associated Frequency Band, Maximum Regional Amplitude of Pattern, Root-Mean-Square Amplitude of Pattern, Amplitude of Global Mean of Pattern, and Projection of Pattern Onto Global-Mean Temperature. For the latter statistic, $P_{\text{GLB}} = 1$ e.g. describes spatially uniform warming or cooling, while $P_{\text{GLB}} = 0$ describes complete spatial cancellation of regional variations in a global mean. Amplitudes of variability (in Celsius) correspond to maximum peak-to-peak cycle amplitude over the 100 year period. [From Mann and Park (1994).]

each other, and may be associated with more complex frequency domain structure than can be identified based on spectral analysis of a fixed window of data. In this case, the enumeration of distinct “signals” within the broader 3-7 year band seems inappropriate. Additional insights are obtained from evolutive generalizations of the procedure described in sections 3.1 and 3.2, or further, from a wavelet-based multivariate decomposition [Park and Mann, 1997]. It is nonetheless useful to examine separately the high- and low-frequency ENSO peaks, which we loosely refer to as ENSO “components” here. Table 3 itemizes the 10 significant peaks isolated in the MTM-SVD analysis.

As a crosscheck, we performed a parallel analysis using a small subset of ($M = 50$) gridpoints scattered evenly over the globe to estimate the effect of sampling inhomogeneity on the analysis of the global temperature dataset. The resulting LFV spectrum (Figure 19) is not significantly dissimilar from that of the full ($M = 449$) dataset. The most notable differences are greater prominence of the 2-to-3-year timescale ENSO peaks, and a slight shift in the location of the quasidecadal peak

(centered closer to 10 year period in the sparse dataset). We conclude that the MTM-SVD analysis of the global temperature data is reasonably robust to sampling inhomogeneity and variations in spatial sampling density. The bias introduced by the paucity of information in data-poor regions is more difficult to determine. The exercises of section 3.5 suggest however that these biases probably are not too influential for the spatial sampling available.

Spatial and Temporal Correlations Across Time Scales

The similarity between the spatial patterns of distinct signals or frequency components of a band-limited signal can provide insights into possible physical relationships between them. The squared dot product of the spatial EOFs derived from the MTM-SVD analysis provide such a measure of similarity between spatial patterns. Under the assumption of Gaussian random spatial variations with \tilde{M} complex spatial degrees of freedom, the statistical significances of such correlations are provided from standard tables. Table 4 indicates statistical comparisons between the distinct signals or components identified. These quantitative comparisons of spatial relationships corroborate qualitative inspection of the temperature pattern reconstructions shown below. Patterns of temperature variability within the core 3-7 year ENSO band (i.e., those corresponding to peaks at 2.8-to-3.0-, 3.3-to-3.4, 4.3-to-4.8, and 5.1-5.7 year period) all share a characteristic global pattern [see e.g., *Halpert and Ropelewski*, 1992] of in-phase variability throughout much of the tropics and extratropical teleconnection patterns such as the PNA or TNH pattern over the Pacific/North American sector [see *Wallace and Gutzler*, 1981; *Barnston and Livezey*, 1987]. The corresponding spatial EOFs are correlated at greater than 99% confident level (sharing between 25% and 50% of their variance in common in each case). The 7-8 year peak has a less classical “ENSO” pattern, but does show some significant similarity with the other ENSO-band patterns, as well as with other patterns (e.g., the quasi-biennial pattern) exhibiting a temperature signature consistent with the North Atlantic Oscillation [NAO – see e.g., *Wallace and Gutzler*, 1981; *Rogers*, 1984; *Barnston and Livezey*, 1987; *Lamb and Pepler*, 1987]. This observation seems to be consistent with the study of [*Rogers*, 1984] who observed a peak near 7.3-year period in the spectrum of the NAO index. The spatial patterns associated with the interdecadal 15-to-18 and quasidecadal 10-12 year signal both share a combination of ENSO-like and NAO-like features with certain (i.e., 3.3-to-3.4- and 5.1-to-5.7-year)

ENSO components, exhibiting spatial correlations significant at $>99\%$ confidence. Spatial patterns associated with quasibiennial peaks centered near 2.1-to-2.3-, 7-to-8-, and 11-to-12-year period are each dominated by an NAO-like pattern. While some of these correlations may be spurious, there are only 45 distinct correlation pairs, and very few should randomly exceed the 99% confidence level given our estimate of $\tilde{M} \geq 20$ spatial degrees of freedom in the dataset.

In contrast, a similar dot-product of the spectral EOFs or “principal modulations” measures the similarity in the slow amplitude and phase modulation of distinct signals or components. Such similarity may be indicative of a non-linear coupling between oscillatory variations with different periodicities, or simply modulation by the same long-term envelope. In the case of a secular mode and an oscillatory signal, a significant correlation may indicate modulation of the oscillatory signal by the secular variation. Under the assumption of a smoothly varying coloured noise background, the correlations should exhibit the null distribution describing pairs of Gaussian distributed complex K -vectors. These latter dot-products suggests a number of interesting interrelationships. The 15-18 year period interdecadal ENSO-like signal exhibits similar long-term temporal modulation to several of the ENSO-band components, suggesting the possibility of a consistent long-term modulation of ENSO during the past century. The secondary “multidecadal” secular variation exhibits a high correlation with the envelope of the 10-12 year quasidecadal signal, suggesting the possibility that quasidecadal oscillations in the North Atlantic are modulated by the long-term multidecadal secular variation centered in that region. In turn, there is some evidence for a long-term modulation of the quasibiennial oscillation by the secular “trend”. Such possible relationships are discussed later on.

Secular Signals

The primary secular mode (Figure 20) describes an in-phase, global-scale secular trend in the temperature dataset. The associated spatial pattern of warming projects strongly (94% projection) onto global mean temperature.

The maximum regional warming trend (Table 3) is $\sim 1.7^\circ\text{C}$, while the estimated global-mean warming is closer to 0.5°C . Both this mean warming and the temporal reconstruction of the trend (inset, Figure 20) are consistent with recent non-parametric analyses of global-mean temperature [*Ghil and Vautard, 1991*], indicating warming most rapid from about 1920 to 1950. The continued acceleration

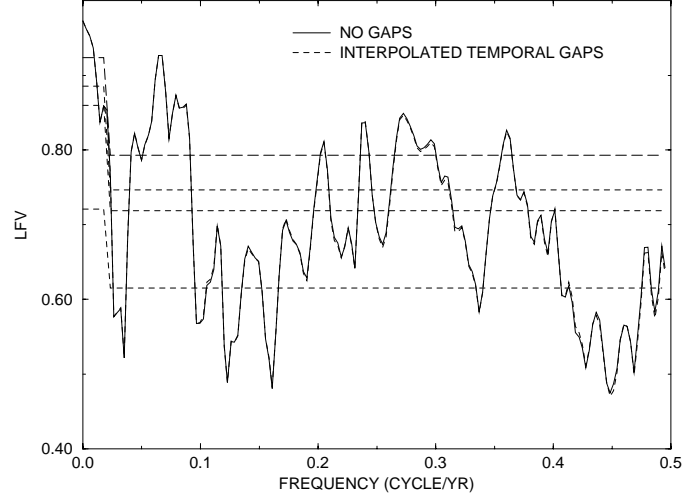


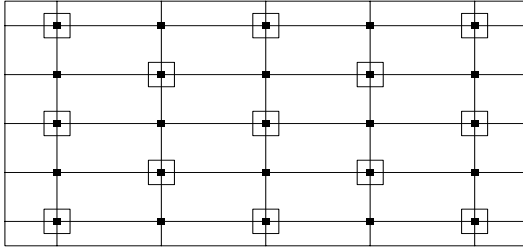
Figure 13: Comparison of LFV spectrum for complete data set and for the case where temporal gaps are present (see text) which are linearly interpolated. [From Mann (1998).]

τ , years	<i>trend</i>	> 50	15-18	10-12	7-8	5.1-5.7	4.3-4.8	3.3-3.4	2.8-3.0	≈ 2.2
<i>trend</i>	1	0	0.16	0.13	0.44	0.33	0.25	0.19	0.10	0.77 [†]
> 50	0	1	0.67	0.87 [†]	0.11	0.51	0.49	0.54	0.30	0.21
15 – 18	0.13 [*]	0.03	1	0.54	0.13	0.44	0.81 [†]	0.95 [‡]	0.52	0.15
10 – 12	0.00	0.06	0.37 [‡]	1	0.25	0.55	0.23	0.38	0.40	0.44
7 – 8	0.13 [*]	0.01	0.01	0.10	1	0.51	0.05	0.22	0.16	0.70 [*]
5.1 – 5.7	0.04	0.04	0.25 [‡]	0.22 [‡]	0.03	1	0.20	0.27	0.04	0.70 [*]
4.3 – 4.8	0.08	0.04	0.22 [‡]	0.01	0.04	0.33 [‡]	1	0.81 [†]	0.25	0.04
3.3 – 3.4	0.07	0.02	0.25 [‡]	0.16 [†]	0.09	0.34 [‡]	0.32 [‡]	1	0.56	0.09
2.8 – 3.0	0.13 [*]	0.01	0.11 [*]	0.02	0.13 [*]	0.25 [‡]	0.42 [‡]	0.25 [‡]	1	0.07
≈ 2.2	0.02	0.01	0.05	0.26 [‡]	0.17 [†]	0.06	0.11 [*]	0.19 [†]	0.08	1

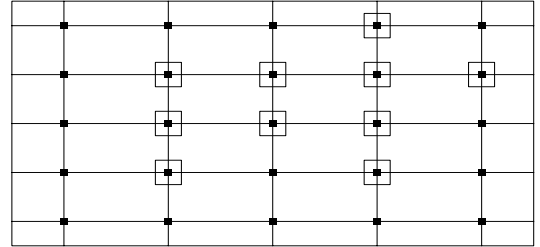
Table 4: Squared Correlations Between Spatial and Temporal Modulation Patterns of Distinct Signal/Component Pairs With Associated Significance Levels. The top triangle measures the similarity in the spectral EOFs or “principal modulations”, comparing the long-term envelopes of different oscillatory signals or components and indicating possible temporal relationships. The bottom triangle compares spectral EOFs of different signals or components, measuring the similarity in their spatial patterns. Under the assumption of locally-white noise, the significance levels for these correlations are estimated from the standard distribution of the spectral coherence based on $\tilde{M} = 20$ spatial and $K = 3$ spectral degrees of freedom respectively. From Mann and Park (1994).]

Symbols: * = > 90% † = > 95% ‡ = > 99%

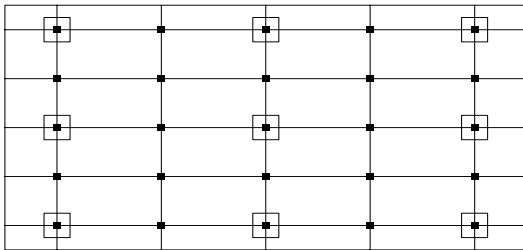
I



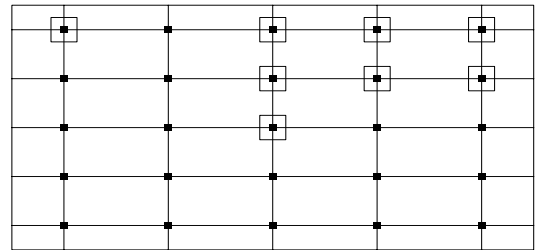
II



III



IV



V

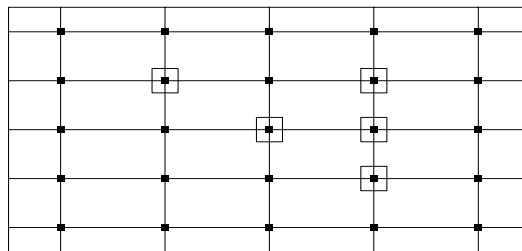


Figure 14: Various spatial subsets of the domain used for testing sensitivity to spatial sampling [From Mann (1998).]

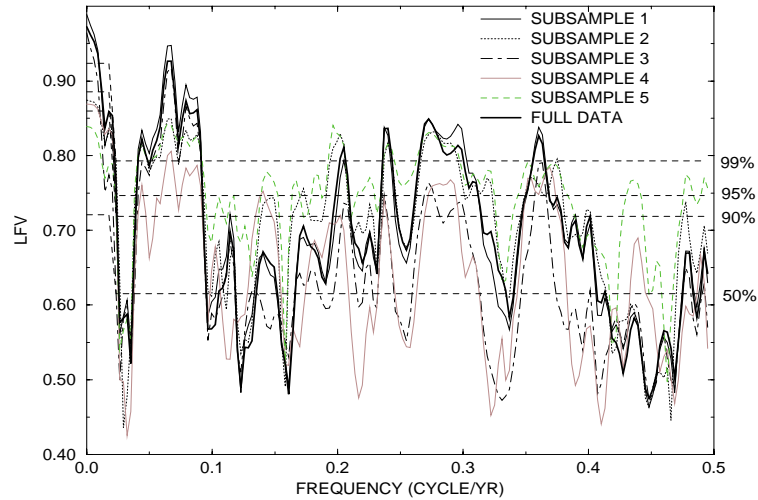


Figure 15: Comparison of LFV spectrum for complete spatial network along with the various spatially-subsampled networks described in Figure 14. The numerical vertical scale shown applies only to the full 25 gridpoint dataset. The LFV spectra for the various spatial subsets are renormalized so that the quantiles of the null distribution and significance levels shown roughly apply to each of the subsets, irrespective of the varying spatial degrees of freedom present.

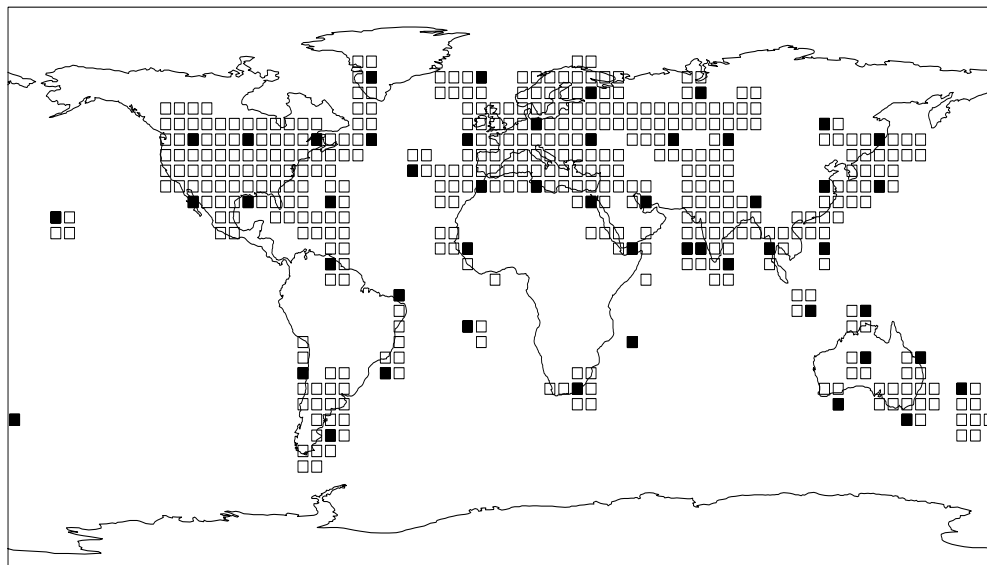


Figure 16: Locations of 5 degree by 5 degree grid points used in analysis. The filled boxes indicate the sparse more homogeneously distributed sub-network of 50 gridpoints used to test sensitivity to spatial sampling. [From Mann and Park (1994).]

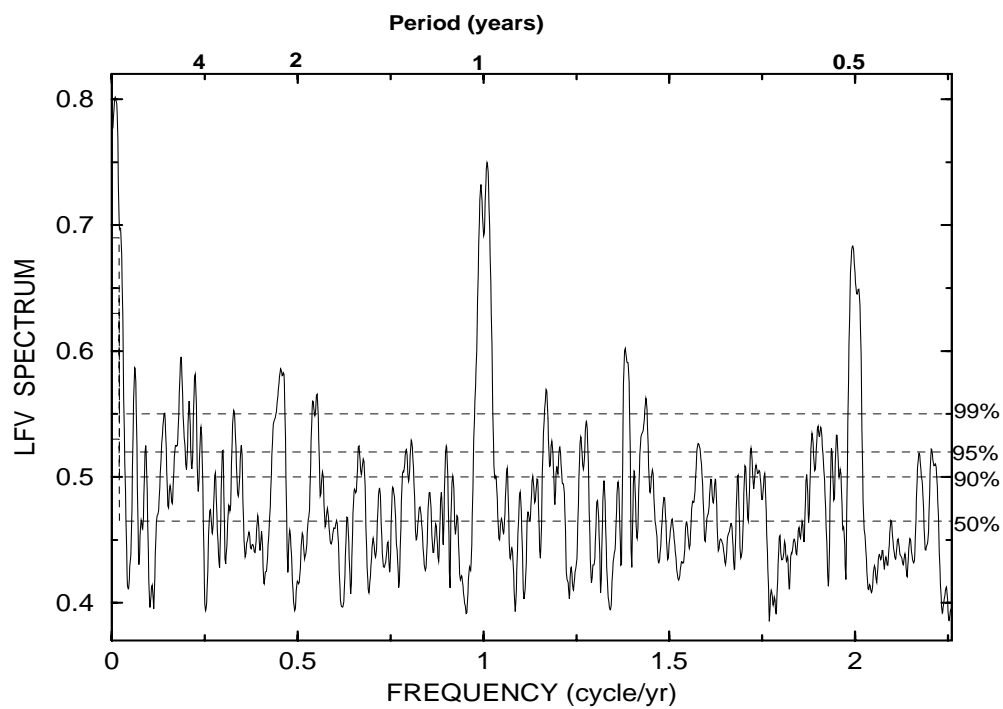


Figure 17: LFV spectrum of the global temperature data shown in Figure 16 through frequencies slightly greater than $f = 2$ cycle/yr. Horizontal dashed lines denote 90%, 95%, and 99% confidence limits from bootstrap resampling.

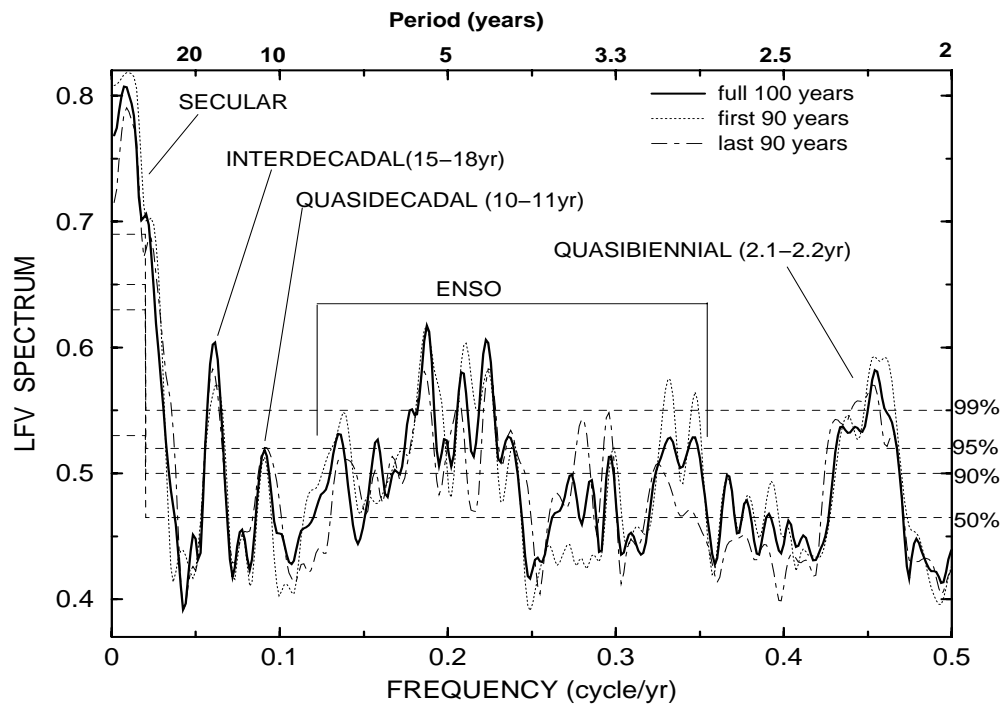


Figure 18: LFV spectrum of the global temperature data set in the restricted “interannual” range $f = 0$ to $f = 0.5$ cycle/year. The spectra for all 100 years (solid), first 90 years only (dotted), and last 90 years only (dot-dashed) are each shown for comparison. Horizontal dashed lines denote 90%, 95%, and 99% confidence limits from bootstrap resampling. Putative signals are noted by the indicated labels. [From Mann and Park (1994).]

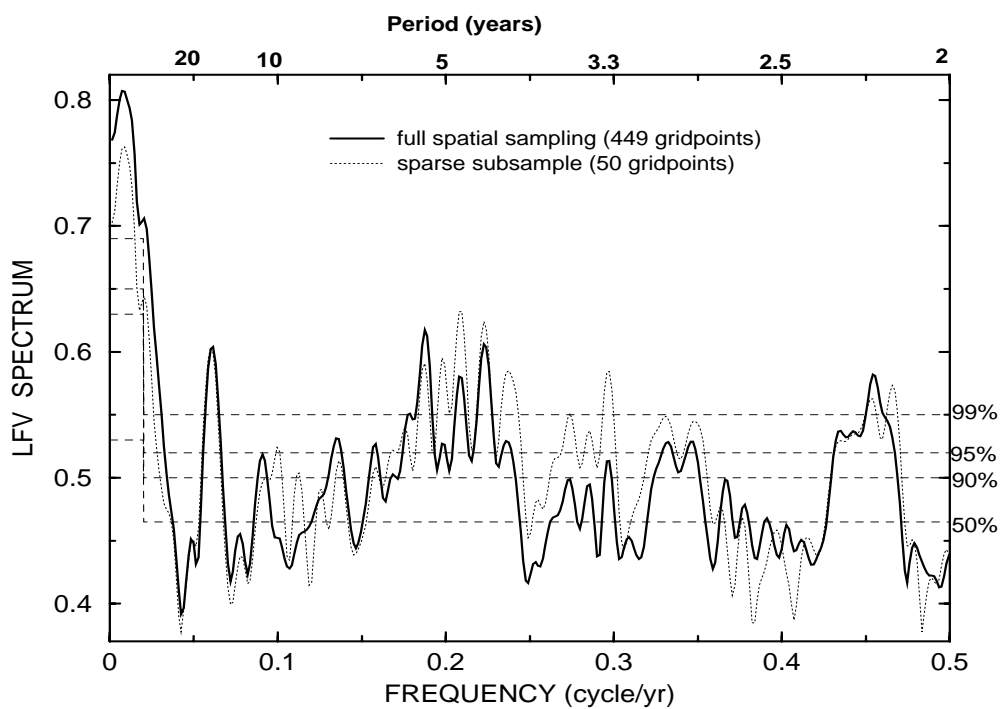


Figure 19: LFV spectrum of the full $M = 449$ global temperature data (solid) along with that of a sparse more homogeneously distributed $M' = 50$ gridpoint data set (dot-dashed). Horizontal dashed lines denote 90%, 95%, and 99% confidence limits from bootstrap resampling. [From Mann and Park (1994).]

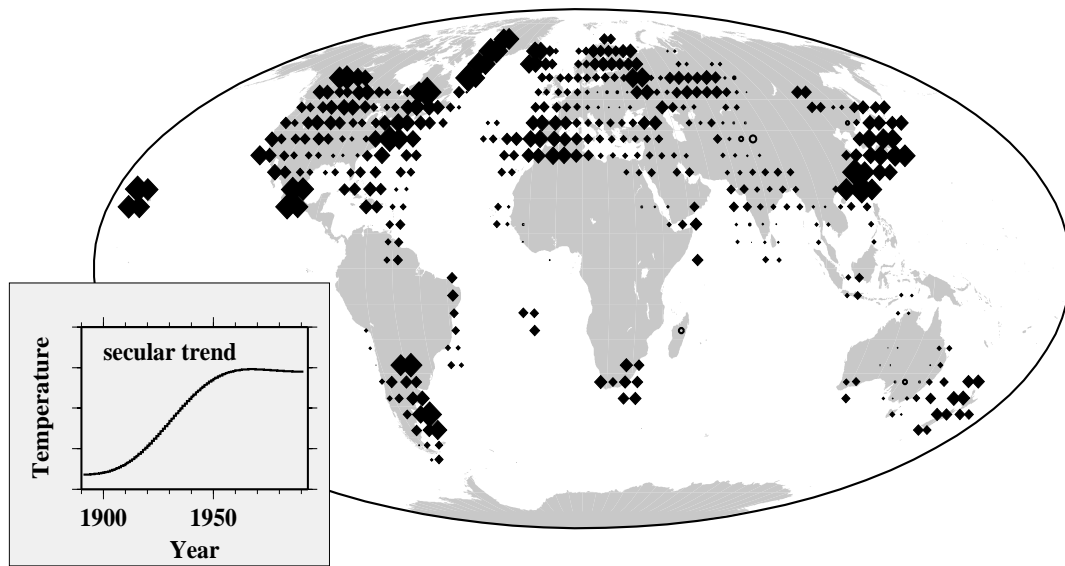


Figure 20: Pattern of temperature variability associated with the primary secular mode. Solid diamonds are used to indicate grid points evolving positively with the reference time domain signal shown in the inset (warming), while open circles represent the few grid points evolving negatively with the time domain signal shown (cooling). As in all subsequent plots, the symbol sizes scale the relative magnitude of temperature variations. The absolute scale for typical and maximum regional variations is provided by Table 3. [From Mann and Park (1994).]

of global warming in certain regions through the 1990s is not associated, in the context of our study, with long-term secular warming. Such warming could represent a sudden, non-stationary shift to sustained ENSO-like global climate patterns [see *Trenberth and Hoar, 1995*], but may also be consistent with the natural internal fluctuations of the tropical Pacific system [*Cane et al, 1997*]. This is highlighted by the fact that a marked positive recent departure from the low-frequency global warming trend is found in the far eastern tropical Pacific (within the reach of positive El Nino SST anomalies), but not in the more central subtropical Pacific (see section 4.2, Figure 30). Much of the warmth of the 1980s (but *not* the 1990s) is, in contrast, explained by interdecadal fluctuations (see below).

Though associated with a clear global warming signal, the spatial pattern is variable, with certain grid points actually cooling slightly. Such regional departures from the average warming of $\sim 0.5^\circ\text{C}$ suggest the probable existence of associated atmospheric circulation anomalies accompanying the warming signal. Such circulation anomalies are addressed more directly in the joint temperature/SLP analysis of section 4.2. The strongest warming ($\sim 1.7^\circ\text{C}$) is observed along the margin of Greenland, which could indicate the influence of a positive ice-albedo feedback. Further such evidence is provided by the changes in seasonality of temperature described by *Mann and Park [1996a]*. For comparison, a calculation of the simple linear trend in the gridpoint data yields a similar pattern, albeit with a moderately higher estimated warming signal (compare the resulting values $T_{\text{MAX}} = 1.87^\circ$, mean region warming $T_{\text{RMS}} = 0.59^\circ$, and average global warming $T_{\text{GLB}} = 0.57^\circ$ with their corresponding values in Table 3), owing largely to the statistical leverage of recent decadal-scale warming in a non-robust least-squares trend estimation.

In contrast to the primary mode, the significant secondary secular mode describes a spatially heterogeneous multidecadal “cycle” centered largely in the North Atlantic (Figure 21) which projects little (10%) onto global mean temperature. To some extent the dissimilarity in the features of the two secular modes is guaranteed by their mutual orthogonality, much as are the modes of a classical time-domain PCA. The principal mode tends to capture the in-phase global component, while the secondary mode favours the dominant mode of variation in the the spatially heterogeneous residual (see e.g., the synthetic PCA experiment of section 2.2). Some linear combination of the two modes (i.e., rotation) or other statistical decompositions could possibly provide a more physical decomposition. *Schlesinger and Ramankutty*

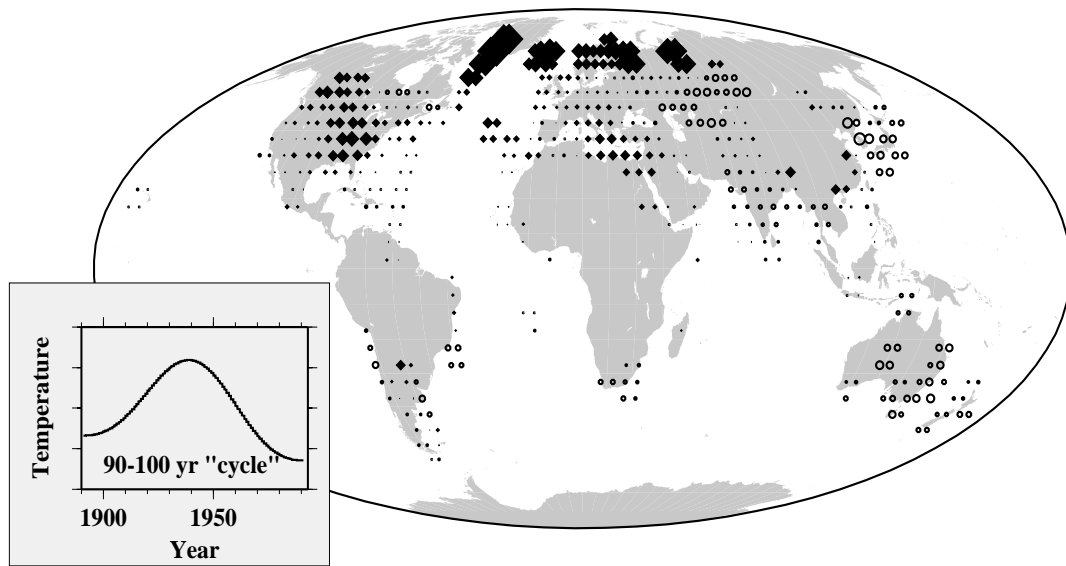


Figure 21: Pattern of temperature variability associated with the secondary secular mode of variation. High-amplitude variability is confined largely to the North Atlantic. Each grid point evolves with the same 70 – 80 year “oscillation,” shown in the inset, differing only in magnitude or sign. Solid diamonds evolve in phase with the North Atlantic, while grid points with open circles vary oppositely. A minimum slope constraint was invoked for the temporal signal reconstruction. [From Mann and Park (1994).]

[1994] for example identified a residual multidecadal oscillatory component in the global temperature record after removing a model predicted trend due to anthropogenic forcing. Only analyses of longer datasets (e.g., proxy data – see section 4.3) can more objectively separate out possible anthropogenic trends and low-frequency oscillatory features of the climate.

The cycle-like characteristic of the secondary secular variation is poorly constrained by the short duration of the data set, and the simple boundary constraints invoked. However a more objective signal reconstruction approach based on the optimal weighting of various boundary constraints (see section 4.2) favours a single ~ 70 year multidecadal cycle of variation, and long-term proxy data (section 4.3) offer additional evidence for a multidecadal or “century-scale” oscillatory mode with a 50-70 year timescale. The pattern of this multidecadal variation (Figure 21) exhibits significant amplitude in the high-latitude North Atlantic (as large as 1.4°C , see Table 3), in-phase with smaller amplitude variability in the United States, Northern Europe, and the Mediterranean region, and out of phase with variability elsewhere over the globe. The cycle of warming in the North Atlantic from roughly 1890-1940, and subsequent cooling, is consistent with the long-term trend in North Atlantic sea surface temperature and air temperatures determined elsewhere [*Deser and Blackmon*, 1991; *Kushnir*, 1994; *Schlesinger and Ramankutty*, 1994]. Large temperature variations in the high-latitude North Atlantic supports a possible connection with century-scale variability in deep water production [e.g., *Stocker et al*, 1992]. The opposite sign of anomalies in the North and South Atlantic, consistent with the inter-hemispheric contrast pattern noted by *Folland et al* [1984] is consistent with changes in cross-equatorial heat-flux that would be expected to arise from variability in the thermohaline circulation. The near cancellation of the pattern in a global average suggests a process that largely redistributes heat over the Earth’s surface. Additional dynamical insight is offered by the analysis of associated atmospheric circulation variations in section 4.2, while better statistical constraint on the apparent multidecadal oscillation is provided by the multiproxy data analysis of section 4.3.

Interdecadal Signal

The interdecadal 15–18 year period signal shown in Figure 22 has a pattern consistent with that of the pair-coherence map of *Mann and Park* [1993] and probably

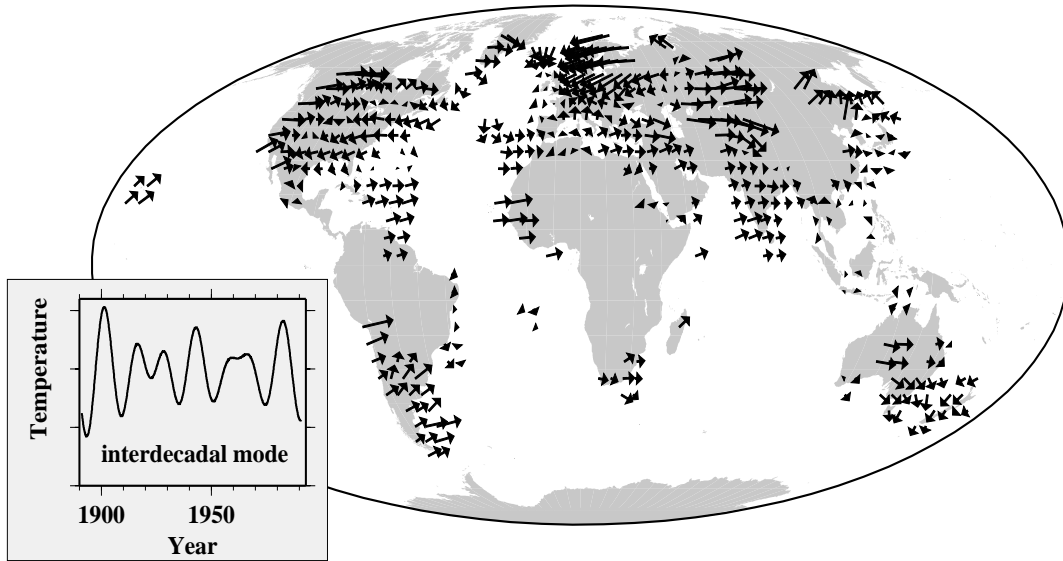


Figure 22: Pattern associated with the 15-to-18-year interdecadal mode, with zero phase (e.g., tropics) evolving with the time domain signal shown in the inset. Maximum pattern average warmth is coincident with tropical warmth. The size of the vectors indicates relative magnitude of temperature variations (absolute scale is provided in Table 4). Vector orientation indicates the relative temporal lag at each grid point. We define a zero phase vector (i.e., grid points with a vector pointing rightward, toward “3 o’clock,” for example, much of the tropics in this case) as evolving positively with the time domain signal shown in the inset. Counterclockwise rotation in the spatial pattern indicates positive lag, while clockwise rotation represents negative relative lag or “lead”. A rotation of 360 degrees corresponds to the periodicity of the mode (~ 17 years in this case). All grid points share the same long-term modulation, with the ~ 17 year carrier oscillation shifts forward or backward with the phase lags indicated in the spatial pattern. For example, grid points with vectors at “12 o’clock” experience maximum warming at a $90^\circ \sim 4$ -year lag relative to peak tropical warming. Grid points at “6 o’clock” experience maximum warming at ~ 4 years before peak tropical warming, and grid points at “9 o’clock” experience maximum cooling simultaneous with peak tropical warming. The pattern average variability is nearly in phase with the tropical variability, so that peak projection onto global warmth corresponds to peak tropical warmth. [From Mann and Park (1994).]

corresponds to the bidecadal temperature signal identified by *Ghil and Vautard* [1991] in global-average temperature. The spatial pattern resembles, at least superficially, that of ENSO, with high-amplitude, largely in-phase tropical warming or cooling, and similar inferred extratropical teleconnection patterns. Despite significant cancellation in the global average, this mode is associated with a sizable peak-to-peak $T_{\text{GLB}} \sim 0.2^\circ\text{C}$, with a maximum global warm anomaly coincident with tropical warming. The time domain signal (inset of Figure 22) suggests that the anomalous warmth of the 1980s was associated, at least in part, with a large positive excursion of the interdecadal oscillation. Note, however, that global warming in the interdecadal oscillation is associated with simultaneous cooling in the southeastern United States and Europe.

In addition to exhibiting spatial correlations at >99% confidence with three of the four ENSO spatial patterns (Table 4), the interdecadal mode appears to be associated with a modulation common to two of the ENSO-band components. The signal thus appears to exhibit at least a limited connection with long-term variations in ENSO, as has been suggested in previous studies of interdecadal climate variability [*Trenberth*, 1990; *Tanimoto et al.*, 1993]. This signal has been independently observed in studies of the South Atlantic [*Venegas et al.*, 1996], and may also related to significant regional climate impacts such as influences on Sahel rainfall [*Folland et al.*, 1986] and the dynamic topography of the oceans [*Unal and Ghil*, 1995].

A variety of mechanisms have been offered to explain such interdecadal $\sim 15-30$ oscillatory behavior of the climate, including external astronomical forcing [e.g., *Royer*, 1993], high-latitude ocean-atmosphere interactions [e.g., *Darby and Mysak*, 1993; *Mysak and Power* 1992], non-linear instabilities in the global thermohaline circulation [e.g. *Chen and Ghil*, 1995] and extratropical ocean-atmosphere feedback mechanisms [e.g., *Trenberth and Hurrell*, 1994; *Latif and Barnett*, 1994 – henceforth LB94; *Von Storch*, 1994], intrinsic tropical mechanisms [*Graham*, 1994] and coupled tropical/extratropical ocean-atmosphere mechanisms [*Gu and Philander*, 1997] in the Pacific ocean. Possible mechanistic explanations of the observed variability are further explored in section 4.2.

Quasidecadal Signal

A “quasidecadal” signal with 10-to-12-year periodicity (Figure 23) exhibits a temperature pattern with large regional amplitude in the North Atlantic, exhibiting a

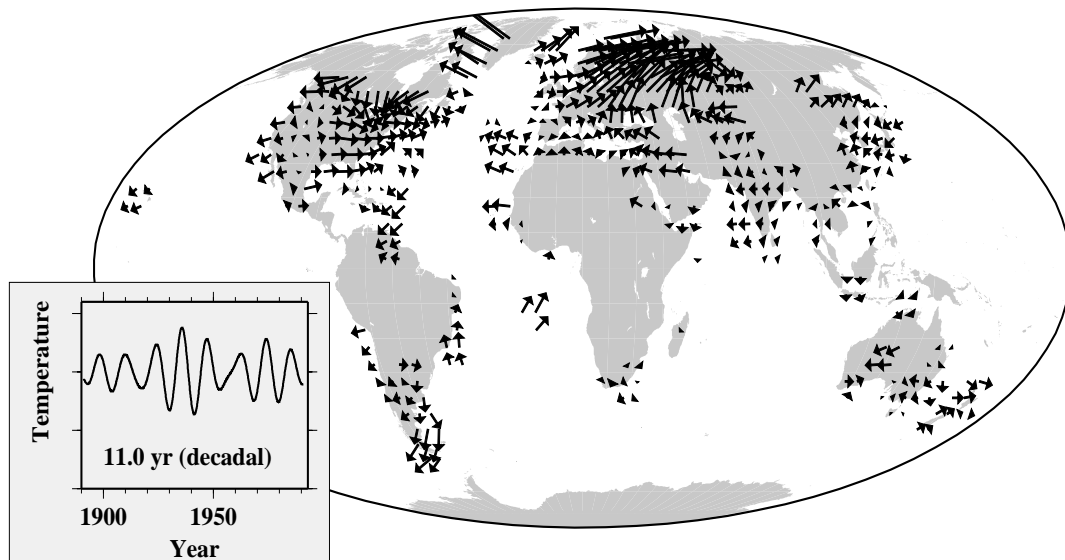


Figure 23: Spatial pattern of variability associated with the 10-to-12-year decadal mode, with the zero phase signal (i.e., arrow pointing directly right – e.g., Great Britain, most of southeastern United States) corresponding to the time series shown in the inset. Symbol conventions are similar to Figure 22. [From Mann and Park (1994).]

quadrupole phase pattern of warming and cooling in different regions bordering the Atlantic basin. This pattern is reminiscent of an NAO influence. Such a quasidecadal signal has independently been observed in other studies North Atlantic climate data [Deser and Blackmon, 1993; Hurrell, 1995]. The surface temperature pattern tends to cancel, however, in a large-scale average, exhibiting a relatively weak projection (18 %) onto global-mean temperature. It is thus not surprising that such a signal is either undetected [Folland *et al.*, 1984; Ghil and Vautard, 1991] or weakly detected [Allen and Smith, 1994; Mann and Lees, 1996] in studies of global-mean temperature, but emerges more distinctly in regional studies of continental United States temperature [Mann *et al.*, 1995a; Dettinger *et al.*, 1996], SLP [Mann *et al.*, 1995a], precipitation [Currie and O'Brien, 1992] Indian precipitation [Vines, 1986; Mitra *et al.*, 1991], and both tropical [Houghton and Tourre, 1992; Mehta and Delworth, 1995; Chang *et al.*, 1997] and North Atlantic [Deser and Blackmon, 1993] regional climate data. There is some debate in the literature over whether this decadal signal is or is not characterized by a cross-equatorial dipole in Atlantic sea surface temperatures [Houghton and Tourre, 1992; Mann and Park, 1994; Mehta and Delworth, 1995; Chang *et al.*, 1997; Tourre *et al.*, 1997]. Where there is spatial sampling in the Atlantic, our pattern exhibits fairly clear evidence for a nearly 180 degree reversal in phase of surface temperature variations north and south of the equator, supporting Chang *et al.* [1997] and Tourre *et al.* [1997]. The significant relationship (95% significance level-see Table 4) between the long-term modulation of this quasidecadal oscillation and the multidecadal secular variation in the North Atlantic described above, suggests that the longer multidecadal cycle of warming and cooling in the North Atlantic may modulate the amplitude of these higher frequency quasidecadal oscillations. In contrast, the signal is not significantly correlated (<50% confidence level) with the ~ 11 -year sunspot cycle, casting doubt on a simple linear relationship between decadal-scale solar forcing and similar timescale surface climate variations [e.g., Currie and O'Brien, 1992]. Joint analysis of historical sea-level pressure and surface temperature, discussed in section 4.2, suggests possible mechanisms for the quasidecadal oscillation.

ENSO Signal

The MTM-SVD analysis of the global temperature data reveals clear ENSO-band signals (Figure 24), and confirms a rough division of the ENSO-related variability

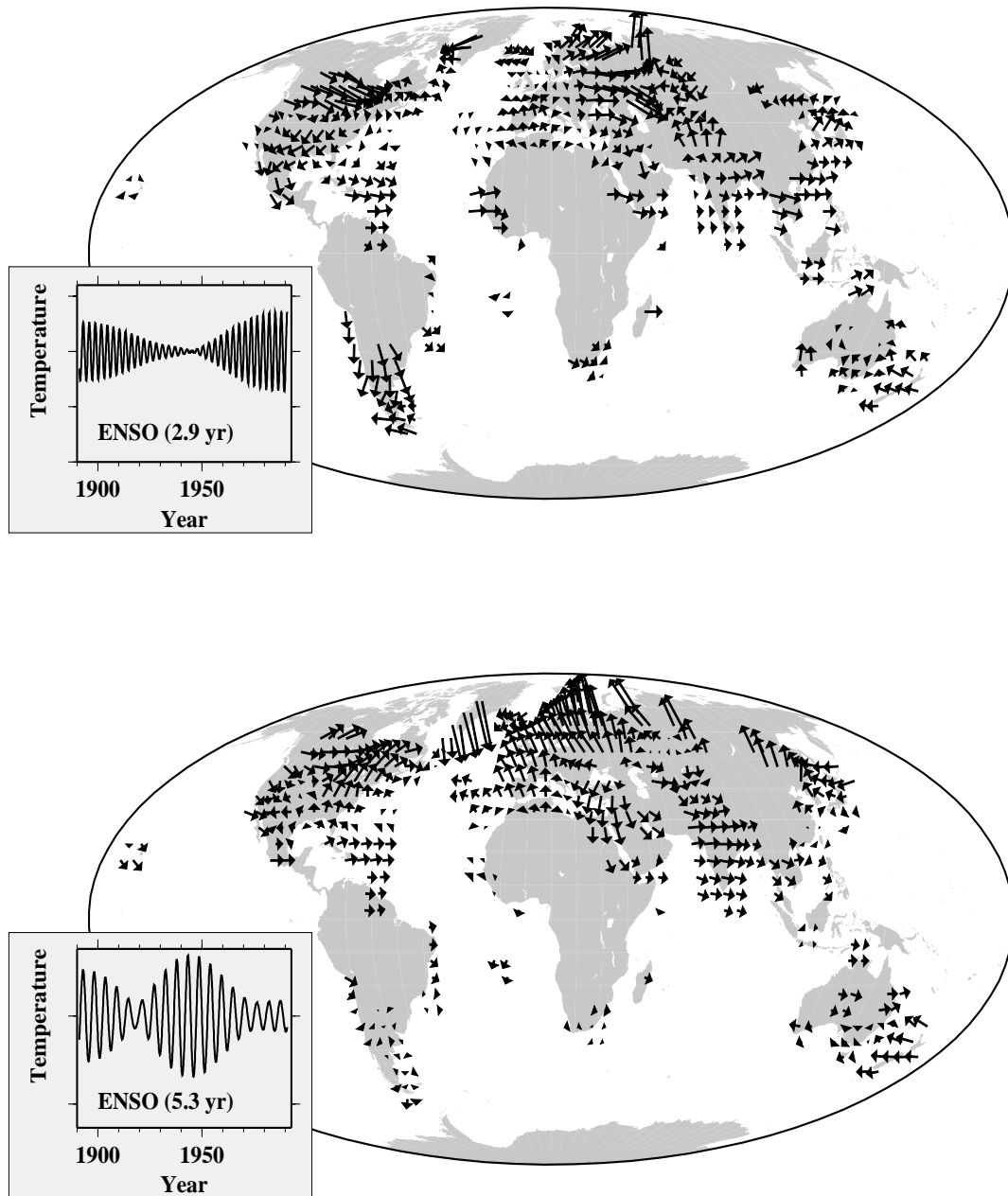


Figure 24: Spatial pattern associated with the 2.8-to-3.0-year (top) and 5.7-to-5.7 year (bottom) “ENSO” components. Symbol conventions are similar to Figure 22, with zero phase (e.g., much of the tropics) coincident with the time domain signal shown in the inset for both cases. [From Mann and Park (1994).]

into higher-frequency (2.8-to-3.0- and 3.3-to-3.4-year period) and lower-frequency (4.3-to-4.8- and 5.1-to-5.7-year period) bands, consistent with the notion of distinct high- and low-frequency bands of ENSO [e.g., *Keppenne and Ghil, 1992; Dickey et al, 1992*]. A more elaborate time-dependent description of the frequency-domain characteristics of ENSO is provided in the analysis of section 4.2. The spatial patterns (Figure 24) associated with the ENSO spectral peaks are similar to the ENSO temperature pattern identified by *Halpert and Ropelewski [1992]*, henceforth HR92. For example, both HR92 and our 2.8–3.0 year ENSO component show a pattern of roughly in-phase tropical warming coincident with warming and cooling, respectively, in the northwest and southeast United States. Such behavior is consistent with the positive phase of a PNA or TNH circulation anomaly pattern that has been argued to be favoured during tropical warm events [*Horel and Wallace, 1981; Livezey and Mo, 1987*]. Both patterns also share warming in eastern Europe coincident with cooling in central Asia and slight cooling in western Europe, as well as cooling in the northern Pacific that is in phase with warming in the tropical western Pacific. This latter pattern resembles a similar Western Pacific Oscillation or “WPO” pattern. Though much of warming during ENSO is produced by tropical ocean-atmosphere heat exchange, some of this heat is transported poleward by a variety of processes. Hence there is a tendency for warming, for example, in middle as well as tropical latitudes during or shortly following warm events, even though anomalous advection can produce cooling in certain regions. Such dynamics are responsible for the non-trivial impact of ENSO events on global mean temperature. Each of the ENSO patterns have significant projections onto global temperature (Table 3), with global-average peak-to-peak fluctuations $T_{\text{GLB}} \sim 0.10^{\circ}\text{C}$ for each component, and somewhat larger excursions for the sum over all components. Other workers [*Jones, 1989; Angell, 1990*] have noted similar interannual variations in global average temperature associated with ENSO.

Each of the ENSO component patterns share features of in-phase tropical warming with extratropical patterns consistent with combinations of the WPO, PNA, and TNH patterns. The lowest frequency (5.1-to-5.7 years ENSO) component exhibits the most prominent NAO signature, consistent with *Rogers [1984]* who identified a peak near 6-year period in the cospectrum of the Southern Oscillation and NAO. While the pattern for each component is by definition linearly reversed for negative and positive excursions, the sum of the components which interfere constructively

or destructively to describe the actual “warm” and “cold” events [see e.g., the total signal reconstructions shown later] need not exhibit an equivalence between large negative and positive reconstructed events. In each of our ENSO patterns, maximum global warm anomalies coincide with tropical warm events, while the maximum cold anomalies coincide with cold events.

Quasibiennial Signal

A quasi-biennial (~ 2.2 -year period) signal is isolated in the global temperature data (Figure 25) consistent with the independent detection of such a signal in Northern hemisphere SLP [*Trenberth and Shin, 1984*], North Atlantic SLP, winds, sea level pressures [*Deser and Blackmon, 1991*] and air temperatures [*Gordon et al., 1992*], and predominantly north-south variations in U.S. temperature [*Dettinger et al., 1996*]. The signal exhibits a prominent NAO temperature pattern as well as other extratropical regional anomalies, and is associated with sizable regional variations (0.38°C mean regional amplitude variations), as well as a significant peak-to-peak global average variation (0.14°C). As discussed by [*Trenberth and Shin, 1984*] and below in section 4.2, the surface quasibiennial signal shows no obvious relationship with the stratospheric quasibiennial oscillation (QBO) of similar timescale, although such connections have been suggested with atmospheric data higher in the troposphere [*Labitzke and van Loon, 1988*] or indirectly, through modulation of ENSO [*Barnston et al., 1991*]. Interestingly, there is evidence of modulation by the same envelope which modulates the lower-frequency ENSO variability (precisely those ENSO-band components, the 5.1–5.7 years and 7–8 years components which exhibit a notable NAO pattern – Table 4). These correlations are only marginally ($\sim 90\%$) significant, however, and may well be spurious.

Single-Gridpoint Reconstructions

Figure 26 shows the time-domain signal reconstructions for several chosen gridpoints, based on the sum over each of the spatiotemporal signals or signal components isolated in the MTM-SVD analysis. Also shown are the interannual lowpassed (periods longer than 2 years retained) raw data for comparison. The North American east coast gridpoint (Figure 26-top) is dominated by the secular warming trend (18% of the lowpassed “interannual” data variance) and interannual (ENSO and quasi-biennial) fluctuations ($\approx 13\%$ of the interannual variance), while the quasidecadal

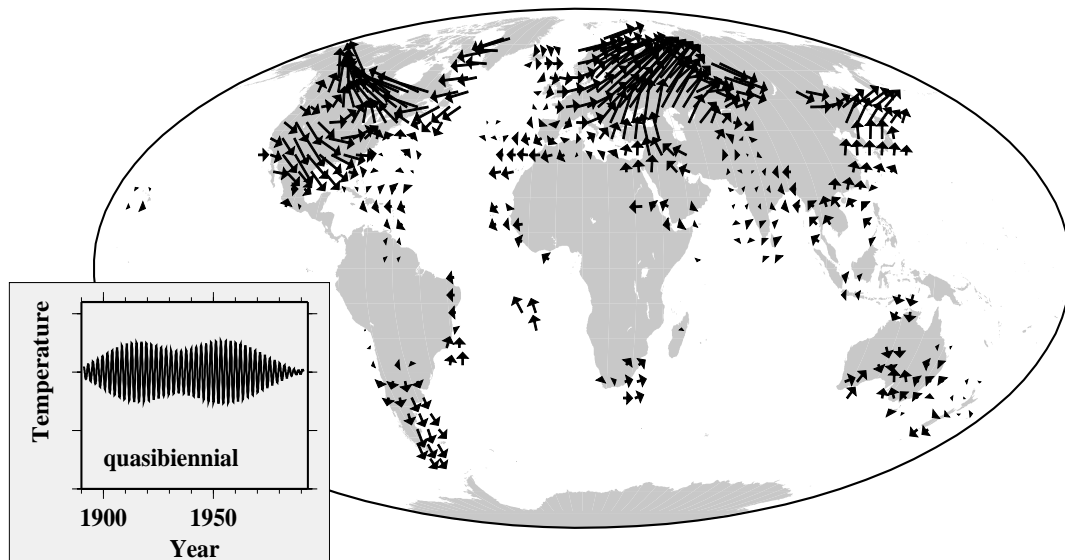


Figure 25: Pattern of variability associated with the 2.1-to-2.3-year quasi-biennial mode. Zero phase variability (e.g., England) evolves positively with the time series shown in the inset. Symbol conventions are similar to Figure 22. [From Mann and Park (1994).]

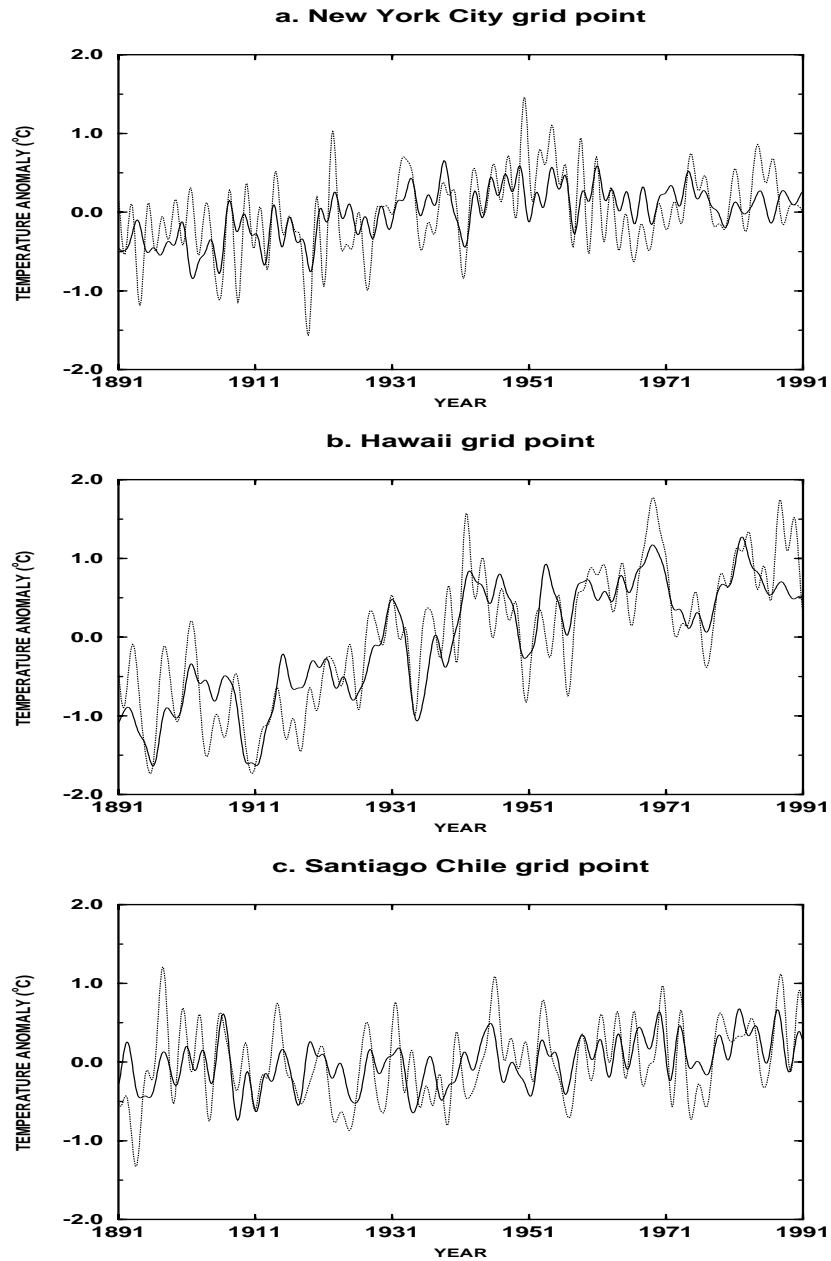


Figure 26: Specific gridpoint time domain signal reconstructions for chosen regions determined from summing over each of the spatiotemporal signals or components isolated in the analysis. The reconstructed signals are shown (solid curves) along with the interannual lowpass of the raw data (dotted curves). (a) North American East Coast Gridpoint (containing New York City). (b) Tropical Pacific Gridpoint (containing main island of Hawaii). (c) South American Grid point containing Santiago, Chile. [From Mann and Park (1994).]

signal describes about 2% of the interannual variance. The total reconstruction describes 34% of the variance. The Hawaiian gridpoint (Figure 26-middle) is dominated by the secular warming signal (61% of the interannual variance), but with a large share of variance also described by the interdecadal signal ($\approx 8\%$). 74% of the total lowpassed variance is explained by the reconstructed signal. Finally, the South American Pacific-coast gridpoint (Figure 26-bottom) is in a region where the direct influence of El Nino can be expected. The reconstruction, not surprisingly, is dominated by the interannual ENSO-band signals ($\approx 20\%$ of the interannual variance). All strong El Nino events [e.g., *Quinn and Neal, 1992*] are clearly captured in the reconstruction. Significant variance is also described by both secular variations ($\approx 5\%$ and 4%) and the interdecadal signal ($\approx 6\%$). The total reconstructed signal describes 35% of the total interannual variance.

The interannual variance explained by the total signal reconstructions range over $\sim 1\%$ to $\sim 75\%$ for the $M = 449$ gridpoints in the analysis, describing $\sim 40\%$ of the total interannual variance in the multivariate dataset. 16% of the total variance is accounted for by the two secular variations, so that the interannual and decadal scale signals describe an important share of the low-frequency multivariate data variance. The variance not explained is attributed in our paradigm to a smoothly varying coloured noise background. However, some of that variance may be attributed to episodic or event-like signals which do not exhibit clear frequency-domain structure (e.g., the impacts of explosive volcanism on surface temperatures – e.g., *Bradley and Jones, 1992*), non-linear or chaotic features of variability [e.g., *Lorenz, 1990*] which are not captured well by a linear frequency-domain decomposition, and in the present analysis the imposition of *a priori* (and hence, not in general optimal) boundary constraints in temporal signal reconstruction from frequency-domain information. An attempt is made to improve upon the latter limitations in the analysis described in the following section.

Summary

Using 100 years of global temperature anomaly data, the MTM-SVD method isolates coherent spatio-temporal oscillations of global climate variability. Organized interannual variability appears to be associated either with ENSO, or extratropical patterns that chiefly involve an NAO pattern. Secular variance is dominated by a globally coherent trend, with nearly all grid points warming in phase at varying

amplitude. A smaller, but significant, share of the secular variance corresponds to a pattern dominated by warming and subsequent cooling in the high latitude North Atlantic with a roughly centennial time scale. Spatial patterns associated with significant peaks in variance within a broad period range from 2.8 to 5.7 years exhibit characteristic ENSO patterns. A recent transition to a regime of higher ENSO frequency is suggested by our analysis. An interdecadal mode in the 15–18 year period range appears to represent long-term ENSO variability. This mode has a sizable projection onto global-average temperature, and accounts for much of the anomalous global warmth of the 1980’s. A quasibiennial mode centered near 2.2 year period and a mode centered at 7–8 year period both exhibit predominantly a North Atlantic Oscillation (NAO) temperature pattern. A “decadal” mode centered on 11–12 year period also exhibits an NAO temperature pattern, and may be modulated by the century-scale North-Atlantic variability. Decadal variability has weak impact on global-average temperature, but gives rise to a strong redistribution of surface heat.

4.2 Northern Hemisphere Joint Surface Temperature and Sea Level Pressure Data

The potential dynamical insights possible from analyzing the joint relationship between surface temperature and atmospheric circulation are well established [e.g., *Namias, 1983; Cayan, 1992ab*]. Here we investigate spatiotemporal signals in joint fields of surface temperature and SLP in the Northern hemisphere which provide near uniform coverage from the tropics through the sub-polar regions for almost a century. A variety of dynamical inferences are possible in the case of the joint field analysis, complementing the observations from the global temperature analysis described in the previous section. Simple relationships between SLP anomaly patterns, inferred surface circulation anomalies, and associated relative advective effects (warming or cooling) may suggest a largely passive response of the temperature field to circulation anomalies. Cold-season warming/cooling along coastlines associated with anomalous inferred onshore/offshore circulation suggests variability in the degree of continental vs. maritime influence. SST anomalies that do not reflect a passive response to atmospheric circulation anomalies may indicate underlying changes in oceanic circulation and ocean-atmosphere exchange. An analysis of the signatures provided by the joint spatial patterns thus provides insight into

the underlying mechanisms of organized climate variations. Comparison with recent coupled ocean-atmosphere model simulations allows us to determine if, beyond empirical statistical inferences, there is some physical motivation for placing confidence in an apparent climatic signal.

The data used consists of the land air and sea surface temperature anomaly dataset described and used in the section 4.1 [*Jones and Briffa, 1992; Jones, 1994*], and gridded Sea Level Pressure data on a similar but staggered $5^\circ \times 5^\circ$ grid in the Northern Hemisphere [*Trenberth and Paolino, 1980* – this dataset is continually updated through the NCAR archive]. We confine our analysis to the latitude band 17.5° - 72.5° N, allowing fairly thorough spatial coverage for both fields. We use the 95 year ($N = 1140$ months) interval 1899-1993 for which both SLP and temperature data are available. Only gridpoints with nearly continuous monthly sampling (very few gaps, and no single gap longer than 12 months) are used, gaps filled as earlier by simple interpolation. This criterion for selection yields a set of $M = 601$ temperature gridpoints and $P = 792$ SLP gridpoints, nearly covering the subtropical-to-subpolar region of the Northern Hemisphere (Figure 27), with some relatively modest spatial gaps in the temperature dataset.

Possible sources of bias in the temperature data were discussed in section 4.1. The gridded SLP exhibit potential biases of their own. The SLP field for any given month represent the spatial interpolation of often sparse observations by hand drawn analyses. These data are of somewhat questionable quality during the earliest (pre 1922) part of the century and during World War II. See *Trenberth and Paolino, [1980]* for a detailed discussion of the quality and potential sources of bias in this data. From a spatial point of view, the data quality is poorest in high-altitude regions with strong cold-season inversions (e.g., large parts of Asia) where sea-level reductions of surface measurements may be flawed. Thus, while there is potentially useful information in these data throughout the 20th century, inferences that depend heavily on the behavior of the data early in the period (such as the spatial details of long-term trends) must be caveated by consideration of the potential data quality problems. Many potential sources of bias, however, are diminished in influence by our seeking organized, dynamically consistent variations in both temperature and SLP fields. Errors that are isolated in time, for example (e.g., data problems associated with World War II) should not have a large influence on our signal detection or reconstruction procedure.

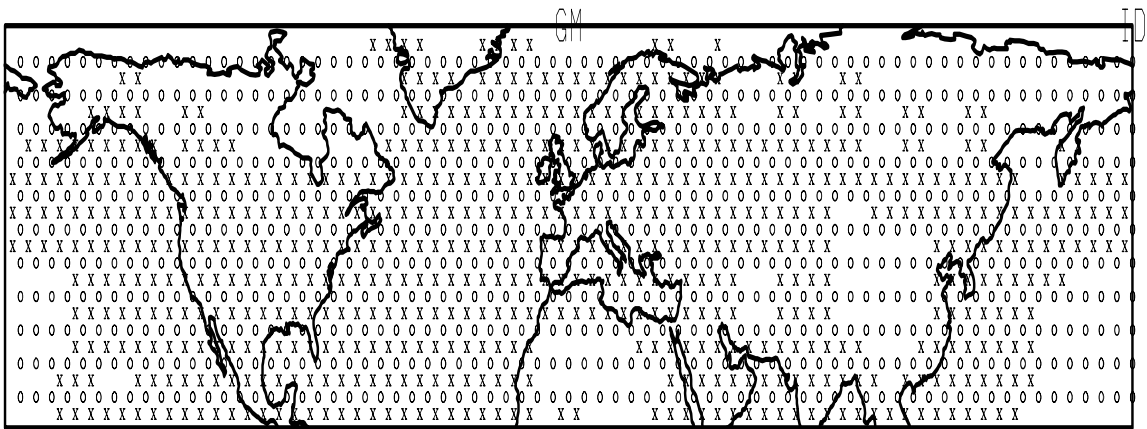


Figure 27: Locations of gridpoints used in analysis, with locations of temperature data indicated by “x”s, and SLP data indicated by “o”s. The grid has latitudinal extent 15° - 70° N and longitudinal extent -180° E to 180° E, with SLP gridpoints located every 5 degrees and temperature gridpoints staggered 2.5 degrees. The positions of the Greenwich meridian and international dateline, as in following plots, is shown for reference. [From Mann and Park (1996b).]

Here we apply a modified version of the standard MTM-SVD analysis described in section 3.1, with the conventional choices $K = 3$ spectral degrees of freedom and bandwidth parameter $p = 2$, to the 95 years of overlapping monthly data for both SLP and temperature data fields. The basic MTM-SVD procedure is modified to determine the dominant modes of narrowband variability in two fields – surface temperature and SLP – simultaneously. This joint mode analysis is accomplished by application of the MTM-SVD analysis to the aggregate data matrix for the two fields, and is a frequency-domain analog of the “Combined Principal Component Analysis” or “CPCA” approach described by *Bretherton et al* [1992] and applied by *Wallace et al* [1992] to the eigendecomposition of joint atmospheric data fields. In the joint field MTM-SVD analysis, each constituent series is standardized for the analysis. To account for the small differences in the sizes of the two datasets ($M = 601$ temperature gridpoints vs $P = 792$ SLP gridpoints), the weights on the corresponding entries in the data matrix are adjusted so that the two fields contribute equal total standardized variance. Temporal signal reconstruction is performed based on the objective boundary constraints described in section 3.2. Signals for which time-evolving frequency structure is detected are reconstructed with the evolutive signal reconstruction technique (section 3.2).

It is appropriate here to note some possible caveats regarding multivariate joint field decompositions. In the context of convention time-domain PCA decomposition, the relative strengths and weaknesses of alternative methods of decompositions for joint or “coupled” fields is explored in some detail by *Bretherton et al* [1992]. Potential deficiencies and limitations of joint field generalizations on time-domain PCA (which are unfortunately sometimes referred to misleadingly as simply “SVD”) have been pointed out recently by a number of authors [e.g. *Newman and Sardeshmukh*, 1995; *Cherry*, 1997]. The primary limitation is that the joint field patterns obtained are not robust, depending quite sensitively, for example, on the relative variance contributions of the two fields. This sensitivity can be understood in terms of the inherent ambiguities in specifying an objective rotation of EOFs in conventional PCA (a nice explanation of the relationship between joint field PCA and rotated PCA analysis is provided by *Cherry* [1997]). In fact, generalizations related to varimax rotation have been suggested as a possible means of specifying more objective joint pattern decompositions [*Cheng and Dunkerton*, 1995]. Nonetheless, much as MTM-SVD largely removes the ambiguity associated with rotation (recall

the discussion of section 3.4), the narrowband decomposition specified by MTM-SVD projects joint spatial patterns which are quite robust, being widely insensitive to variations in the relative contributions of the two independent fields. This point is discussed further below in the context of application to the joint SLP/surface temperature dataset.

LFV spectra

The LFV spectrum for the joint field analysis (Figure 28) is consistent with that obtained in the analysis of global temperature data described in section 4.1 (see Figure 18), with significant variance peaks at the quasibiennial (2.1 – 2.2 year) timescale, within the 3-7 year ENSO period band, and at “quasidecadal” (10-11 year period) and “interdecadal” (16-18 year period) timescales. Two significant modes are also identified within the secular band corresponding to variability on timescales $\tau > 48$ year in the 95 year dataset. It is worth noting that the quasidecadal and interdecadal peaks exhibit a less distinct signal separation than was evident in the corresponding LFV spectrum of the global temperature data; this is not especially surprising given that the differing spatial signatures of the two signals were most evident (compare Figures 22 and 23) in the tropical and southern latitudes not present in the sampling of the joint data fields analyzed here. A restricted sensitivity test (see Figure 28, top) using 85-year data sub-segments long enough to resolve the secular and relatively closely spaced quasidecadal and interdecadal peaks demonstrates relative stability in the significance of the peaks detected in the analysis of the full 95 year dataset. For the interannual signals, a more liberal sensitivity test or “evolutive analysis” can be performed, as described below. The LFV spectrum was further found to be similar whether the MTM-SVD decomposition was performed on the two fields (SLP and temperature) with equal contributions of variance, or performed on the temperature data alone with the resulting signals linearly projected onto the SLP fields. Somewhat different results were obtained when the analysis was performed on the SLP field alone, which we attribute to the questionable quality of the SLP data (especially early in the 20th century), which limits their usefulness by themselves for signal detection and reconstruction.

Comparison of LFV spectra for all-seasons, warm- and cold-season data (Figure 28, bottom) suggest that secular and interdecadal signals are seasonally robust, although the spatial signature of these signals, mostly in mid- and high-latitudes, are

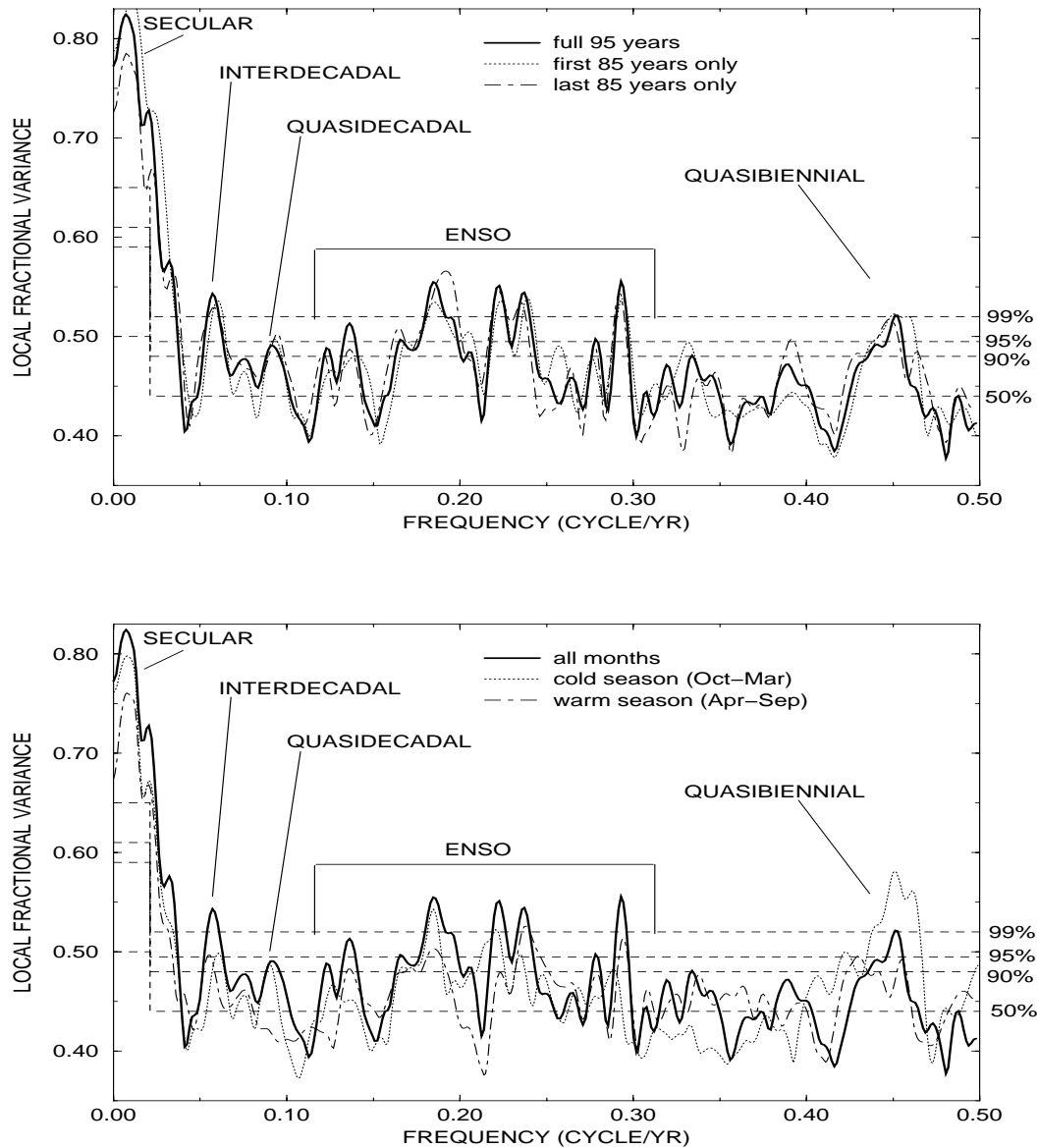


Figure 28: (top) LFV spectrum for the 1140 month (95 year) joint surface temperature and SLP dataset. Horizontal dashed lines denote median (50%), 90%, 95%, and 99% confidence limits from bootstrap resampling. (bottom) Comparison of LFV spectrum for all-months and cold and warm season analyses. The numerical vertical scale and significance levels shown apply to the all-months analyses. The LFV spectra for the cold and warm-season only analyses are slightly renormalized (by the factors ≈ 1.02 and 0.98 respectively) so that the quantiles of the null distribution and significance levels shown apply roughly for each case, even though the effective number of degrees of freedom in the sample varies between the two distinct seasonal windows. [From Mann and Park (1996b).]

shown below to display seasonally-specific features. The interdecadal signal appears to derive its strong ($> 99\%$) significance in the all-seasons analysis from more moderate amplitude, but consistently significant expression, during both seasons. In contrast, the quasidecadal signal appears as a distinctly cold-season phenomenon, as prominent as the interdecadal signal during that season, but completely absent in the warm season. The ENSO-band variance peaks show some distinct differences between the all-seasons and seasonal analyses. The quasibiennial signal is significant during both independent seasons, but is clearly stronger during the cold season (we have checked, through analysis of synthetic examples, that no significant bias is introduced by the proximity of quasibiennial frequencies to the $f_N = 0.5$ cycle/year Nyquist frequency in the case of these seasonal analyses). It is possible that a seasonally-persistent signal is only *detectable* above noise at certain times in our analysis. For example a low-frequency carrier signal in tropical SST may only lead to a larger scale expression during the winter season when high-amplitude extratropical circulation anomalies are induced by associated tropical heating anomalies. Since tropical coverage in our spatial sampling is marginal, such a signal may not be detectable during the warm season, as the associated tropical carrier signal would be missed. Such limitations should be kept in mind. An independent analysis of the spatial and temporal patterns for both seasons provides insight into such issues. An evolutive LFV spectrum (Figure 29) was calculated using a $N = 40$ year moving window through the dataset. This choice of window width admits a frequency resolution 0.10 cycle/year so that the quasidecadal and interdecadal peaks of Figure 28 are not distinguishable, and only periods shorter than 20 years can be confidently separated from secular variations. The relative stability of interannual signals, and the potential time-dependence of the amplitude and frequency characteristics, can however be tested. A 40 year window, allows roughly one phase discontinuity per 13 years. Thus, low-frequency (5-7 year timescale) ENSO variability is assumed to maintain coherence (though varying in amplitude) over 2-3 “cycles”. In contrast, the quasibiennial oscillation is statistically modeled as being phase-coherent (and varying slowly in amplitude) over roughly 5 cycles with a 40 year window, which may imply a physically unrealistic timescale of coherence. For this signal we employed (see below) a somewhat shorter 20 year window in evolutive time-reconstruction of the signal. A alternative wavelet generalization of the MTM-SVD approach [*Lilly and Park, 1995; Park and Mann, 1997*] allows for an automatic scaling of period

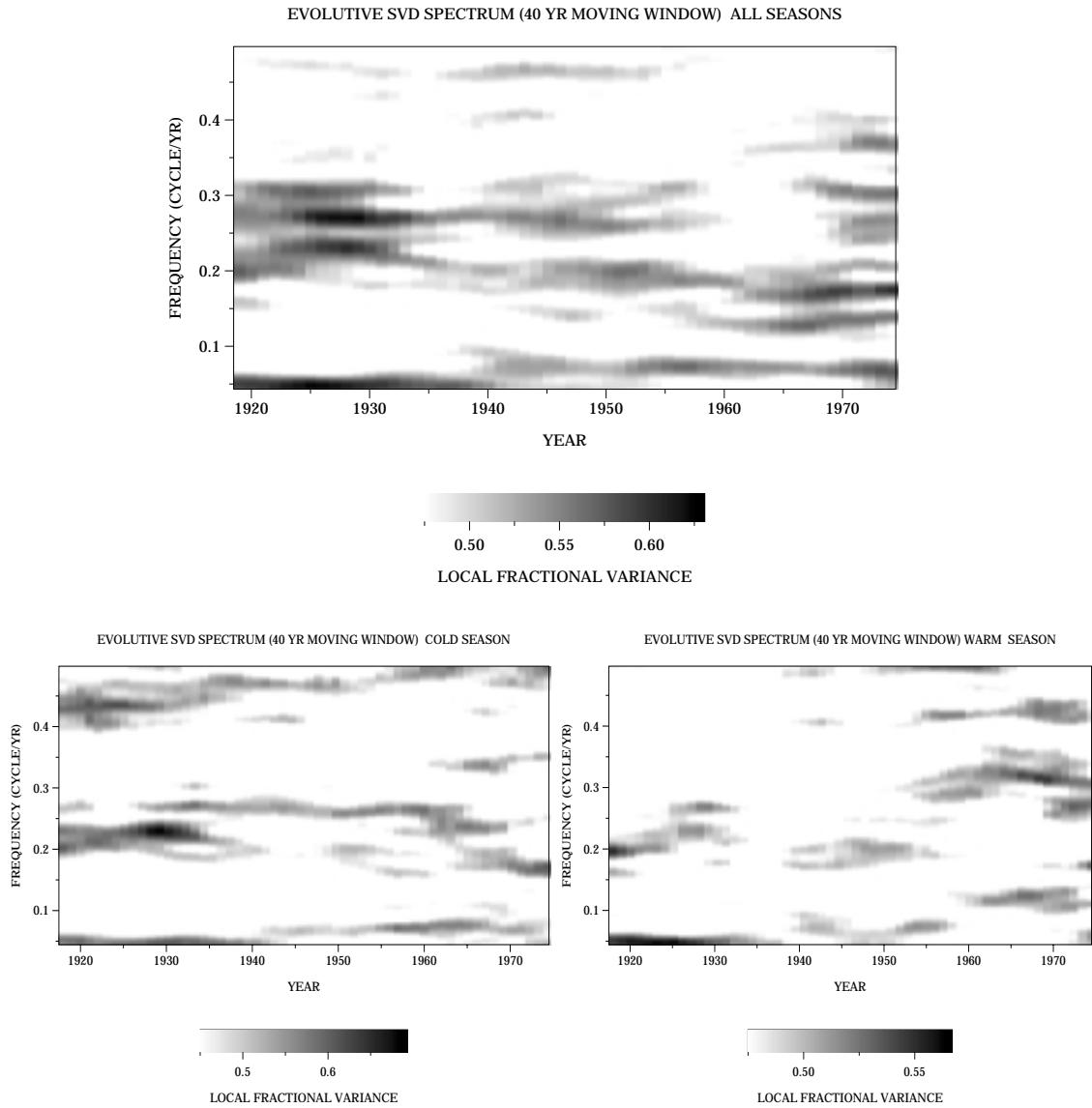


Figure 29: Evolutive LfV spectrum based on performing the SVD analysis in a moving 40 year window for (top) all seasons, (bottom-left) cold-season, (bottom-right) warm-season. The amplitude of the spectrum as a function of time (center of moving window) and frequency is shown with the indicated grayscale, with confidence levels associated with the values given in Figure 28. Only the frequency range resolvable from secular variations ($f > 0.05$ for a 40 year moving window) is shown. [From Mann and Park (1996b).]

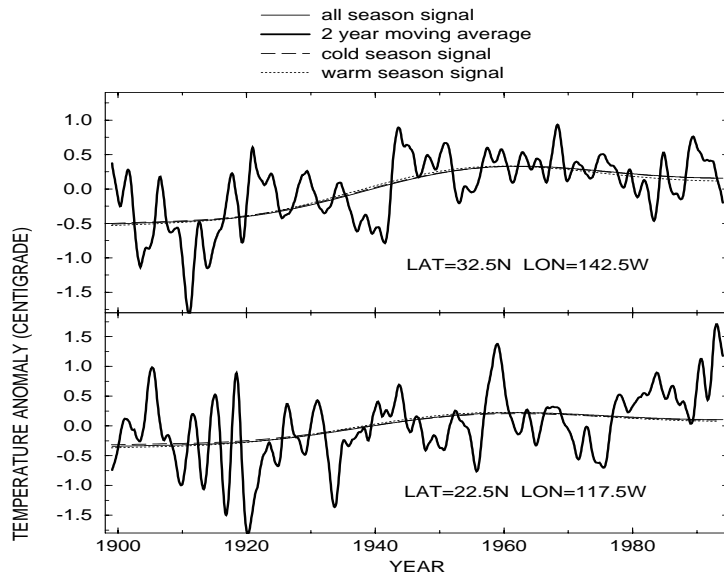
and assumed phase-coherence timescale.

In the all-months analysis (Figure 29, top), there is clear evidence of organized frequency-domain structure within the ENSO band, with two dominant bands of variability clustered around 3-4 year period and 5-7 year period bands, that exhibit appreciable frequency and amplitude modulation. This behavior is *approximated* in the full window analysis by amplitude-modulated statistically significant quasi-oscillatory components centered near 3, 4, 5, and 7 year periods (see .3, “ENSO Signal” of section 4.1). A parsimonious picture of two distinct low-frequency (“LF”) and high-frequency (“HF”) bands of ENSO-related variance is thus indicated in the evolutive analysis. This description suggests a degree of frequency-domain organization which belies a simple *episodic* picture of ENSO, and reinforces the utility of a frequency-domain analysis of ENSO variability. The cold- and warm-season only analyses show streaks of variance within these two same dominant bands, but the relative lack of frequency domain structure in these cases relative to the all-months analysis, implies a signal that is not simply phase-locked to the annual cycle. Nonetheless, the separate cold- and warm-seasonal signal reconstructions are essential to understanding the relationship between tropical and extratropical expressions of the signal. The seasonal analyses substantiate the cold-season dominance of the quasibiennial signal, and reveals a drifting trend towards higher frequency during this century. This frequency modulation is consistent with the relationship that was observed between secular warming and the envelope of the *fixed-frequency* reconstruction of the quasibiennial signal in the global temperature analysis (see section 4.1, “Quasibiennial Signal” and Table 4).

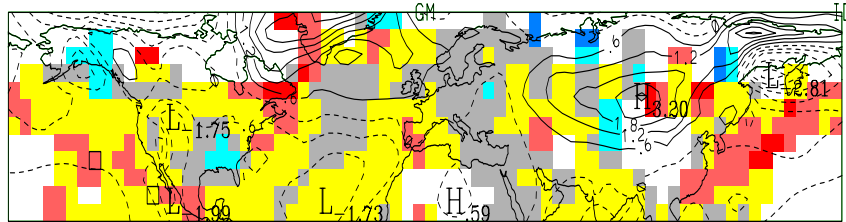
Secular Signals

The primary secular mode (Figure 30), accounts for 77% of the near zero-frequency variance in the joint SLP-temperature dataset, and is associated with the secular trend in the global temperature data (i.e., the global warming signal of section 4.1, Figure 20). The warming pattern is evident in both cold and warm-seasons, although certain regions show a marked seasonal-dependence. For example, secular warming in eastern Asia and the North Atlantic is present only during the cold season, which might be related to winter land and sea-ice albedo effects.

The warming is coherent with regional SLP anomalies that imply altered atmospheric circulation patterns. In the southeastern U.S., the presence of enhanced



COLD SEASON



WARM SEASON

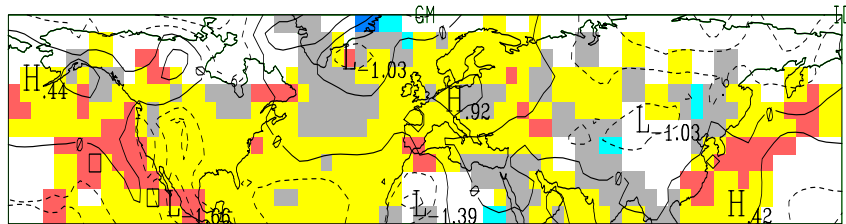


Figure 30: Spatial and temporal pattern of primary secular mode. (top) Time reconstructions for reference temperature gridpoints in the (i) central subtropical and (ii) eastern tropical Pacific, along with 2-year smoothed raw gridpoint data. (middle) Cold-season and (bottom) warm-season spatial pattern. As in all similar subsequent spatial plots, temperature anomalies are indicated with the color scale shown. SLP patterns are contoured in units of millibars (mb), and reference gridpoints are indicated by a box (temperature gridpoint) or boxed “x” symbol (SLP gridpoint).

cold-season cooling and warm- season warming might be related to anomalous circulation patterns (e.g., a trough-like trend over North America discussed elsewhere by *Mann et al* [1995a]) that favors a more continental influence in the region. Over the North Atlantic, a winter season north-south trend resembles the reverse of the NAO pattern [see *Deser and Blackmon*, 1993]. This pattern could explain some of the asymmetry in warming along the western and eastern margins of the North Atlantic basin, although changes in heat transport by the Gulf Stream have also been speculated by *Deser and Blackmon* [1993]. Qualitatively similar circulation anomalies have been variously observed in GCM simulations of the climatic response to greenhouse gas forcing [*IPCC*, chapter 6, 1996; *Oglesby and Saltzman*, 1992; *Marshall et al.*, 1994]. Other circulation anomalies are suggested. The questionable quality of the earlier SLP data, however, demands a cautious interpretation of long-term trends in SLP. The pronounced SLP anomalies near Northern Japan/Sea of Okhotsk, for example, correspond to the discontinuous early behavior of a small number of gridpoints.

The secondary secular mode (Figure 31) accounts for a lesser, but nonetheless significant, 21% share of the secular band variance. This mode is associated with the multidecadal pattern of high-amplitude warming and subsequent cooling in the North Atlantic isolated in the global temperature data (section 4.1). The objective time-domain signal reconstruction procedure employed in this analysis favours a roughly 75 year period “oscillation” timescale. This timescale, though poorly estimated in the context of a single secular variation, is consistent with persistent 50-100 year multidecadal/century-scale oscillations in proxy climate data (see section 4.3).

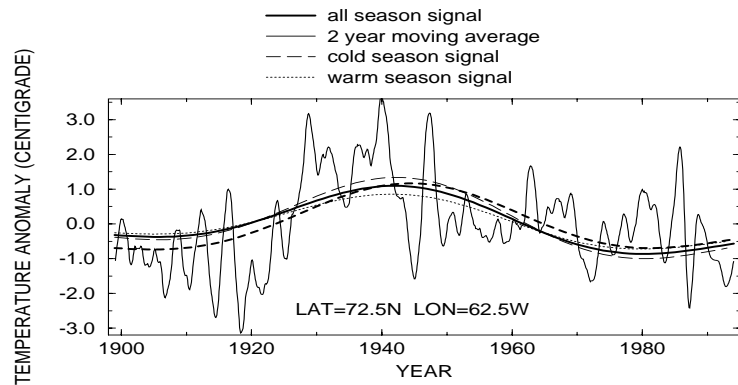
Arguments for a relationship with the thermohaline circulation are further strengthened here by the joint relationship between sea surface temperatures and overlying SLP patterns. Delworth and collaborators [*Delworth et al*, 1993; 1997] have demonstrated that century timescale (40-80 year period) oscillatory behavior can arise from climate mechanisms involving the thermohaline circulation, and perhaps coupled ocean-atmosphere processes, based on a 1000 year coupled ocean-atmosphere model simulation. In that study, a pattern of anomalously warm SSTs in the mid-latitude and polar North Atlantic, and weaker cold anomalies in parts of tropical/subtropical North Atlantic, was associated with the enhanced-thermohaline circulation phase of the oscillation. The enhanced circulation state was in turn accompanied by a pattern of negative high-latitude and positive low-latitude SLP anomalies over the North

Atlantic. Whether the atmospheric pattern is simply a passive response or an intrinsic component to the underlying feedback system remains to be established. The opposite features were associated with the weakened state of thermohaline circulation.

We find additional support for such a coupled pattern in the multidecadal signal isolated here. The North Atlantic regional features of the signal (consistent with those isolated in the associated global temperature pattern) confirm the comparison drawn by *Kushnir* [1994] between observed North Atlantic multidecadal variations and the multidecadal oscillations patterns of *Delworth et al* [1993 – henceforth DEL93]. We find a pattern of surface temperature variability in the North Atlantic, evident in both cold and warm seasons, that resembles the surface temperature patterns of the DEL93 signal. Furthermore, consistent with DEL93, we find a persistent relationship between anomalous warm SSTs in the high-latitude North Atlantic and anomalous low SLP over part of the polar North Atlantic (Labrador Basin/Baffin Bay region). However, a *convincing* similarity is only found during the warm season, during which low pressure presides over the entire polar North Atlantic region during the warm SST phase of the signal. Thus, the agreement between the observed and modeled century-scale signal is imperfect. The substantial opposite-sign surface temperature anomalies over much of Eurasia during the cold-season (note that the cold-season dominates the pattern of the all-seasons global temperature analysis described by Figure 20) appears to be related to a breakdown of mid-latitude westerlies in that region during the warm-North Atlantic phase inferred from the SLP pattern, associated with a decrease in their moderating influence on the cold-season Eurasian climate.

Interdecadal Signal

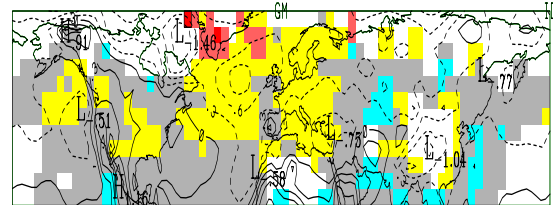
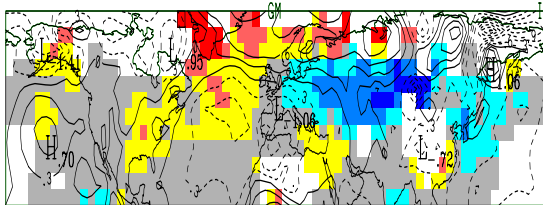
The interdecadal signal of Figure 22 is established as a significant signal in joint temperature and SLP over the Northern hemisphere (Figure 32-Figure 34), with a suggested Pacific basin center of activity. Although a number of possible mechanisms for such roughly bidecadal timescale variability were discussed in section 4.1, the joint-mode analysis provides evidence for the particular mechanism advocated in the modeling study of LB94. In that study, oscillatory ~ 20 year period behavior centered in the North Pacific was generated in a roughly 70 year simulation of a coupled ocean-atmosphere model. A delayed oscillator mechanism was



COLD SEASON

WARM SEASON

warm phase



cold phase

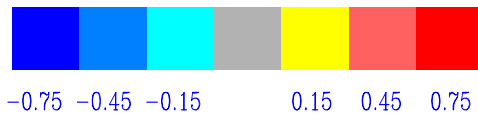
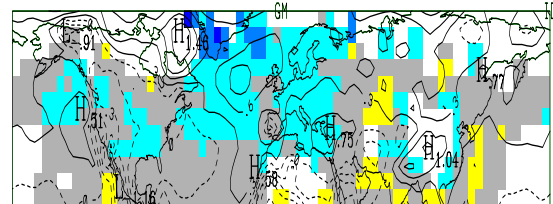
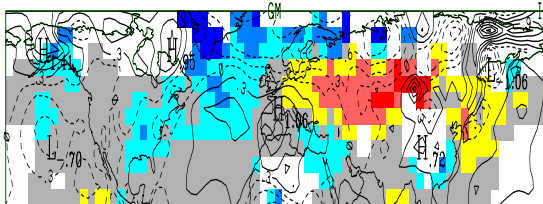


Figure 31: Spatial and temporal pattern of secondary secular mode. (top) Time reconstructions for a reference temperature gridpoint in the North Atlantic, along with smoothed raw data series. An additional (thick dashed) curve shows the additional contribution of the primary secular mode to the total secular variation at this gridpoint. (bottom) Cold-season (left) and warm-season (right) spatial patterns of signal, showing in each case the phases of the signal corresponding to a warm (upper) and cold (lower) North Atlantic.

argued for by LB94, involving feedbacks between gyre heat transport, changes in heat content and SST, and anomalous atmospheric circulation in the extratropical Pacific. The interdecadal signal isolated in the joint field analysis exhibits remarkable resemblance in both temporal (i.e., both the ~ 20 year period and the irregular modulated nature of the oscillation) and spatial (Fig. 33) characteristics to the LB94 signal. During the extreme of the cycle associated with anomalous negative oceanic heat content in the central North Pacific in LB94, for example, LB94 observe anomalous positive SSTs in the lower-latitude North Pacific. This anomalous SST pattern is associated with an increased latitudinal SST gradient, accompanying anomalous low wintertime SLP over the North Pacific and inferred strengthening of mid-latitude westerlies. At the other extreme of the cycle, these patterns are reversed. This relationship is argued by LB94 to reflect a sequence of positive and negative feedbacks whereby changes in the meridional SST gradient force an equivalent barotropic response in the planetary wave structure. This altered circulation leads to changes in the latitudinal gradient in windstress curl, spinning down the subtropical North Pacific gyre, altering the poleward heat transport by the gyre and thus, the SSTs themselves. The mode is inferred to be an internal eigenmode that is excited by stochastic forcing.

In the cold-season (Figure 33), the peak positive (negative) SLP anomaly over the North Pacific is associated with a pattern over North America resembling the positive (negative) phase of the Pacific/North American teleconnection pattern [PNA – see *Barnston and Livezey, 1986*]. The “PNA” signature of this interdecadal signal is distinct from the similar but spatially offset “TNH” pattern typically connected with the interannual ENSO signal (see “ENSO Signal” section below), consistent not only with LB94, but other studies which have linked interdecadal variability with the PNA pattern [e.g., *Trenberth, 1990; Mann and Park, 1993*]. The ~ 20 year timescale of an oscillatory cycle is attributed by LB94 to the intrinsic spinup timescale of the North Pacific gyre, with the adjustment in gyre heat transport lagging windstress changes by several years, thus providing feedbacks that support oscillatory behavior. The warm-season expression of the signal (Figure 34) emphasizes the seasonal persistence (and consistency) of SST anomalies in the Pacific which appear to lead to cold season-specific excitation of high-amplitude extratropical circulation anomalies. This seasonal distinction is also consistent with the LB94 mechanism. One notable exception is an implied strengthening and weakening

of the Asian monsoonal pattern associated with seasonally-opposite SLP variations over central Asia.

While some compelling similarities are found with the simulations of LB94, there are notable discrepancies as well. For example, the interdecadal pattern of LB94 is strongest over the western North Pacific where the model SST gradient is largest. In contrast, our observed pattern exhibits the largest SST gradient anomalies in the eastern North Pacific. Furthermore, high amplitude variability in the Atlantic region and elsewhere suggests strong downstream teleconnections or perhaps even coupling with Atlantic basin processes. Such issues are discussed further for the “Quasidecadal” signal below. This monsoonal pattern discussed above is just one of several apparent connections with low-frequency variability in ENSO which are also not explained by the extratropical mechanism of LB94, and may indicate the added importance of coupling between the extratropics and tropics. This relationship is evident not only in the ENSO-like patterns of warming and cooling (see also section 4.1) but in the mild positive east-west SLP gradient across the tropical Pacific coinciding with anomalous warmth in the eastern tropical/subtropical Pacific. Furthermore a close association between the signal and decadal-scale variations in the southern oscillation [SO – see Fig 32 and also, *Trenberth*, 1990] and NINO3 SST indices (both exhibit spectral coherences significant at $\sim 95\%$ confidence level within the interdecadal frequency band) is evident. Such connections suggest some relationship with low-frequency changes in ENSO. It is possible that the high-amplitude extratropical variations may force a weaker modulation of the tropical Pacific, thus impacting the ENSO phenomenon. Conversely, a more complicated coupled tropical /extratropical mechanism could be at work, perhaps combining dynamical mechanisms explored by both LB94 and *Gu and Philander* [1997].

In terrestrial regions, the temperature patterns appear consistent with the effects of altered atmospheric circulation on sensible heat redistribution. For example, the cold anomaly in the southeastern U.S. and warm anomaly in the Northwestern U.S. are consistent with sensible heat transport by the anomalous PNA-type pattern. This phase of the cycle is associated with a significant share of the general hemispheric (and in fact global, as shown in section 4.1) warmth that was observed during the mid-to-late 1980s (as well as the late 1940s and early 1970s), but the signal projects a tendency for negative temperature anomalies during the early-to-mid 1990s, counter to the continued acceleration of warming which, as discussed earlier,

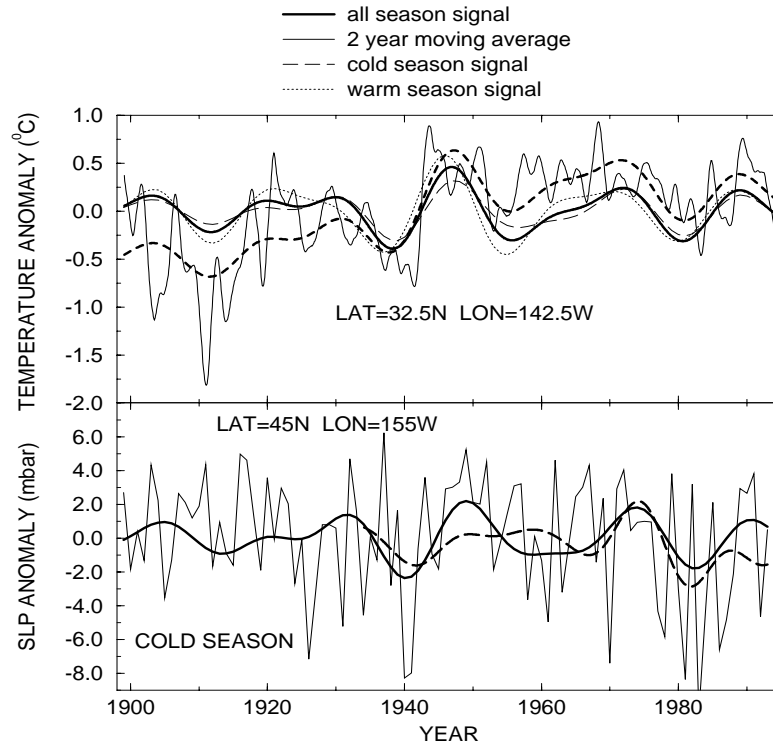


Figure 32: Temporal pattern of interdecadal mode for (i) reference subtropical east/central Pacific temperature gridpoint and (ii) reference mid-latitude central Pacific SLP gridpoint (cold season) along with the smoothed raw data series. The thick dashed line in (i) indicates the sum of the secular warming trend (see Figure 24) and interdecadal mode. The thick long-dashed line in (ii) shows the interdecadal and longer-term (lowpassed with a notch at 10 year period) variations in the SOI (scaled by a factor of 3 in mb) since continuous data is available, demonstrating an in-phase relationship of decadal-scale variations with the projection of the interdecadal signal onto cold-season winter North Pacific SLP. [From Mann and Park (1996b).]

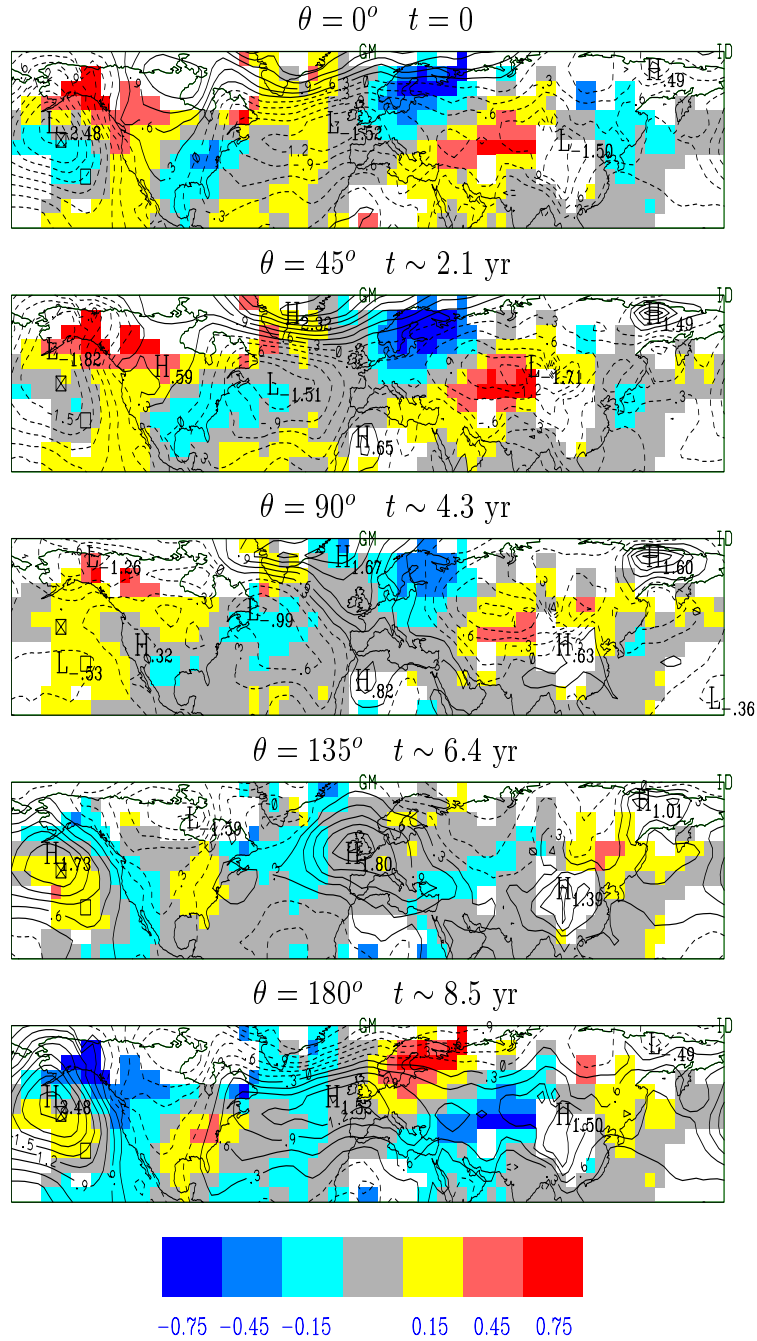


Figure 33: Cold-season spatial pattern of interdecadal signal shown at progressive intervals, spanning one half of a complete (~ 17 year) cycle. The absolute timing of relative phases of the pattern are defined by the reference temperature and slp series shown in Figure 32. [the signal progression here and in all similar following plots is opposite to that erroneously shown in Mann and Park (1996b).]

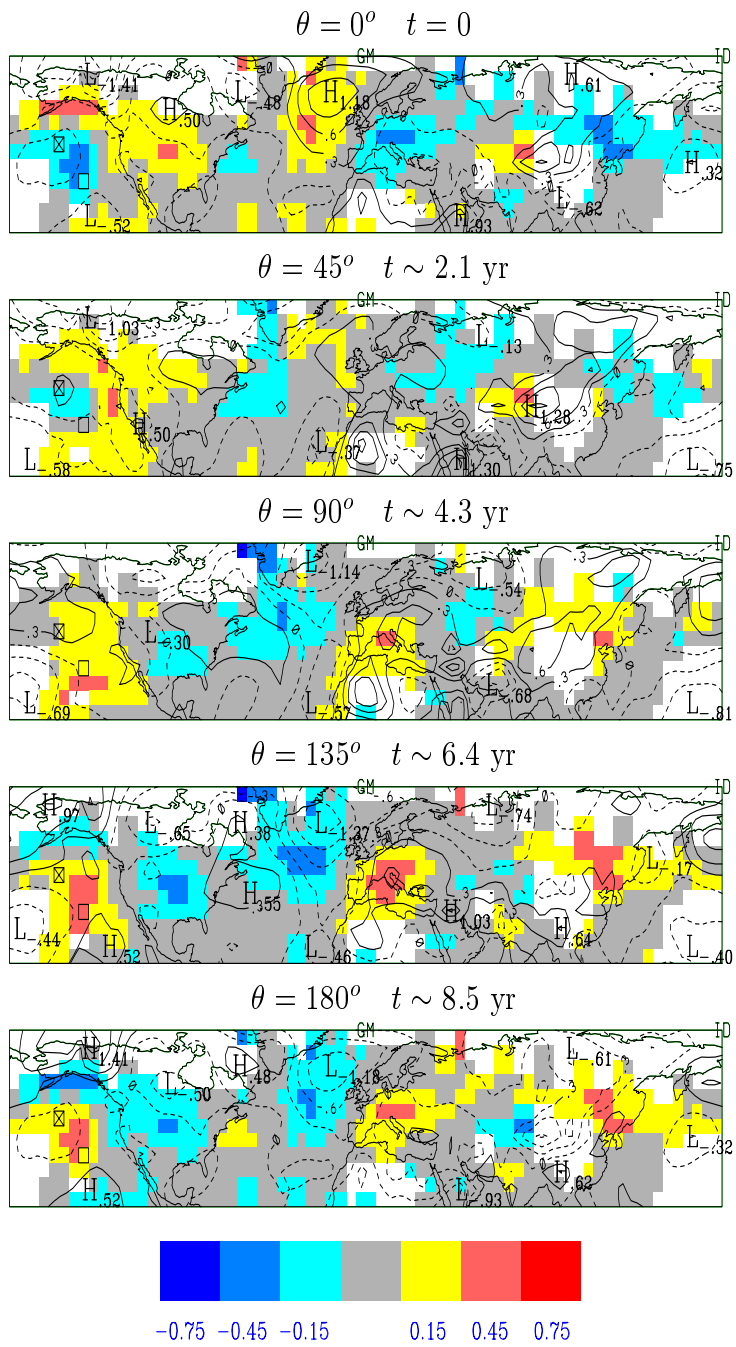


Figure 34: Warm-season spatial pattern of interdecadal signal. Convention same as in Fig 33.

may relate to non-stationary behavior in ENSO [*Trenberth and Hoar, 1995*].

Quasidecadal Signal

In contrast to the interdecadal signal discussed above, the quasidecadal (10-11 year period) signal (Figures 35,36), as its counterpart in global temperature data (Figure 23) appears to be tied more closely to the North Atlantic region. Weaker variability is observed throughout the remaining Northern Hemisphere. The more widespread global temperature data of section 4.1 supports a more distinct separation (i.e., a “spectral gap” – compare Figures 18 and 28) between the quasidecadal and interdecadal signals than does the joint field analysis. With the short duration of instrumental data available and only a Northern Hemisphere domain, it is more difficult to distinguish adequately between the statistical models of independent interdecadal and quasidecadal spatially distinct processes, and a single more broadband, coupled basin signal.

The quasidecadal signal at certain phases exhibits an NAO-like SLP pattern (Figure 36) consistent with observations of quasidecadal variability in the NAO index itself [*Hurrell, 1995*]. However, the SLP pattern is more monopole, with a higher amplitude center of variation in the subpolar North Atlantic than in the subtropics. This distinction underscores the danger of analyzing simple indices such as the NAO for inferences into low-frequency climatic variability; while the pattern of Figure 36 projects onto an NAO or other diagnostic index of North-South SLP gradients in the North Atlantic, it does not in fact resemble the classic NAO pattern [e.g., *Rogers, 1984; Lamb and Pepler, 1986*]. The observed pattern, furthermore, is not associated with a standing SLP dipole, but rather a time-evolving SLP anomaly pattern. Cold conditions over Northern Europe/Western Eurasia for example are consistent with the inferred breakdown of maritime influence due to anomalous low SLP centered over Great Britain during the 3rd snapshot shown. This pattern is almost orthogonal to an NAO anomaly pattern.

Both temperature and SLP signatures over the North Atlantic are similar to that identified by *Deser and Blackmon [1993]* for quasidecadal North Atlantic climate variations, but the signal appears to exhibit a wider hemisphere-scale influence. *Mann et al [1995a]* noted that the quasidecadal signal dominates the low-frequency winter circulation variability in the Great Basin (compare Figure 36 in this region). They were able to demonstrate an association between the anomalous low pressure

over the region during the phase of the 3rd snapshot of Figure 36 and coincident increased storm activity/increased regional precipitation anomalies leading to an increasing trend in the Great Salt Lake volume. In contrast with the PNA circulation anomalies associated with the interdecadal signal discussed above, which are interpreted as a downstream perturbation set up by Pacific basin climate variations, we infer here an origin in the high-amplitude variations centered in the Atlantic. The notion that an Atlantic source of variability would have such strong upstream impacts is counterintuitive, but nonetheless consistent with studies that have established the importance of retrogressing long-wave disturbances during the cold season over North America [e.g., *Lanzante, 1990*].

No connection is found between the quasidecadal signal and ENSO. Spectral coherences with quasidecadal band variations in NINO3 and the SOI are statistically insignificant. The purely cold-season nature of the signal in this analysis seems to arise from that fact that its most prominent features – i.e., the extratropical circulation and surface temperature anomalies in the North Atlantic – are cold-season dominant. The signal may persist year-round in the tropics which are only weakly represented by our largely extratropical spatial sampling. The cold-season expression in the extratropics may also indicate a carrier signal beneath the seasonal thermocline, only expressed at the surface during the winter period when stratification is weak and deep convection occurs [see e.g., *Dickson, 1997* and references therein].

LB94 suggest that a mechanism similar to that discussed for the interdecadal Pacific-centered signal, combined with a narrow basin geometry, could lead to an analogous shorter period, quasidecadal signal centered in the Atlantic. Our study offers some limited support for this hypothesis, as the relationship between the evolving patterns of SLP and SST in the North Atlantic show some of the same features. For example, the initial snapshot of Figure 36 exhibits a consistent pattern of anomalous high pressure associated with inferred weakened westerlies in mid-latitudes, and a decreased SST gradient over much of the Atlantic. However, the mechanism of LB94 does not explain some very important features of the signal, most notably the tropical SST dipole associated with the larger-scale expression of the signal as shown earlier in Figure 23.

A number of mechanisms besides that of LB94, could explain such features or even the signal itself. Some researchers indicate the importance of low-frequency

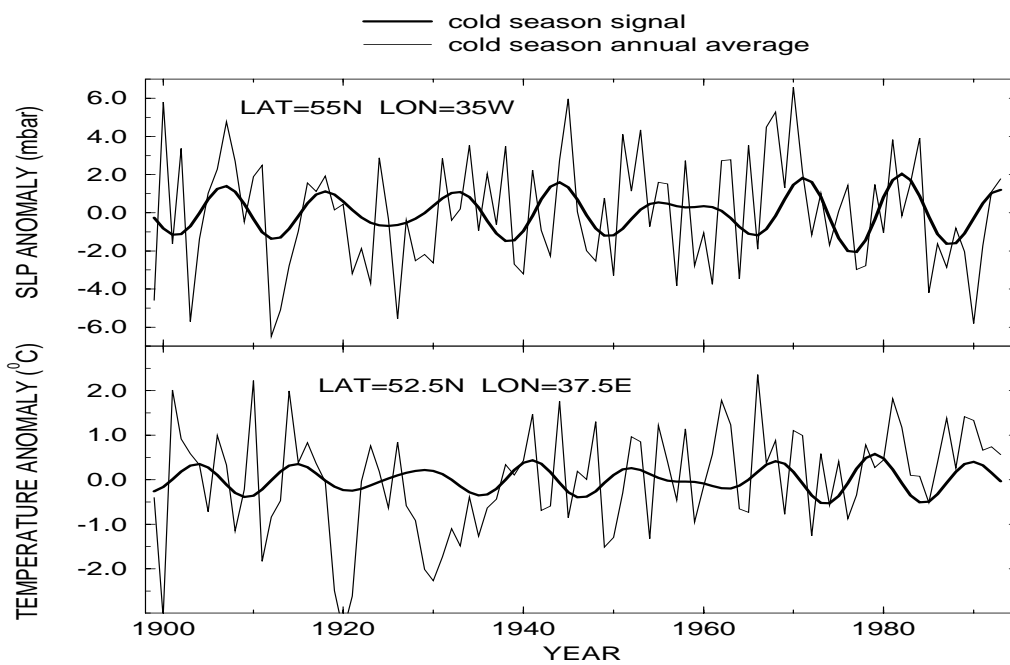


Figure 35: Time reconstruction of ~ 10 - 11 year quasidecadal signal for (i) reference mid-latitude/sub-polar North Atlantic SLP gridpoint (cold season) and (ii) similar latitude western Soviet temperature gridpoint. Note the 90° phase lag between the two variations, as expected from the discussion in the text. [From Mann and Park (1996).]

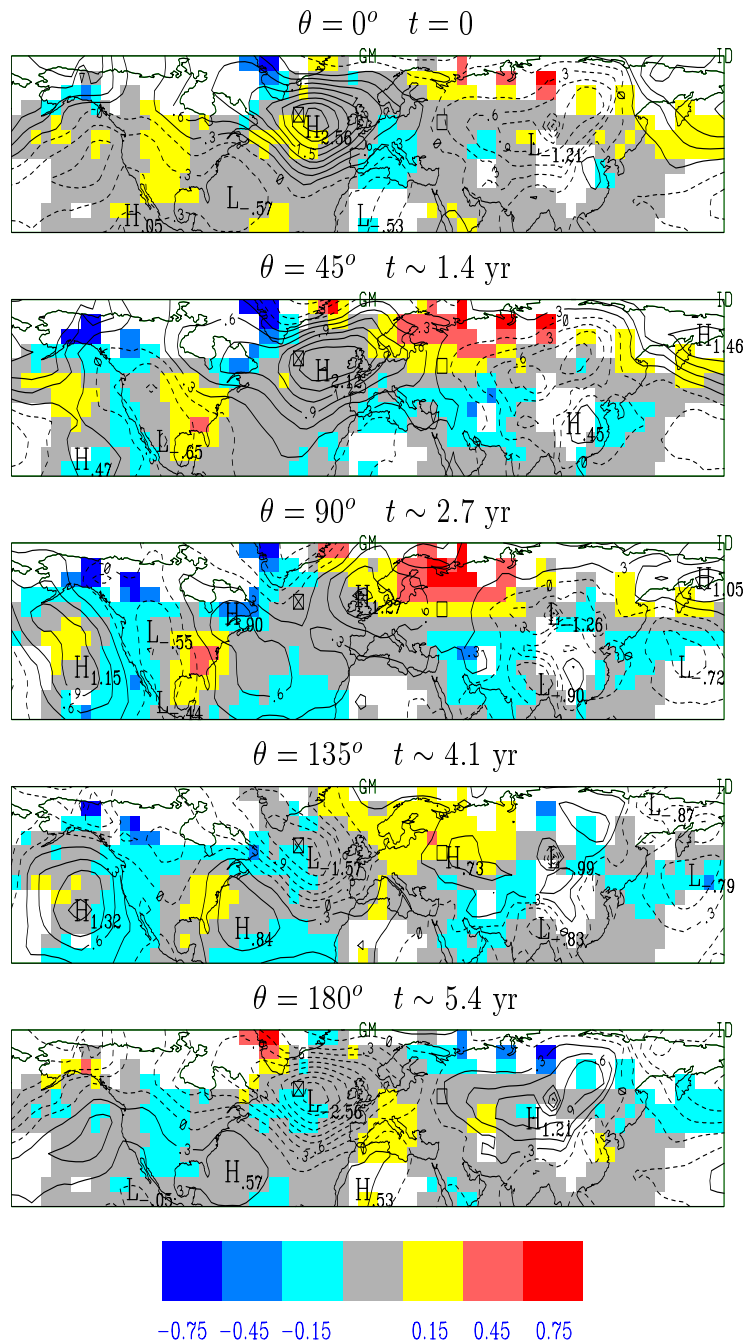


Figure 36: Cold-season spatial pattern of quasidecadal signal spanning one half of complete (~ 11 year) cycle. The initial snapshot corresponds to the peak positive winter SLP anomaly in the North Atlantic.

advection of salinity anomalies by gyres [Weaver *et al.*, 1991] or the interaction of thermal and salinity anomalies [Yang and Neelin, 1993] on deep water production, and tropical ocean-atmosphere interactions [Mehta and Delworth, 1994]. Chang *et al.* [1997] present a simple, but compelling, thermodynamic coupled ocean-atmosphere mechanism which leads to a quasidecadal oscillating SST dipole (and corresponding wind anomalies) in the tropical Atlantic. Tourre *et al.* [1997] propose how the interaction of such tropical anomalies with other processes, such as gyre-scale advection, can lead to a full-basin expression of signals that originate in the tropical Atlantic.

Several studies have also presented possible connections between the ~ 11 year solar cycle and quasidecadal climate fluctuations. Such statistical relationships have typically been established with stratospheric and upper tropospheric fluctuations [e.g., Labitzke and van Loon, 1988; Tinsley, 1988], rather than lower atmospheric or surface climate data. While we do not find evidence for a statistically significant correlation with the ~ 11 year sunspot cycle in this quasidecadal *surface* climate signal, there is some evidence for phase-locking during the past few decades [see also Mann *et al.*, 1995b] coinciding with a period of high amplitude solar cycle variations. The argument that an internal quasidecadal eigenmode could resonate with such external forcing, given sufficient amplitude, cannot be ruled out. However, the direct forcing (i.e., the irradiance changes) associated with such solar variations is small [see e.g., Lean *et al.*, 1995] and some as yet unestablished means of amplification of the forcing [e.g., cloud electrification – Tinsley, 1988 or modulation of stratospheric ozone concentrations – Robock, 1996] would be required for a viable mechanism.

ENSO Signal

Although the region sampled in this analysis does not include the equator or southern hemisphere, enough of the tropical Northern hemisphere is included that relationships with ENSO can be examined. The domain includes a sizable region known to experience the direct effects of both El Niño and the Southern Oscillation or “SO” [see e.g., Trenberth and Shea, 1987]. Our analysis thus complements similar previous analyses of ENSO-related climate variability [Barnett, 1991] where tropical ENSO-band climate patterns were examined, by using a long, widespread, though less tropics-dominated dataset.

The time-domain signal is reconstructed based on the evolutive procedure (employing a 40 year moving window) recognizing the distinct low-frequency “LF” and

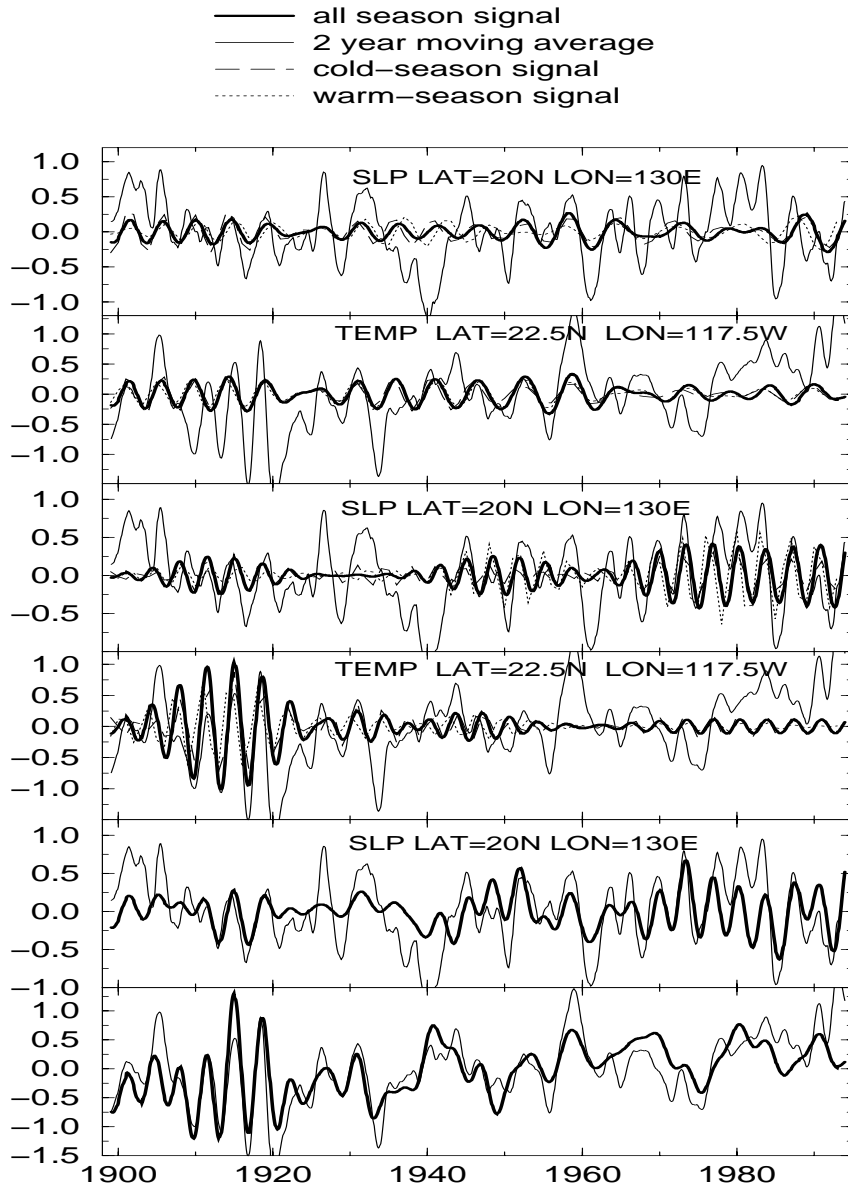


Figure 37: Time reconstruction for (i) low-frequency component, reference SLP gridpoint in the tropical western Pacific, (ii) low-frequency component, reference temperature gridpoint in the eastern tropical Pacific, (iii) high-frequency component, same SLP gridpoint, (iv) high-frequency, same temperature gridpoint, (v) sum of interdecadal and both ENSO components, SLP gridpoint, (vi) sum of interdecadal and both components + secular warming signal, temperature gridpoint. [From Mann and Park (1996b).]

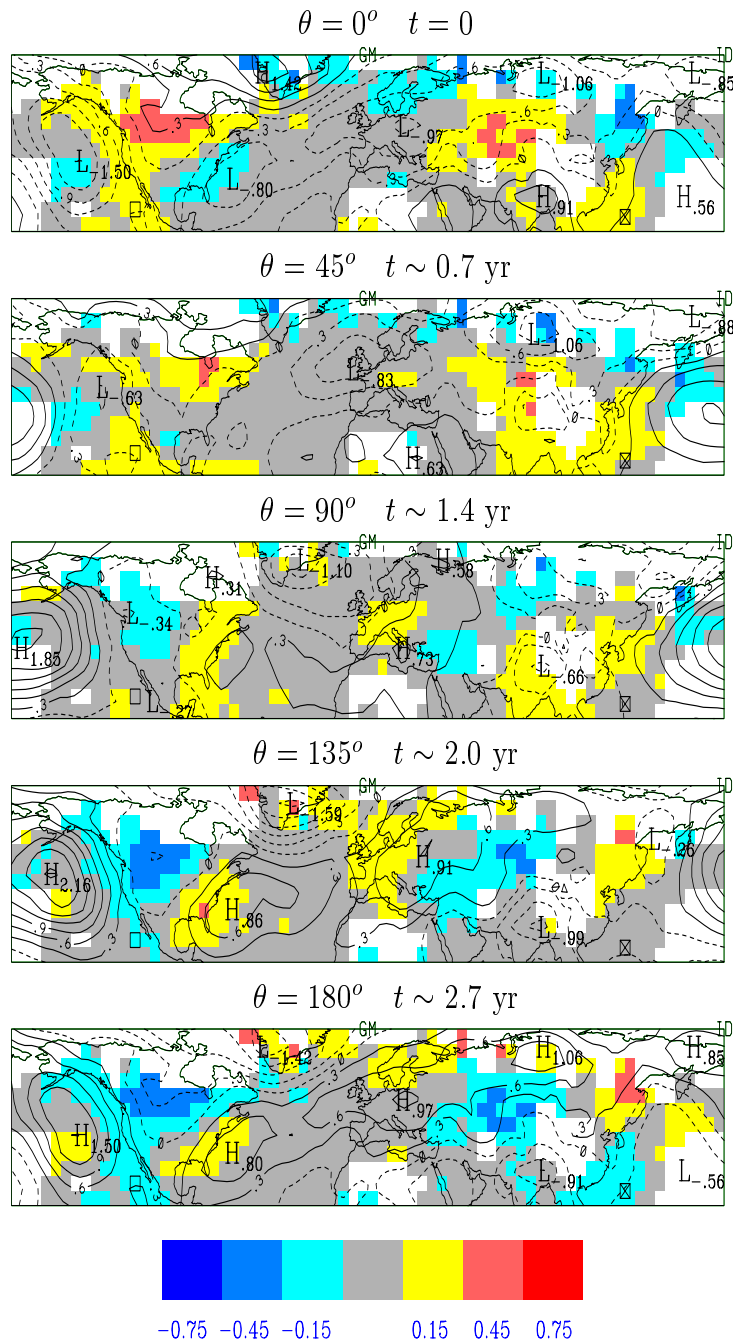


Figure 38: Canonical cold-season spatial pattern of low-frequency ENSO signal spanning one half of the average ~ 5.4 year cycle length. The initial snapshot corresponds to peak or near-peak (El Nino/low SO) ENSO conditions in the cycle.

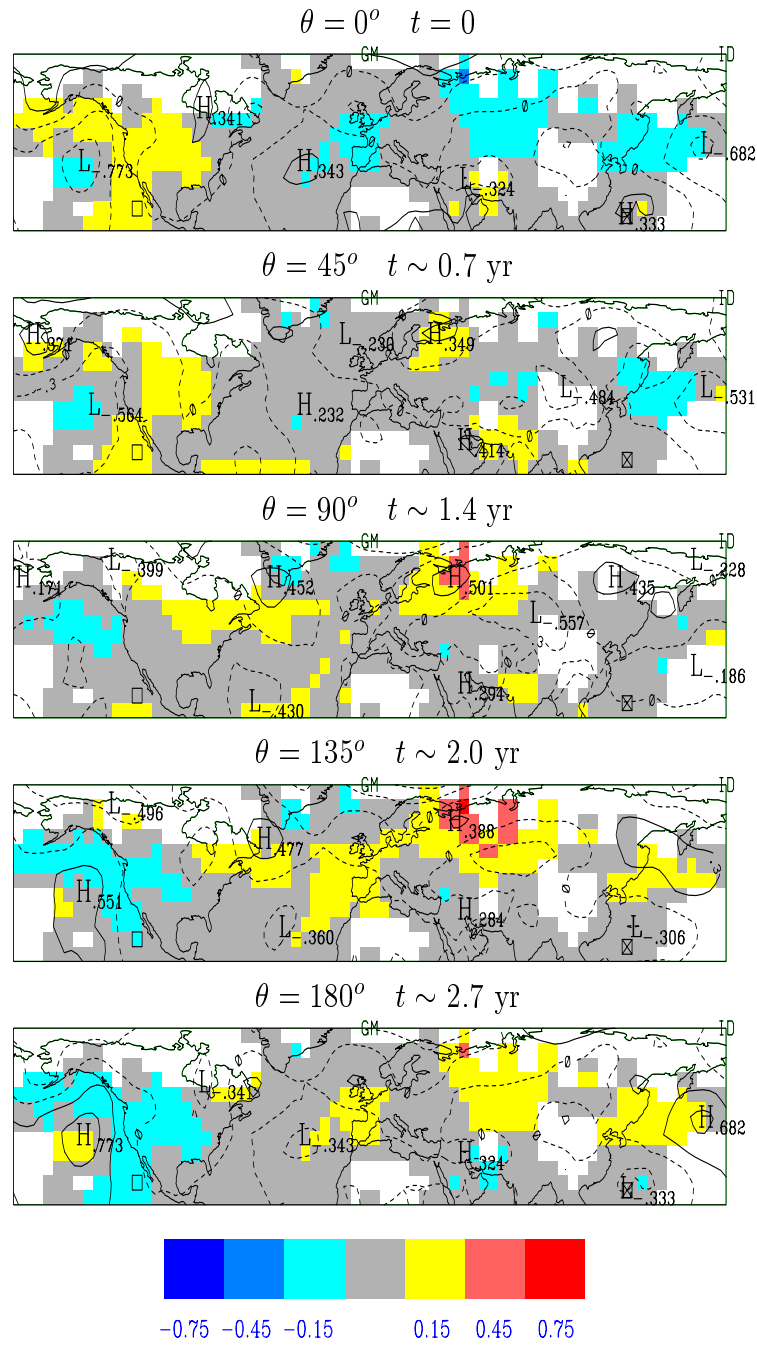


Figure 39: Canonical warm-season spatial pattern of low-frequency ENSO signal.

high-frequency “HF” band components isolated in the evolutive spectrum (see Figure 29). The reference signal is shown for a temperature gridpoint within the reach of the warm “El Nino”/cold “La Nina” tongue, and an SLP gridpoint within the limits of the Indonesian convective region strongly impacted by the southern oscillation (Figure 37). These two reference series are analogous to NINO3 and reverse SOI indices, and as expected are roughly in phase. Both HF and LF time-domain components exhibit highly significant spectral coherence within their respective frequency bands (95-99% confidence level) with both the standard SOI and NINO3 indices, providing independent evidence of a direct relationship with the ENSO signal. The spatial patterns for the LF component are shown for both cold (Figure 38) and warm (Figure 39) seasons. For simplicity, we show the spatial evolution for only one (the “low-frequency”) of the two dominant ENSO-related signals, and for a “composite” cycle obtained as the average pattern of evolution of the signal over the 95 year period. While certain features differ between the two signal components, we focus below only on those features that are shared by the low- and high-frequency patterns, and persist from cycle-to-cycle over the slowly evolving patterns of reconstruction. Low frequency and secular changes in the regional pattern of the large-scale ENSO signal may nonetheless exist [e.g., *Ropelewski and Halpert, 1987*] and should not be dismissed as stochastic event-to-event variations. Consistent with such non-stationarity in the patterns of ENSO, we note that the relative signature of “El Nino” vs “SO” characteristics is somewhat variable over time for the higher-frequency ENSO component, as evident in the high amplitude temperature fluctuations in the tropical eastern Pacific early in the century contrasting with relatively high-amplitude SLP fluctuations in the western tropical Pacific later (Figure 37). The nearly constant phase relationship (i.e., zero lag) between these SLP and temperature variations indicates a consistent “ENSO” signal. Studies of long-term proxy data suggests similar non-stationarity in the characteristics of ENSO over several centuries [*Cole et al. 1993; Linsley et al., 1994; Dunbar et al., 1994; Bradley et al., 1994*].

The initial stage shown for both the cold and warm season signal coincide with the peak low phase of the Southern Oscillation (maximum SLP anomaly in the Indonesian convective region, minimum SLP anomaly in the eastern Pacific) in phase with El Nino conditions (maximum positive SST anomalies along the eastern tropical and subtropical Pacific coast). Consistent with other studies [e.g., *Horel and*

Wallace, 1981] the low phase of the Southern Oscillation is observed to accompany notable cold-season circulation anomalies over the North Pacific and North America. The cold-season pattern over North America during this positive ENSO phase – e.g., roughly the first two stages shown – most closely resembles the Tropical/Northern Hemisphere (TNH) pattern which recent studies have shown to be a characteristic cold-season extratropical teleconnection of ENSO [*Livezey and Mo, 1987*], with patterns resembling the NAO [e.g., *Rogers, 1984*] and Western Pacific Oscillation (WPO) somewhat evident. There is a predominant tendency for hemisphere-wide warmth at this stage, although cooling is found in certain areas where cold advection is suggested or, in the case of Greenland, cooling under a cold-season high pressure region suggestive of enhanced radiational cooling. As the cycle progresses, by the 3rd stage shown (half way between low/high SO and El Nino/La Nina conditions), the TNH pattern over North America has broken down (although a considerable low pressure anomaly remains over the North Pacific) and temperature anomalies are generally weak. The cycle subsequently progresses to the reverse of the initial phase, associated with high SO, La Nina, a reverse TNH pattern, and predominant coolness over the hemisphere.

The SST anomaly patterns are consistent between, and quite persistent through the warm season, but tropical and extratropical circulation anomalies (including the east-west SLP gradients in the tropical Pacific) are considerably weaker. Accordingly, land surface temperature anomalies typically are lower amplitude. In places (e.g., central Asia) temperature anomalies in the distinct seasons are of opposite sign due to the seasonal specificity of inferred circulation anomalies. The seasonal persistence of the signal thus appears to arise largely from the year-round persistence of tropical SST anomalies during the evolution of the signal, while atmospheric circulation anomalies are more seasonally variable.

Quasibiennial Signal

The joint-mode analysis confirms the association of the large-scale surface quasibiennial signal (Figures 40, 41) with a distinct NAO SLP pattern as in *Trenberth and Shin [1984]*. Hemisphere-wide teleconnections are nonetheless evident. The time-domain signal (Figure 40 – performed using the evolutive reconstruction procedure with a 20 year window) exhibits considerable amplitude modulation on decadal timescales, which may indicate a coupling with other lower-frequency variability

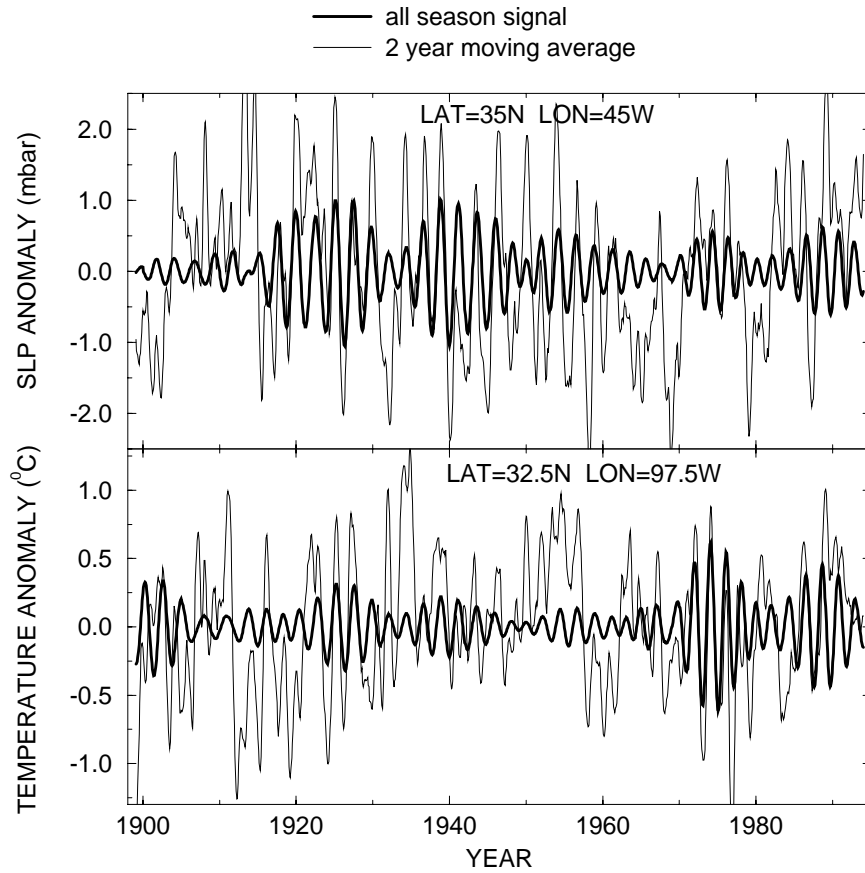


Figure 40: Time reconstruction of ~ 2.1 - 2.2 year quasibiennial signal (all months) for (i) reference SLP gridpoint in central subtropical North Atlantic and (ii) reference temperature gridpoint in western Soviet Union. [From Mann and Park (1996b).]

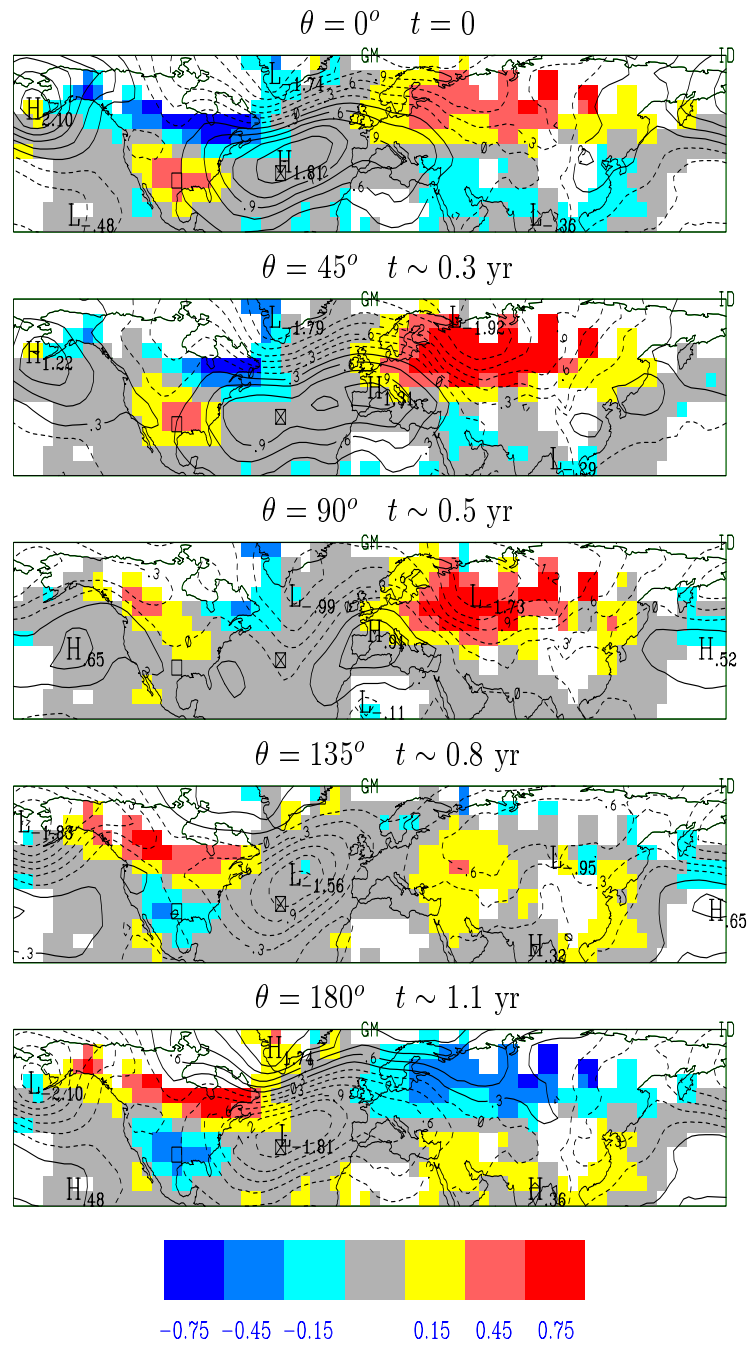


Figure 41: Canonical cold-season spatial pattern of quasibiennial signal, spanning one half of the average ~ 2.2 year cycle length. The initial snapshot corresponds to the peak positive NAO pattern over the North Atlantic.

discussed earlier. This signal is also observed to be highly phase-coherent with no phase modulation, which, as its period is not an integral multiple of the annual cycle, indicates weak if any phase-locking to the annual cycle. Nonetheless, the signal features are most distinct during the cold-season (Figure 41). The phase shown in the initial snapshot, associated with the positive NAO pattern over the Atlantic, also shows a “lopsided” dipole SLP pattern over the Pacific. The temperature pattern follows expected patterns of sensible heat transport with warm (cold) anomalies associated with regions of implied southerly (northerly) advection and, over extratropical Eurasia, enhanced warmth due to strengthened westerlies and an associated moderated winter climate. Similar relationships between circulation and surface temperature anomalies are found as the signal evolves over a typical cycle. The lack of large temperature anomalies in the eastern Pacific or any sizable east-west SLP gradients in the tropical Pacific during the evolution of the signal would seem to cast doubt on a direct connection with ENSO. However, we *do*, somewhat paradoxically, find significant spectral coherences between the quasibiennial signal and quasibiennial-band fluctuations in ENSO [that is, both the SOI and NINO3 – see also *Trenberth and Shin*, 1984; *Barnston et al.*, 1991]. This relationship could thus reflect a quasibiennial extratropical forcing of weaker fluctuations in ENSO. This inference is not dissimilar from that of *Barnett* [1991] who noted that QB-band variations, although apparently somewhat related to ENSO, had a far weaker loading in the tropical Pacific than lower-frequency ENSO variability. Consistent with *Barnett* [1991] and *Trenberth and Shin* [1984], no significant relationship is observed with the quasibiennial oscillation in equatorial stratospheric wind data available for the past few decades [see *Naujokat*, 1986], with spectral coherences in the quasibiennial band that barely breach the median confidence level for significance.

Summary

MTM-SVD analysis of a joint 20-th century temperature-anomaly/sea-level pressure data set, restricted to the Northern Hemisphere, lends strong support to the existence of the oscillatory climate signals, identified in the temperature-anomaly data set alone. The interdecadal 16-18 year climate signal appears consistent with a gyre spinup and mid-latitude ocean-atmosphere interaction, a mechanism predicted in a recent coupled-ocean atmosphere simulation. Weaker quasidecadal (10-11 year timescale), largely cold-season oscillatory behavior is more closely tied to the North

Atlantic and may involve analogous mechanisms. Rather than modulating a simple NAO pattern, the decadal oscillation is associated as well with a lateral migration of pressure and temperature anomalies, behavior that would be missed in a simple time series of a fixed NAO index. Interannual variability is examined with an “evolutionary” generalization of our procedure to captures the time-evolving frequency and amplitude characteristics of the associated climate signal. Variability exhibiting the characteristic climatic patterns of the global El Niño/Southern Oscillation (ENSO) phenomenon is described by two largely distinct frequency bands within the broader 3-7 year ENSO band. The drifting central frequencies of these two dominant bands is suggestive of non-stationary behavior in ENSO. A quasi-biennial signal exhibits a gradual trend towards increasing frequency.

4.3 Long-term Multiproxy Temperature Data

To more confidently identify spatiotemporal climate signals at interdecadal and longer timescales, we make use of a small (35), but globally distributed, set of high-resolution temperature proxy reconstructions (Figure 42) available for most of past half millennium. These data include tropical [e.g., *Thompson, 1992*] and extratropical ice melt measurements [*Bradley and Jones, 1993*], tropical corals [*Cole et al, 1993; Dunbar et al, 1994*] dendroclimatic reconstructions [*Jacoby and D’arrigo, 1989; Bradley and Jones, 1993*] and a handful of very long historical sources [*Bradley and Jones, 1993*]. Although extratropical records primarily reflect warm season climatic variations [see *Bradley and Jones, 1993*], the signals of interest (see e.g. section 4.2, Figure 28) are believed to be seasonally robust. The characteristics of the different proxy records employed in the network are described in Table 5.

To trade off the limitations of temporal resolution and duration (see Table 5) with that of spatial coverage, it was useful to analyze four subsets of the data independently: (A) 27 shorter records (1730-1969) with annual resolution, (B) 21 medium duration (1615-1969 AD) records with annual resolution (C) 35 shorter (1730-1960 AD) records with decadal resolution and (D) 12 longer (1400-1960 AD) records with decadal resolution.

LFV spectra

First, we compared the proxy network against instrumental data in sampling and detecting the same large-scale temperature signals. We performed parallel analyses

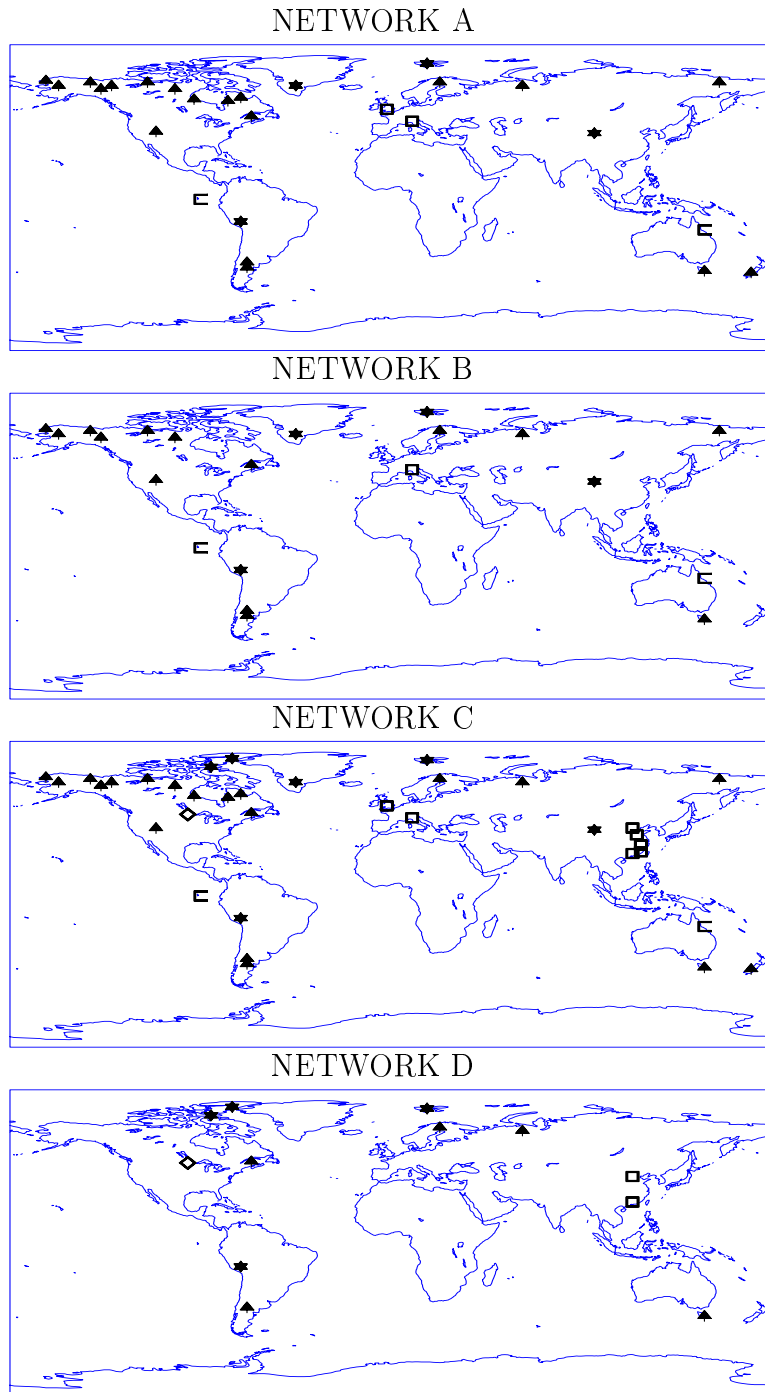


Figure 42: Distribution of proxy temperature reconstructions used in the present study for experiments (a), (b), (c), and (d). Squares denote historical or instrumental records, Umbrella or "Tree" symbols denote dendroclimatic reconstructions, "C" symbols indicate corals, and diamond indicates varved lake sediment record. [Reprinted with permission from Mann et al (1995b). *Nature (London)*, 378, 266-270. Copyright ©1995 Macmillan Journals Limited.]

Record	Location	Begin	End	Resolution	Reference
1. Northern treeline (tree ring)	69N, 197E	1515	1982	annual	Jacoby and D'Arrigo
2. Northern treeline (tree ring)	66N, 203E	1515	1982	annual	Jacoby and D'Arrigo
3. Northern treeline (tree ring)	68N, 218E	1515	1982	annual	Jacoby and D'Arrigo
4. Northern treeline (tree ring)	64N, 223E	1515	1982	annual	Jacoby and D'Arrigo
5. Northern treeline (tree ring)	66N, 228E	1515	1982	annual	Jacoby and D'Arrigo
6. Northern treeline (tree ring)	68N, 245E	1515	1982	annual	Jacoby and D'Arrigo
7. Northern treeline (tree ring)	64N, 258E	1515	1982	annual	Jacoby and D'Arrigo
8. Northern treeline (tree ring)	58N, 267E	1515	1982	annual	Jacoby and D'Arrigo
9. Northern treeline (tree ring)	57N, 283E	1515	1982	annual	Jacoby and D'Arrigo
10. Northern treeline (tree ring)	59N, 289E	1515	1982	annual	Jacoby and D'Arrigo
11. Northern treeline (tree ring)	48N, 294E	1515	1982	annual	Jacoby and D'Arrigo
12. Western U.S. (tree ring)	42N, 249E	1600	1982	annual	Bradley and Jones
13. Northern Patagonia (tree ring)	38S, 292E	869	1983	annual	Bradley and Jones
14. Central Patagonia (tree ring)	41S, 292E	1500	1974	annual	Bradley and Jones
15. N. Scandinavia (tree ring)	68N, 23E	500	1980	annual	Bradley and Jones
16. Northern Urals (tree ring)	66N, 62E	1400	1969	annual	Bradley and Jones
17. Upper Kolyma River (tree ring)	68N, 155E	1550	1977	annual	(Earle, pers. comm.)
18. Tasmania (tree ring)	43S, 148E	900	1989	annual	Bradley and Jones
19. South New Zealand (tree ring)	44S, 170E	1730	1978	annual	Bradley and Jones
20. Agassiz (ice melt)	81N, 280E	466	1966	5 yr	Bradley and Jones
21. Southern Greenland (ice melt)	66N, 315E	1545	1988	annual	Bradley and Jones
22. Devon (ice melt)	75N, 275E	1400	1970	5 yr	Bradley and Jones
23. Svalbard (ice melt)	79N, 17E	1400	1985	annual	Bradley and Jones
24. Quelccaya (ice core, O ¹⁸)	14S, 289E	470	1984	annual	Thompson
25. Dunde (ice core, O ¹⁸)	38N, 96E	1606	1985	annual	Thompson
26. Central England (instrumental)	52N, 358 E	1730	1987	annual	Bradley and Jones
27. Central Europe (historical)	45N, 10E	1550	1979	annual	Bradley and Jones
28. Eastern China (historical)	24N, 114E	1380	1980	decadal	Bradley and Jones
29. Northern China (historical)	39N, 118E	1380	1980	decadal	Bradley and Jones
30. Yellow River (historical)	35N, 116E	1470	1980	decadal	Bradley and Jones
31. S.E. China (historical)	25N, 118E	1470	1980	decadal	Bradley and Jones
32. Yangtze River (historical)	29N, 118E	1470	1980	decadal	Bradley and Jones
33. Galapagos (coral, O ¹⁸)	1S, 270E	1607	1981	annual	Dunbar et al
34. Great Barrier Reef (coral)	19S, 148E	1615	1982	annual	Lough (pers. comm.)
35. Minnesota (lake varve)	48N, 259E	980	1960	decadal	Bradley and Jones

Table 5: Proxy Data Records Used: Description/Type of Record, Location (Latitude, Longitude), Beginning and Ending Year, Time Resolution, and Reference.

of data during the last century based on (i) the global distribution of instrumental temperature data from 1890-1989 analyzed in section 4.1, (ii) proxy group A over the abbreviated interval 1890-1969, and (iii) a sparse sub-sampling of the instrumental data of (i) chosen to mimic the spatial distribution and seasonal sampling and 1890-1969 time interval of the proxy data set A. A paucity of high-latitude instrumental sites impedes a perfect spatial match between data sets (ii) and (iii). The associated LFV spectra are shown in Figure 43. All four data sets exhibit a statistically significant 16-18 year timescale interdecadal signal ($f \approx 0.06$ cyc/yr) significant at the 95% confidence level. The quasidecadal signal of sections 4.1 and 4.2 ($f \approx 0.09$ cyc/yr) is at least marginally significant (>90% level) in each of the datasets. Though the quasidecadal signal is cold-season dominant in the extratropical Northern hemisphere (section 4.2, “Quasidecadal Signal”), the global sampling of the proxy network probably facilitates its detection with predominantly warm season proxy indicators. Within the secular regime, both the primary and secondary mode are significant, as in the observational temperature and joint temperature/SLP analyses of sections 4.1 and 4.2 respectively. This exercise indicates that the proxy data network appears to be capable of capturing large-scale climatic processes evident in recent instrumental-based analyses, though with inexact calibration.

Figure 44 shows the LFV spectra applied to the full-length multiproxy datasets. The LFV spectra for data groups A–D yield statistically significant peaks on 15-35 year interdecadal and 50-130 year multidecadal/century timescales. We isolate a quarter-millennial (~ 240 year) oscillation in data group D where longer-period variability can be resolved from a secular trend. This identification is tentative, however, as less than three “cycles” are present, and the signal can not be independently confirmed from the other data subsets. Only groups A and B can fully resolve the bidecadal signals, as the Nyquist frequency for 10-year sampling corresponds to a 20-year period. Higher frequency signals (e.g., ENSO band) observed in the A and B analyses are discussed elsewhere *Bradley et al* [1994]. Comparison of the spatial patterns of the interdecadal and century-scale peaks reveal clear distinctions that are consistent among the data groups. We have grouped peaks of correlated variance into interdecadal and century-scale bands. The variation of these peaks among LFV spectra on different time intervals suggests signals with frequencies that drift over time.

The time-evolving nature of the amplitude and frequency of the interdecadal

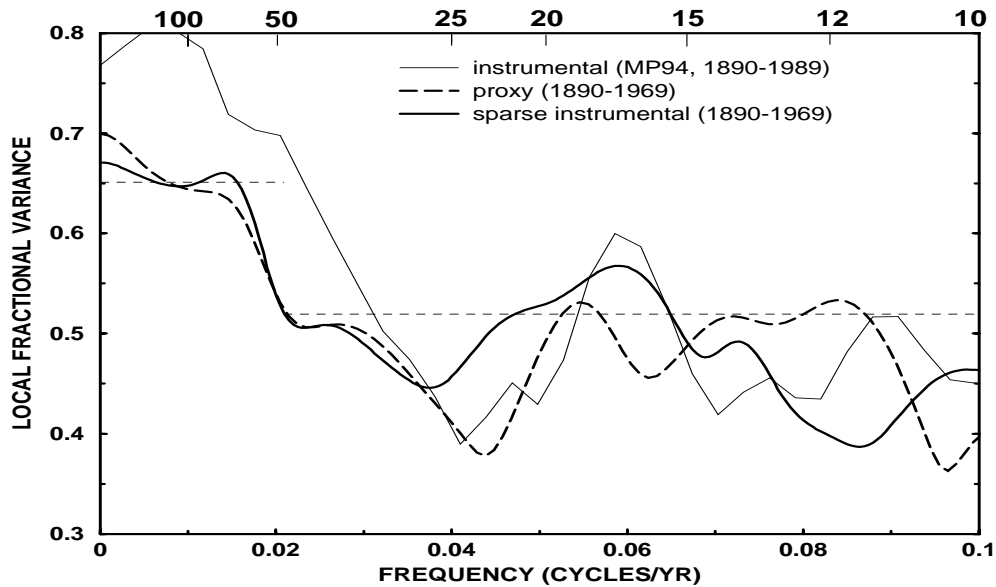


Figure 43: LfV spectrum for (i) instrumental global temperature data of section 4.1 (ii) proxy data set (A), (iii) instrumental data sampled similarly to the proxy network, as described in the text. The local fractional variance scale shown applies strictly only to (i), with the scales for (ii) and (iii) normalized (by factors 0.95 and 0.85 respectively) so that the quantiles of the null distribution and significance levels (which vary with the number of effective spatial degrees of freedom) approximately align at the 95% level (shown by horizontal dashed lines). Confidence limits are higher within the secular band corresponding to variability longer than about 50 years period. [Reprinted with permission from Mann et al (1995b). *Nature (London)*, 378, 266-270. Copyright ©1995 Macmillan Journals Limited.]

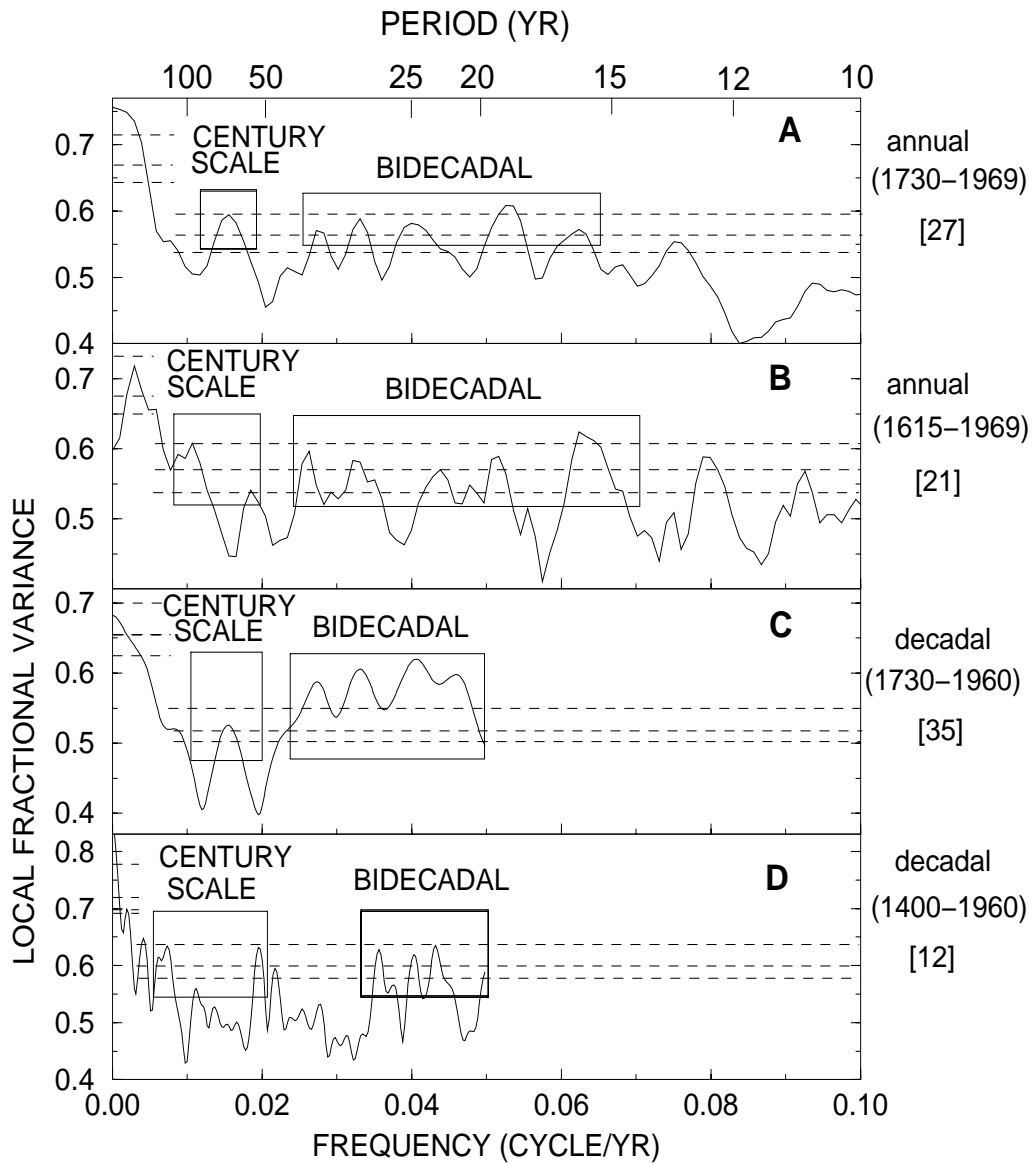


Figure 44: LFV spectra for each of the experiments “A-D”. Horizontal dashed lines indicate 90%,95%, and 99% confidence levels for significance. Significant interdecadal and century-scale peaks are indicated by surrounding boxes. [Reprinted with permission from Mann et al (1995b). *Nature (London)*, 378, 266-270. Copyright ©1995 Macmillan Journals Limited.]

and century-scale signals is better examined with the evolutive MTM-SVD analysis. Window durations are chosen to be long enough to allow reasonable frequency resolution, but short enough to provide insight into the evolving character of signals. The short duration, combined with decadal resolution, precludes a meaningful evolutive analysis for data group “C”. The evolutive analyses (Figure 45) demonstrate that interdecadal oscillations, centered near 20-25 year periodicity, were weakly evident before 1800. The oscillations subsequently strengthen in significance and gradually increase in frequency to roughly 16-18 year periodicity in the final window (1869-1969), in agreement with the timescale of the interdecadal oscillation described in sections 4.1 and 4.2. Time windows that resolve century-scale variations (200 year width) can be employed in Experiment D. Before 1650, a coherent signal with roughly 50 year timescale appears intermittently. After 1650 this oscillation strengthens in its significance and drifts to a 60-70 year periodicity. After 1800, these “century-scale” oscillations appear to drift to slightly longer period, becoming indistinguishable from secular timescale variability within the confines of a 200 year moving window. Note also that the improved frequency resolution of experiment D allows for a clearer separation of the interdecadal and century-scale variability than do experiments A or B.

Signal Reconstructions

Figure 46 shows the spatial patterns of the interdecadal and century-scale signals. In the spatial reconstructions, sources of systematic bias in the temperature reconstructions may lead to unreliable phase and amplitude at isolated sites. The few records that were not originally calibrated in temperature ($^{\circ}\text{C}$) units, are calibrated using the variances of nearby instrumental gridpoint temperature data [*Briffa and Jones, 1992*] during the past century. Calibration of proxy data at longer periods, and various corrections that are made to proxy records (e.g., subtraction of individual long-term growth trends for dendroclimatic records) are potential sources of bias. Thus, the general regional trends that are evident in these patterns, rather than the precise response at particular sites, are most meaningful.

The interdecadal signal (Figure 46, top) exhibits variability in the tropics and subtropics that is largely in-phase. Mid-latitude variations are of similar magnitude, but phase relationships are more variable, consistent with the signature of extratropical teleconnection patterns. While such patterns can be resolved by our

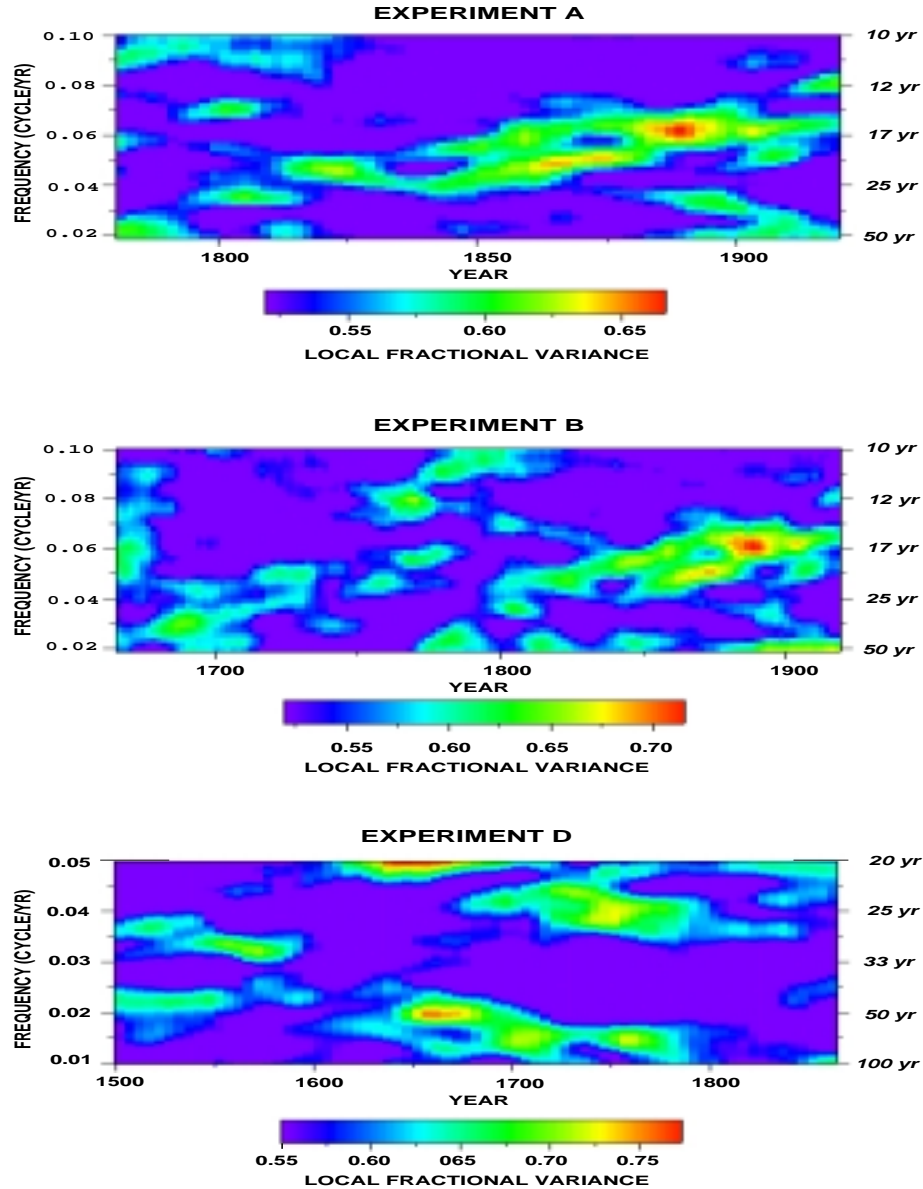


Figure 45: Evolutive LFV spectra for (top) experiment “A” using a window $L = 100$ (local fractional variance is described by a colour scale, with significance levels $90\% = 0.55$, $95\% = 0.565$, $99\% = 0.60$. Greyscale convention chosen so that any features clearly visible above the background are significant well above the 95% level.), (middle) LFV spectrum for experiment B using a 100 year moving window (the significance levels are the same as experiment A), and (bottom) experiment D using a 200 year moving window. Significance levels correspond to 0.58 (90%), 0.60 (95%) and 0.64 (99%) in the latter case. [Reprinted with permission from Mann et al (1995b). *Nature (London)*, 378, 266-270. Copyright ©1995 Macmillan Journals Limited.]

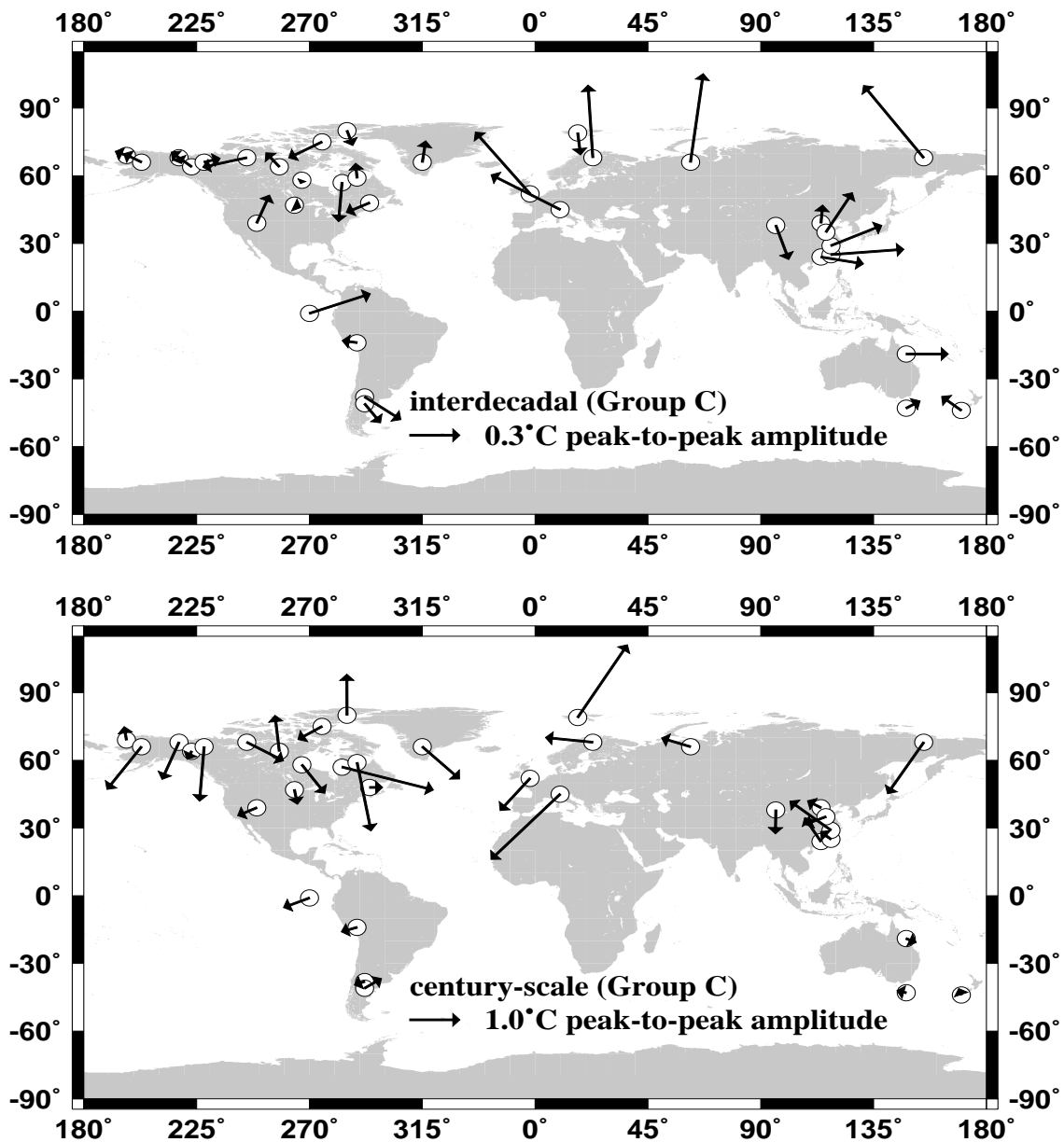


Figure 46: (top) Spatial pattern of interdecadal oscillation based on the signal reconstruction for the ~ 24 year period peak in experiment “C” (which provides the greatest spatial coverage). Conventions similar to that introduced in Figure 22. If we define zero phase as when the tropics are generally warmest, peak warmth in northern Eurasia occurs 90° (or, roughly 6 years) later. Amplitude scale is set so that the largest arrow corresponds to the regional maximum amplitude of the oscillation of $\sim 0.6^\circ\text{C}$ peak-to-peak. (bottom) The spatial pattern for century-scale signal oscillation is reconstructed based on the 65 year period variance peak of experiment C. Pattern maximum is a $\sim 2^\circ\text{C}$ peak-to-peak oscillation (e.g., central Europe). [Reprinted with permission from Mann et al (1995b). *Nature (London)*, 378, 266-270. Copyright ©1995 Macmillan Journals Limited.]

data network only in part, the alternating pattern of phase from Greenland, to eastern and then western mid-latitude North America (with a nodal point in central North America) is consistent with the alternating warm and cold advection of the three-lobed “Pacific North American” (PNA) pressure anomaly pattern (although the vector directions for certain sites are inconsistent with the general pattern). This PNA pattern was associated with the interdecadal signal in the instrumental climate record. Other regional proxy records [*Slowey and Crowley, 1995*] and analyses of continental U.S. drought reconstructions [*Rajagopalan et al, 1996*] confirm a similar pattern of interdecadal variability in the PNA pattern. While some regional differences in relative amplitude and phase are noted with the instrumental signal (compare Figure 24), the larger-scale features of nearly in-phase tropical/subtropical variability consistent with ENSO and an extratropical PNA-like pattern are clearly evident in the proxy climate signal. The frequency modulation of the interdecadal signal between ~ 15 and ~ 35 year period ranges (with a recent trend towards the higher frequencies) presents a complication for the interpretation of the extratropical coupled mode of LB94 discussed in section 4.2 (“Interdecadal Signal”). The oscillatory timescale in the LB94 mechanism is specified by gyre spinup dynamics and should not change over time. Nor should the interdecadal mechanism of *Gu and Philander* [1997] which involves transit times of water mass subduction. In contrast, frequency modulation is more consistent with the behavior of a system with changing control parameters, or a non-linear system [e.g., *Lorenz, 1990; Tziperman et al, 1994; Jin et al, 1994*]. The latter connection would favor the notion that the observed interdecadal variability is associated with intrinsic low-frequency behavior of the tropical ocean-atmosphere [e.g. *Graham, 1994*]. Thus, while the interpretation of the underlying dynamics is not obvious, the proxy data analysis does provide evidence for long-term interdecadal oscillations, and at least some suggestion of a connection with ENSO.

The spatial pattern of the “century-scale” 50-70 year timescale signal (Figure 46-bottom) exhibits high-amplitude variability largely confined to the North Atlantic and Arctic, out-of-phase with weaker variability in the Pacific basin. These features recall the pattern of the single multidecadal or century-scale “oscillation” described in sections 4.1 and 4.2., although it should be noted that arbitrary phase relationships could not be determined for the century-scale signal in the instrumental record as was confined to the secular trend frequency band. The longer history provided by

the proxy data, however, allows for the recognition of a true oscillatory process on multidecadal or century timescales, with arbitrary spatial phase relationships. Aside from the Svalbard site in the boreal Atlantic, there is a tendency towards opposing, though not *opposite*, phase anomalies (ie., $\approx 45^\circ$ - 135° phase difference) between the eastern and western margins of the North Atlantic (note that such variable phase relationships could not be captured in the short instrumental record because the multidecadal oscillation was confined to the secular frequency regime). Such a phase pattern could indicate a combination of in-phase and out-of-phase components in the two regions. An out-of-phase component could arise from differential temperature advection on either side of an alternating center of low and high pressure over the North Atlantic. Changes in northward oceanic heat transport would generate an in-phase component of basinwide warming and cooling. The combination of these effects is consistent with the coupled ocean-atmosphere model mechanisms isolated by DEL93 and discussed previously in section 4.2, in which multidecadal (with a *slightly shorter* 40-60 year periodicity) variations in sea-level pressure over the North Atlantic coincide with oscillations in the thermohaline circulation. The two patterns differ somewhat however in that the empirical phase lag between the in-phase and out-of-phase variations across the North Atlantic suggest a temporal lag between maxima in meridional overturning heat transport to high-latitudes and the most pronounced atmospheric circulation response. The simulations of DEL93 show these two responses to be more coincident. Similar empirical analyses with expanded proxy networks may better constrain the spatial relationships between the modeled and observed oscillatory signals.

Summary

MTM-SVD analysis of a globally-distributed set of temperature proxy records, of several centuries duration, strengthens evidence for persistent 15-35 year period “interdecadal” and 50-150 year “century-scale” climatic oscillations, and reveals both the spatial patterns and temporal histories of these signals. The time-evolving amplitude and frequency of quasiperiodic signals can be examined with an “evolutive” analysis, in which the SVD analysis is applied in a moving window through the data series. The interdecadal oscillation, centered near 20–25 year periodicity, is weakly evident before 1800, and subsequently strengthens in significance and drifts to roughly 16–18 year period in 20th century. The century-scale mode exhibits high-

amplitude variability largely confined to the North Atlantic and Arctic, out-of-phase with weaker variability in the Pacific basin. This behavior resembles the pattern of the single quasi-secular “oscillation” detected in gridded surface temperature and pressure data of the last 100 years.

4.4 Seasonal Cycle: Observations vs CO₂-forced Model Simulations

Thomson [1995] showed that shifts in the phase of the annual cycle in temperature during the 20th century are correlated with atmospheric CO₂ concentrations, and argued for an anthropogenic cause. Similar phase changes have been observed in the seasonal cycle of temperature in particular regions [Davis, 1972; Thompson, 1995] as well as shifts in the seasonality of precipitation [Bradley, 1976; Rajagopalan and Lall, 1995], streamflow [Lins and Michaels, 1994; Dettinger and Cayan, 1995], and Southern Hemisphere winds and sea-level pressure [Hurrell and Van Loon, 1994]. Potential physical connections with greenhouse forcing have been suggested [Lins and Michaels, 1994], complementing the statistical correlation found by Thomson [1995]. If observed changes in seasonality are consistent with an enhanced greenhouse effect, the observed trends in the seasonal cycle should resemble the simulated response of present-generation climate models to enhanced greenhouse conditions. Here, we review the comparison by Mann *et al* [1996a] of the seasonal cycle of temperature in the northern hemisphere with those of simulations of 1) the Geophysical Fluid Dynamics Lab (GFDL) coupled ocean-atmosphere model [Manabe *et al*, 1991], and 2) the NCAR Community Climate Model (CCM1) general circulation/slab ocean model [Oglesby and Saltzman, 1992].

Northern hemisphere average trends

We approximate the seasonal cycle in temperature by its fundamental annual component $A(t) \cos(2\pi t + \theta(t))$, where t is time in years and the phase $\theta(t)$ and amplitude $A(t)$ can vary with time. This simple statistical model is motivated by the fact that surface temperature seasonality is determined, within a phase lag, by the yearly cycle of insolation at the top of the atmosphere in most locations. The harmonics of the annual cycle are important, however, in the tropics and in the polar latitudes of the southern hemisphere [see e.g., Trenberth, 1983] and provide essential information about relationships with specific seasons (e.g., the onset of “spring”

[*Davis, 1972*]). The departures of certain seasonal features (e.g., convective mixing in the high-latitude ocean, the termination of the monsoons, or sea ice and snow-cover processes) from a simple annual cycle suggest that our analysis provides only a first-order estimate of more general changes in the structure of the seasonal cycle.

Using the estimated Northern Hemisphere (NH) average monthly temperature series of Jones et al [“J&W”, 1986 – updated in *Jones, 1994*] with seasonal climatology intact, we estimated the variation in $\phi(t)$ and $A(t)$ of the annual cycle over the interval 1854-1990 through complex demodulation (Figure 47).

We used three Slepian data tapers and a 10 year moving interval or “projection filter” to obtain low-variance estimates of the trends in $A(t)$ and $\phi(t)$. Through this method, phase shifts of less than one day can be resolved in monthly data [see *Thomson, 1995*]. The calculated trends were robust as we varied the length of the moving window from 5 to 20 years. The highly variable spatial sampling (growing from $\sim 20\%$ to near-complete areal coverage during the interval under examination) may bias estimates of small changes in hemisphere-averaged quantities. To test for such bias, we analyzed alternative “frozen grid” estimates of the NH average series using gridded land air and sea surface temperature data [*Jones and Briffa, 1992*]. These series were calculated from both 1) a “sparse” sampling of all nearly-continuous gridpoint series from 1890 to 1989 [see e.g., *Mann and Park, 1994*] providing 33% coverage, and 2) a “dense” sampling from 1899 to 1989 providing 53% areal coverage (shown in Figure 48). The gross trends in the annual cycle phase and amplitude (Figure 47) appear insensitive to the sampling of large-scale averages (see Table 6), though an unavoidable bias due to data sparseness at latitudes poleward of 70°N may exist. The baseline annual cycle varies with the mixture of land, ocean, and high-latitude grid points due to important regional variations in phase and amplitude.

Trends towards an advanced phase (i.e., earlier seasonal transitions) are significant at better than 2.5σ in each of the three data schemes (Table 6) based on jackknife uncertainties, taking serial correlation into account. Such significance does not alone indicate a causal connection with greenhouse-related warming, as it could result, for example, from the enhanced century-scale *natural* variability that is evident in both observations [*Mann and Park, 1994; Schlesinger and Ramankutty, 1994; Mann et al 1995b*] and modeling studies [*Delworth et al, 1994*]. If an opposing trend towards delayed phase due to orbital precession is adopted as a null hypothesis

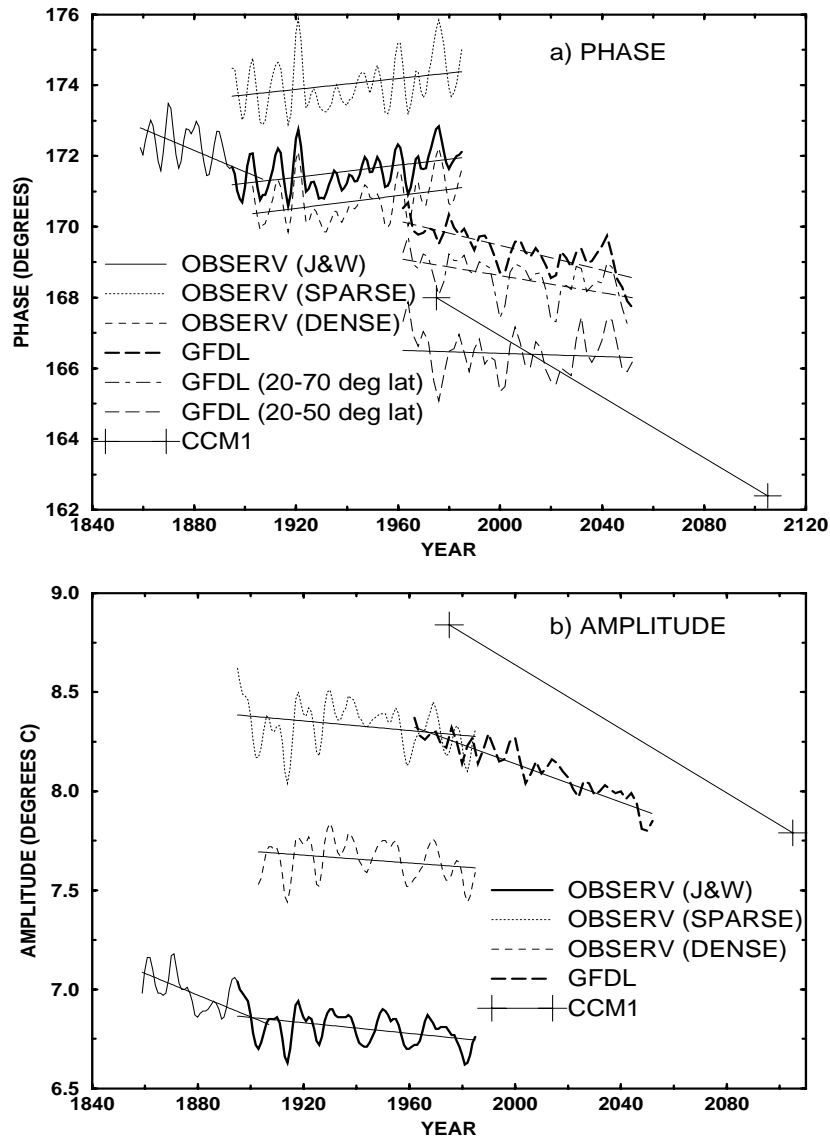


Figure 47: (a) Phase of annual cycle in Northern Hemisphere average temperature for observations and model simulations. Best-fit linear trends (Table 6) are shown. For the observational data, results for both the “J&W” expanding grid, and sparse and dense “frozen-grid” estimates (see text) are indicated. For the longer J&W series, a break in slope near 1900, marks a transition from decreasing to increasing phase (latter portion shown with thicker curve). Time axis for the model defined by the actual year corresponding to the initial prescribed CO_2 level. For the CCM1 (equilibrium) experiment, only the net change has meaning. For graphical purposes, a timescale is prescribed by assuming the same 1 %/year increase as in the GFDL experiment. (b) Amplitude of the annual cycle. Decreasing trends of varying magnitude are found for both model and observed data. Best-fit linear trends are shown (Table 6), with a break in slope again evident in the observations between 1890 and 1900. [From Mann and Park (1996a).]

Table 6: Linear Trends in Phase and Amplitude of Northern Hemisphere Average Annual Temperature Cycle for Model and Observations. [From Mann and Park (1996a).]

SERIES	$\Delta\phi(^{\circ})$	signif.	ΔA	signif.
OBSERV (J&W: 1854-1904)	-1.4	$> 5.5\sigma$	-0.55	$> 6\sigma$
OBSERV (J&W: 1899-1989)	0.79	$> 4.5\sigma$	-0.13	$> 4\sigma$
OBSERV (SPARSE)	0.71	$> 3\sigma$	-0.12	$> 3\sigma$
OBSERV (DENSE)	0.83	$> 3.5\sigma$	-0.10	$> 2.5\sigma$
GFDL (CO ₂ increase)	-1.7	$> 7.5\sigma$	-0.48	$> 16\sigma$
" (20-70 ^o)	-1.2	$> 4\sigma$	-0.50	$> 10\sigma$
" (20-50 ^o)	-0.2	$< \sigma$	-0.04	$< \sigma$
GFDL (control)	0.5	$> 1.5\sigma$	+0.02	$< \sigma$
CCM1 (460ppm-330ppm)	-5.6		-1.05	

[*Thomson, 1995*], the above trends become more significant.

A significant decreasing trend in $A(t)$ is also found for each data-weighting scheme (Figure 47, bottom). A break in the slope between 1884 and 1895 is significant at the $p = 0.01$ level. Lean et al [1995] suggest an increasing trend in solar irradiance beginning in the early 20th century. This trend could counteract an even greater decrease in $A(t)$ that might arise from global warming and associated ice albedo feedback, potentially explaining the break in slope. A connection between decreasing $A(t)$ and decreased winter ice cover is suggested by the model responses to greenhouse forcing.

We analyzed for comparison both (i) the change in the CCM1 climatological annual cycle between 330 ppm and 460 ppm CO₂ level equilibrations [see *Oglesby and Saltzman, 1992; Marshall et al, 1995*] and (ii) 100-year simulations of the GFDL coupled model [e.g., *Manabe et al, 1991*] with (a) a gradual (1%/year) CO₂ increase and (b) with fixed present-day CO₂. Both models exhibit a significant annual cycle response to greenhouse forcing (Table 6). Decreased amplitude of the annual cycle under CO₂-enhanced conditions is consistent with the observations. The time axis for the transient GFDL model simulations should be interpreted quite loosely, as the imposed forcing in these simulations is highly idealized, and does not realistically mimic changes in observed greenhouse gas concentrations. The trend in phase for the models, however, is opposite to that observed, exhibiting a delay, rather than an advance, of the seasons. The magnitude and significance of the trends in the

enhanced-greenhouse GFDL simulation diminishes if high and low-latitude regions, poorly sampled by the observational data, are excluded (Figure 47, top), but no latitude band exhibits the phase *advance* found in the the observations. The control GFDL simulation, like the observations, exhibits a marginally significant advance in phase (Table 6), perhaps associated with organized century-scale variability [Delworth *et al*, 1994].

Spatial patterns

To reconstruct the spatial patterns of the climatological annual cycle, we used a multivariate generalization [Mann and Park, 1994; Mann *et al*, 1995ab] of the complex demodulation procedure used by Thomson [1995]. The climatological seasonal cycle in the control GFDL simulation resembles quite closely that for the “dense” observational temperature sampling (Figure 49). It should, however, be noted that this is partly due to seasonally-specific flux corrections that are imposed in the model on at the ocean surface [Manabe *et al*, 1991]. These climatological flux corrections, furthermore, may suppress the tendency for the annual cycle in the model to depart from its baseline state. The annual cycle over continents is delayed by ~ 1 month relative to the insolation cycle, due to the thermal capacity of land, continental snow cover, and other climatic factors – see Trenberth [1983] for an overview. The greater thermal capacity of the oceans leads to a greater delay (typically, 2 months) and a smaller annual cycle amplitude. Land areas strongly influenced by the oceans experience a more maritime annual cycle. Winter sea ice insulates the ocean surface from the mixed layer, exposing some oceanic regions to cold continental outbreaks. This can lead to a more “continental” seasonal cycle in the high-latitude oceans. Changes in the annual cycle could thus arise from many influences. The climatological annual cycle of the CCM1 (not shown) reproduces the observations less well. CCM1 predicts an oceanic phase lag that is typically ~ 1 month too large because the slab ocean is a poor approximation to the true mixed layer.

To determine the spatial pattern of annual cycle trends in the GFDL simulations, we used the multivariate procedure described above to isolate the average annual cycle in successive 10-year intervals. We regressed the long-term trends in $\theta(t)$ and $A(t)$ on a gridpoint-by-gridpoint basis, calculating jackknife uncertainties from the decadal averages. The spatial pattern of the CCM1 response (not shown) was estimated by differencing the 460 ppm and 330 ppm equilibrium climatologies.

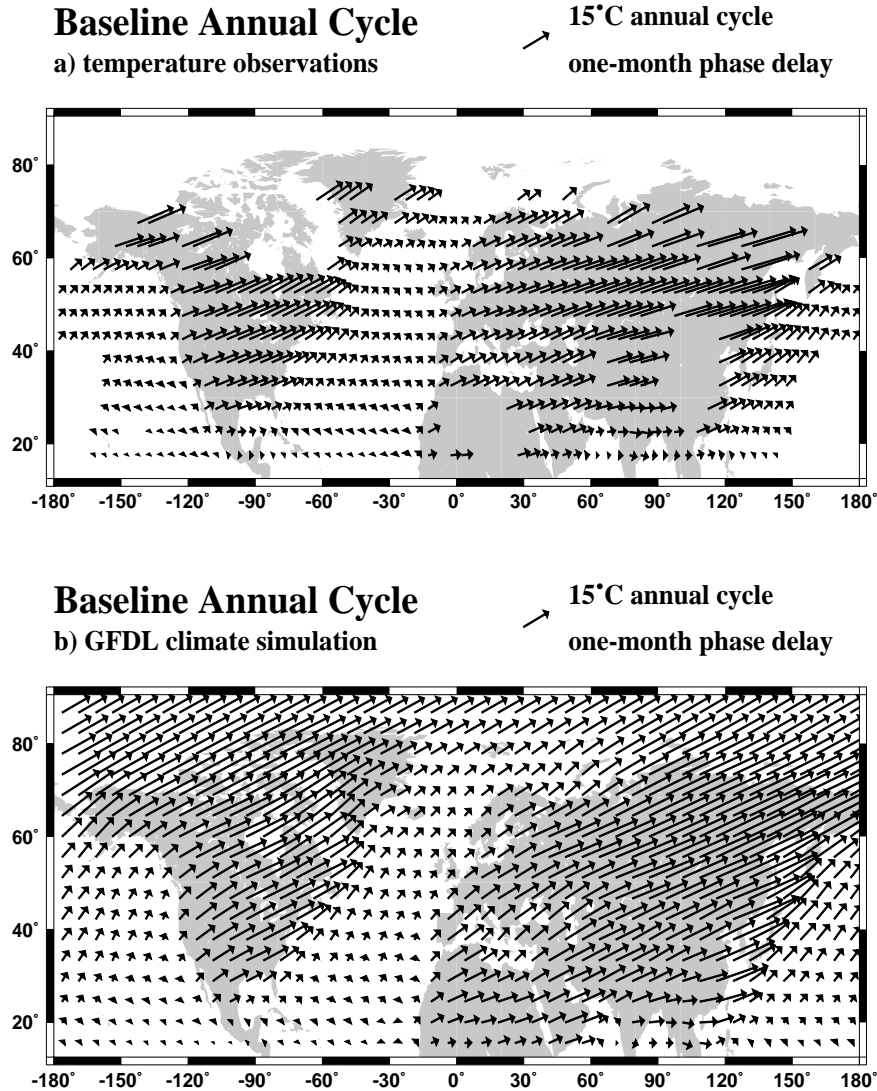
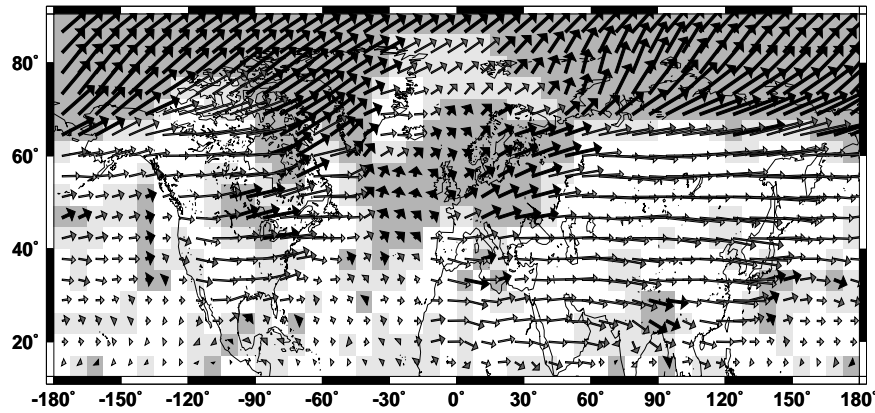


Figure 48: Phase and amplitude of the “baseline” annual cycle in temperature for (a) observation and (b) control GFDL simulation. A phase of 0° (rightward pointing arrow) indicates a minimum temperature that coincides with minimum insolation (Dec. 22nd) in the Northern Hemisphere. A 30° counter-clockwise rotation indicates a 1-month phase delay of minimum temperature relative to the insolation minimum. [From Mann and Park (1996a).]

GFDL Annual Cycle

a) change in phase

↗ 15°C annual cycle
9-day phase delay



GFDL Annual Cycle

b) change in amplitude

◇ +2°C per century
○ -2°C per century

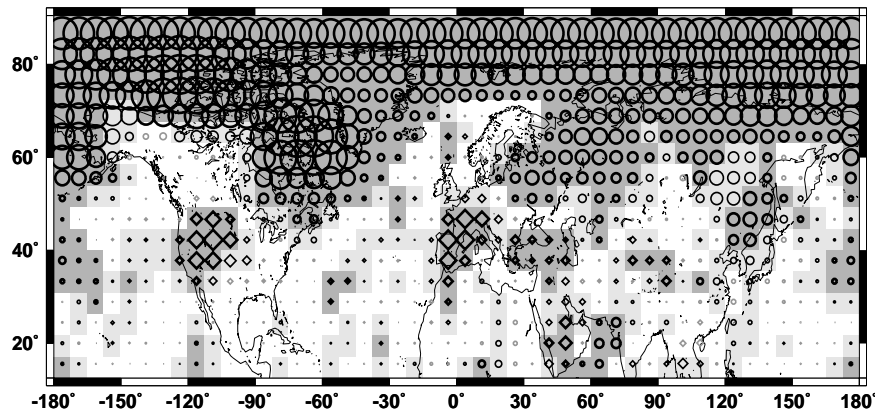


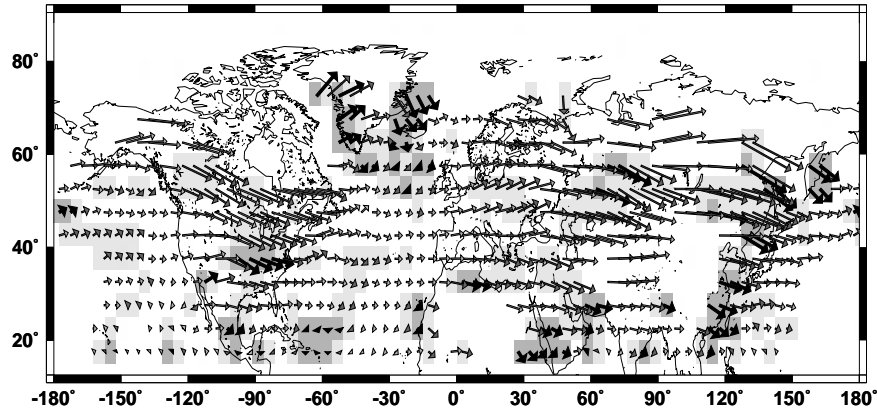
Figure 49: The linear trend of the annual cycle for the enhanced-greenhouse GFDL simulation (a) phase and (b) amplitude. Size of arrows scales the average amplitude of the annual cycle, while the direction indicates relative delay or advance of the annual cycle. A rightward arrow indicates no change in phase. Clockwise and counter-clockwise rotation indicates phase advances and delays, respectively. Significance of trends is indicated in terms of the ratio of the phase shift to its jackknife uncertainty estimate. Boldface symbols/darkest shading indicate nonzero phase and amplitude shifts at the $2\text{-}\sigma$ level, thin black symbols/medium shading indicate nonzero shifts at the $1\text{-}\sigma$ level, and gray symbols/no shading indicate shifts within $1\text{-}\sigma$ of zero. [From Mann and Park (1996a).]

The dominant response in both the CCM1 and GFDL models to increased CO₂ is one of substantial phase delays and amplitude decreases in high latitude oceanic regions. We interpret phase trend as arising from decreased winter sea ice cover and greater exposure of the surface to the ocean's mixed layer and its delayed thermal cycle. The amplitude trend is consistent with a strong positive ice-albedo feedback from reduced winter ice-cover. The close similarity of the primary response in these two very different model experiments suggests a consistent dynamical mechanism. Nonetheless, a more spatially-complex trend pattern in the GFDL coupled model (Figure 49) suggests other potential regional effects. Marginally significant phase advances, for example, are found in south central and eastern Asia. In the western U.S. the phase advance and amplitude increase suggests decreased maritime influence. The significance of these features, however, is comparable to those observed in the control experiment, suggesting that they may be associated with the model's natural century-scale variability rather than with a greenhouse response, or perhaps with some combination of these effects.

Observed amplitude trends (Figure 50) are $-2.4^{\circ}C < \delta A < +1.0^{\circ}C$. Phase advances and delays of 3°–7° (i.e. 3 to 7 days) are common. The largest δA is along the western margins of Greenland, where significant winter warming has occurred during the last century [*Jones and Briffa, 1992*]. Here, we also find the most significant trend towards a delayed (~ 8 days) annual cycle in the northern hemisphere consistent with the model-simulated signature of greenhouse-related decreases in high-latitude sea ice. In contrast, the phase of the annual cycle has advanced along the eastern margins of Greenland, where a long-term winter cooling trend is observed [*Jones and Briffa, 1992*]. This cooling appears to be associated with organized century-scale variability in the North Atlantic [see *Mann and Park, 1994*; *Schlesinger and Ramankutty, 1994*; *Mann et al, 1995b*] which could explain why the signature of greenhouse forcing is masked in this region. The annual cycle amplitude decreases in this location because winter cooling is offset by even greater summer cooling. A broad region of significant trends in annual cycle phase and amplitude is found in the extreme southwestern U.S. and offshore in the subtropical Pacific. This may be related to secular changes in the El Nino/Southern Oscillation (ENSO) and associated changes in patterns of summer coastal upwelling [e.g. *Trenberth and Hurrell, 1994*; *Graham, 1995*].

A combination of phase advances and amplitude decreases over mid-latitude

Observational Annual Cycle ↗ 15°C annual cycle
a) change in phase 4-day phase delay



Observational Annual Cycle ◇ +1°C per century ○ -1°C per century
b) change in amplitude

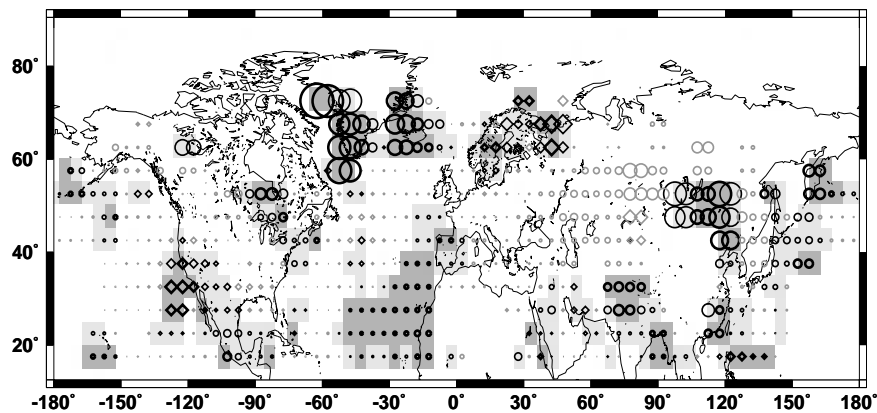


Figure 50: The linear trend in (a) phase and (b) amplitude of the annual cycle for the “dense” observational network of gridded land air and sea surface temperature data from 1899-1990 discussed in the text. Significance of trends indicated as in Figure 49. [From Mann and Park (1996a).]

continental interiors is consistent with an earlier snowmelt and runoff [*Lins and Michaels, 1994; Dettinger and Cayan, 1995; Groisman et al, 1994*] that may be related to greenhouse warming [*Lins and Michaels, 1994; Groisman et al, 1994*]. Few other locations in the Northern Hemisphere exhibit a consistent, readily interpretable annual cycle response. The constructive addition of trends in continental-interior regions is primarily responsible for the average ~ 1 day phase advance for the Northern Hemisphere.

Discussion and Summary

Both observations and model responses to greenhouse forcing show a trend towards decreased amplitude of the seasonal cycle in NH-average temperatures. The simulations suggest that these amplitude decreases may result from ice-albedo feedback. It is here, however, that the agreement ends; the observed and model-predicted trends in the phase of the seasonal cycle show little similarity.

If, as the models simulate, the dominant influence on annual-cycle amplitude $A(t)$ and phase $\phi(t)$ stems from high-latitude sea-ice decreases, the signature of greenhouse warming is scarcely evident in the observational data, which lack widespread high-latitude sampling. The trend in Western Greenland, the highest-latitude region in the observations, does nonetheless resemble model simulations. Some of these discrepancies could be due to the influence of sulfate aerosols which may have masked the effects of enhanced greenhouse gases in certain regions [see e.g., IPCC, 1996–chapter 8] and are not included as forcings in the simulations analyzed here. It should be noted however that the physical mechanisms are not yet well understood [*Hansen et al, 1997*]. It is possible that observed trends in phase, largely influenced by mid-latitude continental interiors, do not arise from greenhouse warming, but rather, at least in part, from natural variability. Such a notion is reinforced by the fact that marginally-significant trends are found in the control GFDL annual cycle, presumably due to organized century-scale internal variability.

If, on the other hand, the observed variation in the seasonal cycle truly represents a “fingerprint” of greenhouse warming, the GFDL and CCM1 models do not appear capable of capturing the detailed responses of the seasonal cycle to greenhouse forcing. In particular, if the phase advances that result from the behavior in continental interiors are not only statistically (as *Thomson [1995]* suggests), but in fact, causally related to greenhouse forcing, the predicted behavior of the models

in these regions would appear to be flawed. Deficiencies in certain aspects of the models (e.g., land surface parameterizations) could plausibly be at fault in such a scenario. The absence of an ENSO of realistic amplitude is also a potential shortcoming of model-predicted changes in seasonality, as some of the observed trends appear to show connections with ENSO.

It is possible, probably likely, that the observed trends in the seasonal cycle represent a combination of internal variability, enhanced greenhouse effects and external forcings. Various alternative scenarios are difficult to resolve, owing to limitations in the observational data and potential shortcomings in the models' descriptions of certain climate processes. The latter limitation may largely be overcome in newer generation climate models. Discrepancies between the observed and model-predicted trends must be resolved before a compelling connection can be drawn between 20th century changes in the behavior of the annual cycle in temperature, and anthropogenic forcing of the climate.

5. Conclusion

We have shown that traditional signal detection techniques suffer a number of weaknesses or limitations in the detection and reconstruction of irregular spatiotemporal oscillatory signals immersed in coloured noise. A methodology for signal detection and reconstruction of such signals – the MTM-SVD methodology – is offered as an alternative technique which avoids most of these problems, and provides an efficient exploratory method for climate signal detection. The associated signal detection parameter – the LFV spectrum – yields the correct null distribution for a very general class of spatiotemporal climate noise processes, and the correct inferences when signals are present. The methodology allows for a faithful reconstruction of the arbitrary spatiotemporal patterns of narrowband signals immersed in spatially-correlated noise. Furthermore, the results of the MTM-SVD approach are robust to the temporal and spatial sampling inhomogeneities that are common in actual climate data.

Applied to observational climate data, the MTM-SVD analysis yields insight into secular trends, low-frequency and high-frequency quasi-oscillatory variations in the climate system. The dominant mode of secular variation during the last century is a long-term global warming trend associated with some anomalous atmospheric

circulation patterns that show similarity to the modeled response of the climate to increased greenhouse gases. Nonetheless, a substantial ~ 70 year “century-scale” or “multidecadal” secular variation suggestive of longer-term oscillatory behavior is superimposed on this trend in both the global temperature and joint northern hemisphere temperature/SLP fields, exhibiting substantial SLP and temperature variations in the North Atlantic, and displaying a notable high-latitude signature in the temperature field. The analysis of multiple centuries of proxy data suggests that 50-100 year internal oscillations with similar features persist over several centuries. Similar oscillatory signals were attributed to variability in the thermohaline circulation and possible coupled ocean-atmosphere processes in recent model simulation studies. An analysis of the seasonal cycle in surface temperature in the observations and long coupled model integrations suggests the impact of both anthropogenic forcing and multidecadal oscillatory variations on seasonality in surface temperature.

An interdecadal 16-18 year climate signal is clearly evident in the instrumental climatic fields analyzed, and appears at some level to be consistent with a mechanism involving gyre spinup and mid-latitude ocean-atmosphere interaction which has also been predicted in a recent coupled-ocean atmosphere simulation. A connection with decadal-scale ENSO variability, suggested both by correlations with standard ENSO indices and ENSO-like teleconnections in temperature and atmospheric circulation, suggest a complexity to the signal which has not been well explained. Analysis of long-term proxy data demonstrates evidence for the persistent, if intermittent, nature of this cycle over many centuries. The frequency modulation of the interdecadal signal evident in these longer-term data seems complicate the interpretation in terms of any simple linear dynamical mechanism. Weaker quasidecadal oscillations are evident, but with statistical confidence. Our analyses also substantiates the importance of oscillatory behavior on interannual timescales associated with ENSO and quasibiennial oscillations, and provides insight into the long -term changes in such relatively high frequency climatic processes.

Acknowledgments

M.E.M. acknowledges support from the U.S. Dept. of Energy through the Alexander Hollaender Distinguished Postdoctoral Research Fellowship program. This work was

originally supported by the NSF Climate Dynamics Program, Grant ATM-9222592.

The authors greatly appreciate the thoughtful and constructive review provided by John Lanzante. Helpful comments were also provided by David Parker and Barry Saltzman. Valuable feedback and constructive criticism during various stages of development and application of this research is acknowledged from many individuals, including Myles Allen, Philip Bogden, Michael Ghil, Yochanan Kushnir, Upmanu Lall, Robert Livezey, Balaji Rajagopalan, Ronald Smith, and David Thomson.

REFERENCES

- Allen, M. R. and L. A. Smith, 1994: Investigating the origins and significance of low-frequency modes of climatic variability. *Geophys. Res. Lett.*, **21**, 883–886.
- Allen, M.R. and A. W. Robertson, 1996: Distinguishing modulated oscillations from coloured noise in multivariate datasets, *Clim. Dyn.*, in press.
- Angell, J.K., 1990: Variation in global tropospheric temperature after adjustment for the El Nino influence, 1958-1989, *Geophys. Res. Lett.*, **17**, 1093–1096.
- Barnett, T.P., 1983: Interaction of the monsoon and Pacific tradewind systems at interannual time scales. Part I: The equatorial zone, *Mon. Wea. Rev.*, **111**, 756–773.
- Barnett, T.P., 1991: The interaction of multiple time scales in the tropical climate system. *J. Clim.*, **4**, 269–281.
- Barnett, T.P., Santer, B., Jones, P.D., and R.S. Bradley, 1996: Estimates of low frequency natural variability in near-surface air temperature, *Holocene*, **6**, 255–263 (1996).
- Barnston, A.G., and R.E. Livezey, 1987: Classification, seasonality and persistence of low-frequency atmospheric circulation patterns. *Mon. Wea. Rev.*, **115**, 1083–1126.
- Barnston, A.G., Livezey, R.E. and M.S. Halpert, 1991: Modulation of Southern Oscillation–northern hemisphere mid-winter climate relationships by the QBO. *J. Clim.*, **4**, 203–227.
- Bottomley, M., Folland, C.K., Hsiung, J., Newell, R.E. and Parker, D.E., 1990: Global ocean surface temperature atlas (GOSTA), Joint Meteorological Office and Massachusetts Institute of Technology Project, U.K. Depts. of the

- Environment and Energy, HMSO, London.
- Bradley, R.S., *Precipitation History of the Rocky Mountain States*, Westview Press, Boulder, CO, 1976.
- Bradley, R.S. and Jones, P.D, 1993: “Little Ice Age” summer temperature variations: their nature and relevance to recent global warming trends, *Holocene*, **3**, 367–376 (1993).
- Bradley, R.S., Mann, M.E., and J. Park, 1994: A spatiotemporal analysis of ENSO variability based on globally distributed instrumental and proxy temperature data. *Eos supplement*, **75**, 383.
- Bretheron, C.S., Smith, C. and J.M. Wallace, 1992: An Intercomparison of Methods for Finding Coupled Patterns in Climate Data, *J. Climate*, **5**, 541–560.
- Brillinger, D., *Time Series–Data Analysis and theory*, McGraw-Hill, 1981.
- Burroughs, W.J., 1992: *Weather cycles: real or imaginary?*, Cambridge Univ. press, 1992.
- Bursor, G., 1993: Complex principal oscillation pattern analysis, *J. Climate*, **6**, 1972–1986.
- Cai, W. and S.J. Godfrey, 1995: Surface heat flux parameterizations and the variability of the thermohaline circulation, *J. Geophys. Res.*, **100**, 10679–10692.
- Cane, M.A., Zebiak, S.E., and S.C. Dolan, 1986: Experimental forecasts of El Nino, *Nature*, **321**, 827–832.
- Cane, M.A. and S.E. Zebiak, 1987: Prediction of El Nino events using a physical model, in *Atmospheric and Oceanic Variability*, H. Cattle, ed., Royal Meteorological Society Press, 153–182.
- Cane, M.A., Clement, A.C., Kaplan, A., Kushnir, Y., Pozdnyakov, D., Seager, R., Zebiak, S.E., Murtugudde, R., 1997: Twentieth-Century Sea Surface Temperature Trends, *Science*, **275**, 957–960.
- Cayan, D.R., 1992a: Latent and sensible heat flux anomalies over the northern oceans: The connection to monthly atmospheric circulation, *J. Climate*, **5**, 354–369.
- Cayan, D.R., 1992b: Latent and sensible heat flux anomalies over the northern oceans: Driving the sea surface temperature, *J. Phys. Oceanogr.*, **22**, 859–881.
- Chang, P., Link, J. and H. Li, 1997: A decadal climate variation in the tropical Atlantic Ocean from thermodynamic air-sea interactions, *Nature*, **385**, 516–

- Chen, F. and M. Ghil, 1995: Interdecadal variability of the thermohaline circulation and high-latitude surface fluxes. *J. Phys. Oceanogr.*, **25**, 2547–2568.
- Chen, F. and M. Ghil, 1996: Interdecadal variability in a hybrid coupled ocean-atmosphere model, *J. Phys. Oceanogr.*, in press.
- Cheng, X., and T. J. Dunkerton, 1995: Rotation of spatial patterns derived from singular value decomposition analysis, *J. Climate*, **8**, 2631–2643.
- Cherry, S., 1997: Some comments on singular value decomposition analysis, *J. Climate*, **10**, 1759–1766.
- Cole, J.E., Fairbanks, R.G., and G.T. Shen, 1993: Recent variability in the Southern Oscillation: isotopic results from a Tarawa atoll coral. *Science*, **260**, 1790–1793.
- Currie, R.G., and D.P. O’Brien, 1992: Deterministic signals in USA precipitation records; II, *Int. J. Climatol.*, **12**, 281–304.
- Darby, M.S. and L.A. Mysak, 1993: A boolean delay equation model of an interdecadal Arctic climate cycle. *Clim. Dyn.*, **8**, 241–246, 1993.
- Davis, N.E., The variability of the onset of spring in Britain, 1972: *Quart. J. Roy. Met. Soc.*, **418**, 763.
- Delworth, T., Manabe, S., and R.J. Stouffer, 1993: Interdecadal variations of the thermohaline circulation in a coupled ocean-atmosphere model. *J. Clim.*, **6**, 1993–2011.
- Delworth, T.D., Manabe, S. and R.J. Stouffer, R.J., 1997: Multidecadal climate variability in the Greenland Sea and surrounding regions: a coupled model simulation, *Geophys. Res. Lett.*, **24**, 257–260.
- Deser, C., and M. Blackmon, 1993: Surface climate variations over the North Atlantic ocean during winter: 1900–1989. *J. Clim.*, **6**, 1743–1753.
- Dettinger, M.D., Ghil, M., and C.L. Keppenne, 1995: Interannual and interdecadal variability in United States surface-air temperatures, 1910–1987. *Clim. Change*, **31**, 36–66.
- Dettinger, M.D. and D.R. Cayan, 1995: Large-scale atmospheric forcing of recent trends toward early snowmelt runoff in California, *J. Clim.* **8**, 606.
- Diaz, H. and Pulwarty, R.S., 1994: *Climatic Change* **26**, 317–342.
- Dickey, J.O., S.L. Marcus, and R. Hide, Global propagation of interannual fluctuations in atmospheric angular momentum: 1992, *Nature*, **357**, 484–488.

- Dickson, B., From the Labrador Sea to global change, 1997: *Nature*, **386**, 649-650.
- Dunbar, R.B., Wellington, G.M., Colgan, M.W. and P.W. Glynn, Eastern Pacific sea surface temperature since 1600 A.D.: The δ^{18} record of climate variability in Galapagos corals, 1994: *Paleocn.*, **9**, 291-315.
- Efron, B., 1990: The Jackknife, the Bootstrap and Other Resampling Plans, Society for Applied and Industrial Mathematics, Philadelphia, pp 92.
- Folland, C. K., Parker D. E., and F. E. Kates, 1984: Worldwide marine temperature fluctuations 1856-1981. *Nature*, **310**, 670-673.
- Folland, C.K., Palmer, T.N., and D.E. Parker, 1986: Sahel rainfall and worldwide sea temperatures, *Nature*, **320**, 602-606.
- Fraedrich, K., Bantzer, C. and U. Burkhardt, 1993: Winter climate anomalies in Europe and their associated circulation at 500 hPa. *Clim. Dyn.*, **8**, 161-175.
- Friis-Christensen, E., and K. Lassen, 1991: Length of the solar cycle: An indicator of solar activity closely associated with climate, *Science*, *254*, 698-700.
- Ghil, M., and R. Vautard, 1991: Interdecadal oscillations and the warming trend in global temperature time series. *Nature*, **350**, 324-327.
- Ghil, M. and P. Yiou, 1996: Spectral methods: what they can and cannot do for climatic time series, in *Decadal Climate Variability*, Springer Verlag, 446-482, 1996.
- Gilman, D.L., Fuglister, F.J., and J.M. Mitchell, Jr., 1963: On the power spectrum of "red noise", *J. Atmos. Sci.*, **20**, 182-184.
- Gordon, A.L., S.E. Zebiak, and K. Bryan, 1992: Climate variability and the Atlantic ocean, *Eos Trans., AGU*, **73**, 161-165.
- Graham, N.E., Michaelsen, J., and T.P. Barnett, 1987: An investigation of the El Nino-Southern Oscillation cycle with statistical model. Predictor field characteristics. *J. Geophys. Res.*, **92**, 14251-14270.
- Graham, N.E., 1994: Decadal-scale climate variability in the tropical and North Pacific during the 1970s and 1980s: observations and model results. *Clim. Dyn.*, **10**, 135-162.
- Graham, N.E., 1995: Simulation of recent global temperature trends, *Science*, *267*, 666-671.
- Greatbatch, R.J. and S. Zhang, 1995: An interdecadal oscillation in an idealized ocean basin forced by constant heat flux, *J. Clim.*, **8**, 81-91.
- Griffies, S.M., and E. Tziperman, 1995: A linear thermohaline oscillator driven by

- stochastic atmospheric forcing, *J. Clim.*, **8**, 2440–2453.
- Griffies, S.M. and K. Bryan, 1997: Predictability of North Atlantic Multidecadal Climate Variability, *Nature*, **275**, 181–184.
- Groisman, P. Ya, Karl, T.R., and R.W. Knight, Observed impact of snow cover on the heat balance and the rise of continental spring temperatures, *Science*, **263**, 198, 1994.
- Gu, D., and S. G. H. Philander, 1997: Interdecadal climate fluctuations that depend on exchanges between the tropics and extratropics, *Science*, **275**, 805–807.
- Halpert, M.S., and C.F. Ropelewski, 1992: Surface temperature patterns associated with the Southern Oscillation, *J. Clim.*, **5**, 577–593.
- Hansen, J., Sato, M. and R. Ruedy, 1997: The missing climate forcing, *Phil. Trans. R. Soc. Lond.*, **B 352**, 231–240.
- Hasselmann, K., 1976: Stochastic climate models, part I. Theory, *Tellus*, **28**, 473–478.
- Hasselmann, K., 1988: PIPs and POPs: The reduction of complex dynamical systems using principal interaction and oscillation patterns, *J. Geophys. Res.*, **93**, 11015–11021.
- Horel, J.D., and J.M. Wallace, 1981: Planetary-scale atmospheric phenomena associated with the Southern Oscillation. *Mon Wea. Rev.*, **109**, 813–829.
- Houghton, R., and Y. Tourre, 1992: Characteristics of Low-Frequency sea-surface temperature fluctuations in the tropical atlantic. *J. Clim.*, **5**, 765–771.
- Huang, R.X., 1993: Real freshwater flux as a natural boundary condition for the salinity balance and thermohaline circulation forced by evaporation and precipitation, *J. Phys. Ocean.*, **23**, 2428–2446.
- Hughes, M. and Diaz, H.F., 1994: Was there a “medieval warm period”, and if so, where and when?, *Clim. Change*, **26**, 109–142.
- Hurrell, J. W. and H. van Loon, 1994: A modulation of the atmospheric annual cycle in the Southern Hemisphere. *Tellus*, **46A**, 325–338.
- Hurrell, J., 1995: Decadal trends in the North Atlantic Oscillation and relationship to regional temperature and precipitation, *Science*, **269**, 676–679.
- IPCC, *Climate Change 1995, the science of climate change*, J.T., Houghton, L.G. Meira Filho, B.A. Callender, N. Harris, A. Kattenberg and K. Maskell Eds., Cambridge University Press, 1996.
- Jacoby, G.C. and D’arrigo, R. *Clim. Change* **14**, 39–59 (1989).

- Jin, F.F, Neelin, J.D., and M. Ghil, 1994: El Nino on the devil's staircase: annual subharmonic steps to chaos, *Science*, **264**, 70–72.
- Jones, P.D., 1989: The influence of ENSO on global temperatures, *Clim. Monit.*, **17**, 80–89.
- Jones, P.D., 1994: Hemispheric surface temperature variations: A reanalysis and an update to 1993, *J. Clim.*, **7**, 1794–1802.
- Jones, P.D., S.C. Raper, R.S. Bradley, H.F. Diaz, P.M. Kelly, and T.M. Wigley, Northern hemisphere surface air temperature variations, *J. Clim. Appl. Meteorol.*, **25**, 161–179, 1986.
- Jones, P.D., and K.R. Briffa, 1992: Global surface air temperature variations during the 20th century: Part 1–Spatial, temporal and seasonal details, *Holocene*, **1**, 165–179.
- Kaplan, A., M.A. Cane, Y. Kushnir, A.C. Clement, M.B. Blumenthal, and B. Rajagopalan, 1997: Analyses of global sea surface temperature 1865-1991, *J. Geophys. Res.*, submitted.
- Keppenne, C.L. and M. Ghil, 1992: Adaptive filtering and prediction of the Southern Oscillation index, *J. Geophys. Res.*, **97**, 20449–20454.
- Keppenne, C.L. and M. Ghil, 1993: Adaptive filtering and prediction of noisy multivariate signals: An application to Atmospheric Angular Momentum, *Inter. J. Bifurc. and Chaos*, **3**, 625–634.
- Kim, K.Y., and G.R. North, 1991: Surface temperature fluctuations in a stochastic climate model, *J. Geophys. Res.*, **96**, 18573–18580.
- Kuo, C., Lindberg, C. and D.J. Thomson, 1990: Coherence established between atmospheric carbon dioxide and global temperature, *Nature*, **343**, 709–713.
- Kurgansky, M.V., Dethloff, K., Pisnichenko, I.A., Gernandt, H., Chmielewski, F.-M., and W. Jansen, Long-term climate variability in a simple nonlinear atmospheric model, 1996: *J. Geophys. Res.*, **101D**, 4299–4314.
- Kushnir, Y., 1994: Interdecadal variations in North Atlantic sea surface temperature and associated atmospheric conditions, *J. Clim.*, **7**, 141–157.
- Kutzbach, J.E. and R.A. Bryson, R.A., 1974: Variance spectrum of Holocene climatic fluctuations in the North Atlantic Sector, *J. Atmos. Sci.*, **31**, 1958–1963.
- Labitzke, K., and H. van Loon, 1988: Associations between the 11-year solar cycle, the QBO, and the atmosphere. Part I: The troposphere and stratosphere in

- the northern hemisphere in winter, *J. Atmos. Terr. Phys.*, **50**, 197–206.
- Lall, U. and M. Mann, 1995: The Great Salt Lake: A barometer of low-frequency climatic variability, *Wat. Res. Res.*, **31**, 2503–2515.
- Lamb, P.J. and R.A. Pepler, 1987: North Atlantic oscillation: concept and an application, *Bull. Am. Meteorol. Soc.*, **68**, 1218–1225.
- Lanzante, J., R., 1990: The Leading Modes of 10-30 Day Variability in the Extratropics of the Northern Hemisphere during the Cold Season, *J. Atmos. Sci.*, **47**, 2115–2140.
- Latif, M. and T.P. Barnett, 1994: Causes of decadal climate variability over the North Pacific and North America, *Science*, **266**, 634–637.
- Lean, J., Beer, J. and R.S. Bradley, 1995: Comparison of proxy records of climate change and solar forcing, *Geophys. Res. Lett.*, **22**, 3195–3198.
- Lilly, J. and J. Park, 1995: Multiwavelet spectral and polarization analysis of seismic records. *Geophys. J. Int.*, **122**, 1001–1021.
- Lins, H.F. and P.J. Michaels, Increasing U.S. streamflow linked to greenhouse forcing, *Eos*, **75**, 281–285, 1994.
- Linsley, B.K., Dunbar, R.B., Wellington, G.M. and D.A. Mucciarone, 1994: A coral-based reconstruction of intertropical convergence zone variability over Central America since 1707, *J. Geophys. Res.*, **99**, 9977–9994.
- Liu, Q. and T. Opsteegh, 1995: Interannual and decadal variations of blocking activity in a quasi-geostrophic model, *Tellus*, **47**, 941–954.
- Livezey, R.E., and K.C. Mo, 1987: Tropical-extratropical teleconnections during the northern hemisphere winter. Part II: Relationships between monthly mean northern hemisphere circulation patterns and proxies for tropical convection. *Mon. Wea. Rev.*, **115**, 3115–3132.
- Livezey, R.E., and W.Y. Chen, 1983: Statistical field significance and its determination by Monte Carlo techniques, *Mon. Weather Rev.*, **111**, 46–59.
- Lorenz, E.N., Can chaos and intransitivity lead to interannual variability?, *Tellus*, **42A**, 378–389, 1990.
- Madden, R.A., D.J. Shea, G.W. Branstator, J.J. Tribbia, and R.O. Weber, The effects of imperfect spatial and temporal sampling on estimates of the global mean temperature: Experiments with model data, *J. Clim.*, **6**, 1057–1066, 1993.
- Maier-Reimer, E., and U. Mikolajewicz, 1989: Experiments with an OGCM on

- the cause of the Younger-Dryas. *Oceanography*, A. Ayala-Castanares, W. Wooster, and A. Yanez-Arancibia, Eds., UNAM Press, 87-100.
- Manabe, S., Stouffer, R.J., Spelman, M.J. and K. Bryan, Transient responses of a coupled ocean-atmosphere model to gradual changes of atmospheric CO₂. Part I: Annual Mean Response, *J. Clim.*, *4*, 785–818, 1991.
- Mann, M.E., and J. Park, 1993: Spatial correlations of interdecadal variation in global surface temperatures. *Geophys. Res. Lett.*, *20*, 1055–1058.
- Mann, M.E., and J. Park, 1994: Global-scale modes of surface temperature variability on interannual to century timescales. *J. Geophys. Res.*, **99**, 25819–25833.
- Mann, M.E., Lall, U., Saltzman, B., 1995: Decadal-to-century scale climate variability: Insights into the Rise and Fall of the Great Salt Lake, *Geophysical Research Letters*, **22**, 937–940.
- Mann, M.E., Park, J. and R. Bradley, 1995: Global interdecadal and century-scale oscillations during the past five centuries, *Nature*, *378*, 266-270.
- Mann, M.E., and J. Lees, 1996: Robust Estimation of Background Noise and Signal Detection in Climatic Time Series, *Clim. Change*, **33**, 409–445.
- Mann, M.E., 1998: *A Study of Ocean-Atmosphere Interaction and Low Frequency Variability of the Climate System*, Ph.D Thesis, 283pp, Yale University, New Haven, CT.
- Mann, M.E. and J. Park, 1996: Greenhouse warming and changes in the seasonal cycle of temperature: model versus observations, *Geophys. Res. Lett.*, **23**, 1111–1114.
- Mann, M.E. and J. Park, 1996: Joint spatio-temporal modes of surface temperature and sea level pressure variability in the Northern Hemisphere during the last century, *J. Climate*, **9**, 2137–2162.
- Marple, S. L. Jr., Digital spectral analysis with applications, Prentice-Hall, Englewood Cliffs, 1987.
- Marshall, S., Mann, M.E., Oglesby, R.J., and B. Saltzman, 1995: A comparison of the CCM1-simulated climates for pre-industrial and present-day CO₂ levels. *Glob. Planet. Change*, **10**, 163–180.
- Mehta, V.M. and T. Delworth, 1995: Decadal variability of the tropical Atlantic ocean surface temperature in shipboard measurements and in a global ocean-atmosphere model. *J. Clim.*, **8**, 172–190.
- Mitra, K., S. Mukherji, and S.N. Dutta, 1991: Some indications of 18.6 year luni-

- solar and 10-11 year solar cycles in rainfall in northwest India, the plains of Uttar Pradesh and north-central India, *Int. J. Climatol.*, **11**, 645–652.
- Moron, V., Vautard, V. and M. Ghil, 1997: Trends, interdecadal and interannual oscillations in global sea-surface temperatures, *Clim. Dyn.*, in press.
- Mysak, L.A., and S.B. Power, 1992: Sea-ice anomalies in the western Arctic and Greenland-Iceland Sea and their relation to an interdecadal climate cycle. *Climatol. Bull.*, **26**, 147–176.
- Mysak, L.A., T.F. Stocker, and F. Huang, 1993: Century-scale variability in a randomly forced, two-dimensional thermohaline ocean circulation model, *Clim. Dyn.*, **8**, 103-116, 1993.
- Namias, J., 1983: Short period climatic variations, *Collected works of J. Namias, 1975 Through 1982, Vol. III*, University of California, San Diego, 393 pp.
- Naujokat, B., 1996: An update of the observed quasibiennial oscillation of the stratospheric winds over the tropics. *J. Atmos. Sci.*, **43**, 1873–1877.
- Newman, M., and P.D. Sardeshmukh, 1995: A caveat concerning singular value decomposition, *J. Climate*, **8**, 352–360.
- Oglesby, R.J. and B. Saltzman, 1992: Equilibrium climate statistics of a general circulation model as a function of atmospheric carbon dioxide. Part I: Geographic distributions of primary variables, *J. Clim.*, **5**, 66–92.
- Palmer, T.N. and Z. Sun, 1985: A modeling and observational study of the relationship between sea surface temperature in the northwest Atlantic and the atmospheric general circulation, *Quart. J. Roy. Meteor. Soc.*, **111**, 947–975.
- Park, J., 1992: Envelope estimation for quasi-periodic geophysical signals in noise: A multitaper approach, in *Statistics in the Environmental and Earth Sciences*, A.T. Walden and P. Guttorp (Eds.), 189-219, Edward Arnold, London.
- Park, J., Lindberg, C.R., and F. L. Vernon III, 1987: Multitaper spectral analysis of high-frequency seismograms. *J. Geophys. Res.*, **92**, 12675–12684.
- Park, J., and K.A. Maasch, 1993: Plio-Pleistocene time evolution of the 100-kyr cycle in marine paleoclimate records. *J. Geophys. Res.*, **98**, 447–461, 1993.
- Park, J., and M.E. Mann, 1998: Interannual Temperature Events and Shifts in Global Temperature: A Multiple Wavelet Correlation Approach, *Earth Interactions* (in revision).
- Parker, D.E., Folland, C.F. and M. Jackson, 1995: Marine surface temperature: observed variations and data requirements, *Clim. Change*, **31**, 559–600.

- Percival, D.B. and A.T. Walden, 1993: *Spectral Analysis for Physical Applications* (Cambridge University Press, 1993).
- Philander, S.G.H., *El Nino, La Nina, and the Southern Oscillation* (Academic Press, 1990).
- Pedlosky, J., 1987: *Geophysical Fluid Dynamics*, 710pp., Springer-Verlag, New York.
- Peixoto, J.P. and A.H. Oort, 1992: *Physics of Climate*, 520 pp., American Institute of Physics, New York.
- Pierce, D.W., Barnett, T.P., and U. Mikolajewicz, 1995: Competing roles of heat and freshwater flux in forcing thermohaline oscillations. *J. Phys. Oceanogr.*, **25**, 2046–2064.
- Preisendorfer, R.W., 1988: Principal component analysis in meteorology and oceanography. *Development in atmospheric science*, 17, Elsevier, Amsterdam, pp 425.
- Quon, C., and M. Ghil, 1995: Multiple equilibria and stable oscillations in thermosolutal convection at small aspect ratio. *J. Fluid Mech.*, **291**, 33–56.
- Quinn, W.H. and V.T. Neal, 1992: The historical record of El Nino Events, in *Climate Since A.D. 1500*, edited by R.S. Bradley and P.D. Jones, pp. 623–648, Routledge, Boston.
- Rajagopalan, B. and U. Lall, 1995: Seasonality of precipitation along a meridian in the western United States, *Geophys. Res. Lett.*, *22*, 1081-1084.
- Rajagopalan, B., Cook, E., and M.A. Cane, 1996: Joint spatiotemporal modes of U.S. PDSI and Pacific SST variability, *Eos supplement, AGU*, **77**, 126.
- Rajagopalan, B., Mann, M.E., and U. Lall, 1998: A Multivariate Frequency-Domain Approach to Long Lead Climate Forecasting, *Weather and Forecasting*, in press.
- Richman, M.B., 1986: Rotation of principal components, *J. Climatol.*, **6**, 293–355.
- Robock, A., 1996: Stratospheric control of climate, *Science*, **272**, 972–973.
- Rogers, J.C., 1984: The association between the North Atlantic Oscillation and the Southern Oscillation in the Northern Hemisphere, *Mon. Wea. Rev.*, **112**, 1999–2015.
- Ropelewski, C.F., and M.S. Halpert, 1987: Global and regional scale precipitation patterns associated with the El Nino-Southern Oscillation, *Mon. Weather Rev.*, *115*, 1606–1626.
- Ropelewski, C.F., Halpert, M.S., and X. Wang, 1992: Observed tropospheric bien-

- nial variability and its relationship to the Southern Oscillation. *J. Clim.*, **5**, 594–614.
- Royer, T.C., 1993: High-latitude oceanic variability associated with the 18.6 year nodal tide, *J. Geophys. Res.*, **98**, 4639–4644.
- Roebber, P.J., 1995: Climate variability in a low-order coupled atmosphere-ocean model, *Tellus*, **47**, 473–494.
- Saltzman, B., Sutera, A. and A. Evenson, 1981: Structural Stochastic Stability of a Simple Auto-Oscillatory Climatic Feedback System, *J. Atmos. Sci.*, **38**, 494–503.
- Saltzman, B., 1982: Stochastically-driven climatic fluctuations in the sea-ice, ocean temperature, CO₂ feedback system, *Tellus*, **34**, 97–112.
- Saltzman, B. and R. E. Moritz, 1980: A time-dependent climatic feedback system involving sea-ice extent, ocean temperature, and CO₂, *Tellus*, **32**, 93–118.
- Saravanan, R. and J. C. McWilliams, 1995: Multiple equilibria, natural variability, and climate transitions in an idealized ocean-atmosphere model, *J. Clim.*, **8**, 2296–2323.
- Schlesinger, M.E., and N. Ramankutty, 1994: An oscillation in the global climate system of period 65–70 years, *Nature*, **367**, 723–726.
- Schmidt, G.A. and L.A. Mysak, 1996: The stability of a zonally averaged thermohaline circulation model, *Tellus*, **48A**, 158–178.
- Slowey, N.C. and Crowley, T.J., 1995: *Geophys. Res. Lett.*, **22**, 2345–2348.
- Stocker, T.F., 1996: An overview of century time-scale variability in the climate system: observations and models. In D.L.T. Anderson and J. Willebrand (Eds.), *Decadal Climate Variability: Dynamics and Predictability, NATO ASI, volume 1*, Springer-Verlag, in press.
- Stocker, T.F., Wright, D.G., and L.A. Mysak, 1992: A zonally averaged coupled ocean-atmosphere model for paleoclimate studies, *J. Clim.*, **5**, 773–797.
- Tanimoto, Y., Iwasaka, N., Hanawa, K. and Y. Toba, 1993: Characteristic-variations of sea surface temperature with multiple time scales in the North Pacific. *J. Clim.*, **6**, 1153–1160.
- Thomson, D. J., 1982: Spectrum estimation and harmonic analysis, *IEEE Proc.*, **70**, 1055–1096.
- Thomson, D.J., 1990: Time-series analysis of Holocene climate data, *Phil. Trans. R. Soc. Lond., A.*, **330**, 601–616 (1990).

- Thomson, D.J, 1995: The seasons, global temperature, and precession, *Science*, **268**, 59–68.
- Thompson, L., in *Climate Since A.D. 1500* (eds Bradley, R.S. and Jones, P.D.) (517–548) Routledge and Kegan Paul, Boston, 1992).
- Thompson, R., Complex demodulation and the estimation of the changing continentality of Europe’s climate, *Int. J. Climatol.*, **15**, 175, 1995.
- Tinsley, B.A, 1988: The solar cycle and QBO influence on the latitude of storm tracks in the north Atlantic, *Geophys. Res. Lett.*, **15**, 409.
- Tourelle, Y., Rajagopalan, B. and Y. Kushnir, 1998: Dominant patterns of climate variability in the Atlantic over the last 136 years, *J. Climate* (in press).
- Trenberth, K.E., What are the seasons?, 1983: *Bull. Am. Meteorol. Soc.*, **64**, 1276–1282.
- Trenberth, K.E., 1990: Recent observed interdecadal climate changes in the northern hemisphere. *Bull. Am. Met. Soc.*, **71**, 988–993.
- Trenberth, K.E., and D.A. Paolino, 1980: The Northern Hemisphere sea-level pressure data set: trends, errors and discontinuities. *Mon. Wea. Rev.*, **108**, 855–872.
- Trenberth, K.E., and W-T K. Shin, 1984: Quasibiennial fluctuations in sea level pressures over the Northern Hemisphere. *Mon. Wea. Rev.*, **112**, 761–777.
- Trenberth, K.E. and D. J. Shea, 1987: On the evolution of the Southern Oscillation. *Mon Wea. Rev.*, **115**, 3078–3096.
- Trenberth, K.E. and J.W. Hurrell, 1994: Decadal atmosphere-ocean variations in the Pacific. *Clim. Dyn.*, **9**, 303–319.
- Trenberth, K.E. and T. J. Hoar, 1995: The 1990-1995 El Nino-Southern Oscillation Event: Longest on Record, *Geophys. Res. Lett.*, **23**, 57–60.
- Tziperman, E., Stone, L., Cane, M.A., and H. Jarsoh, 1994: El Nino chaos: overlapping of resonances between the seasonal cycle and the Pacific ocean-atmosphere oscillator, *Science*, **264**, 72–74.
- Unal, Y.S. and M. Ghil, 1995: Interannual and interdecadal oscillation patterns in sea level, *Clim. Dyn.*, **11**, 255–279.
- Vautard, R. and M. Ghil, 1989: Singular spectrum analysis in nonlinear dynamics, with applications to paleoclimate time series, *Physica D*, **35**, 395–424.
- Vautard, R., Yiou, P. and M. Ghil, 1992: Singular spectrum analysis: a toolkit for short noisy chaotic signals, *Physica D*, **58**, 95–126.

- Venegas, S. A., Mysak, L.A. and D.N. Straub, 1996: Evidence for interannual and interdecadal climate variability in the South Atlantic, *Geophys. Res. Lett.*, **23**, 2673–2676.
- Vines, R.G., Rainfall patterns in India, 1986: *J. Climatol.*, **6**, 135–138.
- Von Storch, J.S., 1994: Interdecadal variability in a global coupled model. *Tellus*, **46**, 419–432.
- Wallace, J.M. and R.E. Dickinson, 1972: Empirical orthogonal representation of time series in the frequency domain. Part I: Theoretical considerations, *J. Appl. Meteor.*, **11**, 887–892.
- Wallace, J.M., Smith, C. and C.S Bretherton, 1992: Singular value decomposition of wintertime sea surface temperatures and 500-mb height anomalies. *J. Clim.*, **5**, 561–576.
- Wallace, J.M., and D.S. Gutzler, 1981: Teleconnections in the geopotential height field during the northern hemisphere winter, *Mon. Weather Rev.*, **109**, 784–812.
- Weaver, A.J., Sarachik, E.S., and J. Marotzke, 1991: Freshwater flux forcing of decadal and interdecadal oceanic variability. *Nature*, **353**, 836–838.
- Weaver, A.J., and Sarachik, E., 1991: Evidence of decadal variability in an ocean general circulation model: An advective mechanism, *Atmos. Ocean*, **29**, 197–231.
- Weare, B.C. and Jasstrom, J.S., 1982: Examples of extended empirical orthogonal function analyses, *Mon. Wea. Rev.*, **110**, 481–485.
- Wigley, T.L., and R. Raper, 1990: Natural variability of the climate system and detection of the greenhouse effect, *Nature*, **244**, 324–327.
- Wikle, C.K., and N. Cressie, 1996: A spatially descriptive, temporally dynamic statistical model with applications to atmospheric processes, in PhD, Dissertation, Iowa State University, Ames IA.
- Xu, J.S., 1993: The joint modes of the coupled atmosphere-ocean system observed from 1967-1986. *J. Clim.*, **6**, 816–838.
- Yang, J. and J.D. Neelin, 1993: Sea-ice interaction with the thermohaline circulation. *Geophys. Res. Lett.*, **20**, 217–220.
- Yang, J. and R.X. Huang, 1996: Decadal oscillations driven by the annual cycle in a zonally-averaged coupled ocean-ice model, **23**, 269–272.
- Yiou, P., Genthon, C., Jouzel, J., Ghil, M., Le Treut, H., Barnola, J.M., Lorius,

- C., Korotkevitch, Y.N., 1991: High-frequency paleovariability in climate and in CO₂ levels from Vostok ice-core records, *J. Geophys. Res.*, **96B**, 20365–20378.
- Yiou, P., Ghil, M., Jouzel, J., Paillard, D. and R. Vautard, 1994: Nonlinear variability of the climatic system, from singular and power spectra of Late Quaternary records, *Clim. Dyn.*, **9**, 371–389.
- Zhang, S., Lin, C.A., and R. Greatbatch, 1995: A decadal oscillation due to the coupling between an ocean circulation model and a thermodynamic sea-ice model., *J. Marine. Res.*, **53**, 79–106.